



NANOSTRUCTURED DIAMOND-LIKE CARBON BY DUAL PULSED LASER ABLATION-PULSED GAS FEEDING

PATRICK SIPHO SIBIYA

Thesis presented in fulfillment of the requirements for the degree of
Master of Sciences in the Department of Physics and Engineering at the
University of Zululand.

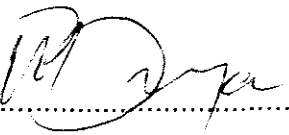
Supervisor: Dr. M. Maaza
Nano-science Laboratories, MRG, iThemba LABS

Co-supervisor: Prof. O.M. Ndwandwe
Dept. of Physics and Engineering, University of Zululand

December 2007

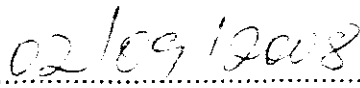
DECLARATION

I, the undersigned, hereby declare that the work contained in this thesis is my own original work and that I have not previously in its entirety or in part submitted it at any university for a degree.



.....

Signature



.....

Date

ACKNOWLEDGEMENTS

The author would firstly express many thanks to the above might God for His presence in my life until I finish writing the thesis. I'm also humbling myself to express my gratitude to Dr M. Maaza for being supervising me and His excellent guidance and constant without any compromise throughout the process of the work.

I also want to send warm thanks to my co-supervisor Prof O.M. Ndwandwe for giving me an opportunity to further my studies towards Masters. I would like to thank U. Buttner at University of Stellenbosch in engineering department for His assistance in the technical part of PLD technique during the process of deposition.

My warm thanks also go to Miranda at University of Cape Town for her assistance in SEM and Also T. Kerdja at Centre de Dev. des Techniques Avancees, Algeria contributed.

Furthermore, I would like to mention that Mathew Moodley at CSIR deserve more rewards for His contribution in organizing the analytical techniques such as XPS, Zygo, and FTIR. Also thank Tshepiso Baisitse for helping me on Zygo and FTIR. I thank Dr Marthin van Staden at the department of National Metrology Laboratory (NML) for assisting

with XPS, Dr Eino Vuorinen for contribution with FTIR. Without them I will not be in this platform. I also send lot of credit to Phillip Sechogela for assisting me with RBS and ERDA and with the simulation the experimental data. My thanks also cascades to Dr S. Halindintwali at the UWC for his enduring in assisting with UV-VIS spectrometer and STYLUS Profiler. I would like to send my big thanks the staff of iThemba LABS (MRG) for treating me as their brother throughout the process of the research. Many thanks also go to the middle man Dr Chris Theron for organizing return bus tickets for me throughout the year.

In my finally acknowledgement I would like to sincere my warmest thanks to the family as large for their constant encouragements and motivations towards my success. I would like to sincerely my warmest thanks to my mom and the late dad, Christina Mangwane and Joseph Sibiya with their value to my life.

I acknowledge the support I got from National research Foundation (NRF) jointly with iThemba LABS for sponsoring me throughout the research period of the work.

Summary

Diamond-like carbon films is a metastable form of carbon containing mixture of sp^3 and sp^2 hybridization. In the previous decades Diamond-like carbon has been studying widely due to its unique properties resembling those of diamond. These properties exhibit the high hardness, high wear resistance, low friction coefficient, chemical inertness, high electrical resistance, and optical transparency in the IR region. These properties make DLC films a good candidate in various applications such as the mechanical, optical, coating magnetic hard disks, and biocompatibility in the replacement of hip joints, heart valves, stents, as well as zinc sulphide for IR windows. In the present work nano-structure diamond-like carbon was deposited at room temperature by Pulsed Laser Ablation in a methane atmosphere on corning glass and silicon substrate. The structures of Diamond-like carbon film such the surface morphology and the composition has been studied by the scanning electron microscopy (SEM) and X-ray photoelectron spectroscopy (XPS). The structural properties of DLC films have been studying by were investigated by Raman spectroscopy. The vibrational mode of C-H molecules and the composition of carbon, oxygen and hydrogen have been investigated

by Fourier transformations Infrared Absorption, Rutherford backscattering, Elastic Recoil Detector. The optical and the surface topography of the films have been studied by Ultraviolet Visible spectrophotometer, Zygo interferometer, and Stylus Profiler. SEM shows that DLC films deposited in a high vacuum peel out of the silicon substrate whereas the films deposited on glass shows the dark yellow color depending on the thickness of the films. Raman results indicate the depended of DLC films on deposition time, the sp^3 fraction increase from 21% to 97.1% and the peak position changes with respect to time. XPS result shows excellent films produced by pulsed laser ablation with C1s in the range 81.5%-88.8 % with the surface roughness less 30nm. These smooth film shows promise applications on hard and medical biocompatibility. DLC films deposited on have refractive (n) in range of 1.7 to 2.2 suitable for optical applications.

Keywords: *Pulsed laser ablation; Diamond-like carbon (DLC) films; Raman spectroscopy; XPS; UV-VIS.*

Nomenclature

μ	Coefficient of friction
C	Carbon
a-C	amorphous carbon
a-C:H	amorphous hydrogenated carbon
DLC	Diamond-Like Carbon
ta-C	tetrahedral amorphous carbon
PECVD	plasma enhanced chemical vapor deposition
PIII-D	plasma immersion ion implantation deposition
CVD	chemical vapour deposition
PLD	pulsed laser deposition
IBD	Ion Beam Deposition
SEM	Scanning Electron Microscopy
FT-IR	Fourier transforms Infrared Absorption
UV-VIS	Ultraviolet and Visible Spectroscopy
sp^3	Orbital hybridization characteristic for diamond-like carbon
sp^2	Orbital hybridization characteristic for graphite-like carbon
ERDA	elastic recoil detection analysis
RBS	Rutherford backscattering spectrometry
XRD	X-ray Diffraction

XeBr	Xenon bromide
XeCl	Xenon chloride
XeF	Xenon fluoride
XPS	X-ray Photoelectron Spectroscopy
ECR-CVD	Electron cyclotron resonance chemical vapor deposition

TABLE OF CONTENTS

TABLE OF CONTENTS.....	ix
CHAPTER 1	1
1. Introduction.....	1
2. Dissertation’s overview and objectives	12
CHAPTER 2	13
2. Literature review.....	13
2.1. Diamond-Like Carbon family.....	13
2.1.1. Growth mechanism of diamond like carbon	21
2.1.2. Properties of DLC.....	24
2.1.3. Surface properties	25
2.1.4. Mechanical properties.....	26
2.1.5. Optical properties	30
CHAPTER 3	31
3. Diamond-Like Carbon by non radiative deposition techniques	31
3.1. Ion Beam Deposition.....	31
3.2. Plasma Enhanced Chemical Vapor Deposition	33
3.3. Sputtering Deposition	34
3.4. Diamond-Like Carbon by Pulsed Laser Deposition	35
CHAPTER 4	51

4.	USED CHARACTERISATION TECHNIQUES	51
4.1.	SURFACE MORPHOLOGY	51
4.1.1.	Scanning Electron Microscopy	51
4.1.2.	Surface Zygo interferometry	54
4.1.3.	Surface Mechanical Profilometry	56
4.2.	Chemical analysis	58
4.2.1.	Rutherford backscattering Spectrometry	58
4.2.2.	Elastic Recoil Detection Analysis	61
4.2.3.	X-ray Photoelectron Spectroscopy	61
4.3.	VIBRATIONAL & OPTICAL PROPERTIES.....	64
4.3.1.	Raman Spectroscopy.....	64
4.3.2.	Infrared spectroscopy.....	67
4.3.3.	UV-VIS-NIR optical Spectroscopy.....	74
CHAPTER 5	76
5.1.	EXPERIMENTS & DISCUSSIONS	76
5.1.1.	Synthesis by double pulsed gas-feeding/pulsed laser deposition.....	76
5.1.2.	Characterization techniques and characterization conditions	83
5.1.3.	Surface morphology properties.....	86
5.1.4.	Elemental analysis and hydrogen-Carbon content.....	97
5.2.	Vibrational and electronic properties.....	107
5.2.1.	Raman spectroscopy investigations.....	107
5.2.2.	Infrared spectroscopy investigations	114

5.2.3. X-rays photo-emission electron spectroscopy investigations	118
5.2.4. Optical properties.....	128
CHAPTER 6	132
Conclusion and PERSPECTIVES	132
Bibliography	136

LIST OF FIGURES

Figure 1:	Major crystalline polymorph forms of carbon	3
Figure 2:	Schematic representation of sp^1 , sp^2 , and sp^3 hybridization of carbon	4
Figure 3:	Schematic diagram of hexagonal structure of graphite (ABAB)	8
Figure 4:	Ternary phase diagram for the classification of DLC coatings	14
Figure 5:	(a) schematic representation of the variation of the sp^2 bonds along the 3 amorphization stages. (b) Schematic comparison of the evolution of sp^2 cluster size « L_a » and sp^3 content	19
Figure 6:	(a) Density versus sp^3 fraction for different DLC coatings. (b) Density versus Young's modulus for ta-C DLC films	20
Figure 7:	Schematic component processes during the growth phase of an amorphous.	23
Figure 8:	High pressure-high temperature phase diagram of carbon....	37
Figure 9:	Schematic illustration of the time scale key phases of the PLD... ..	40
Figure 10:	Schematic diagram of a standard apparatus of PLD.	46
Figure 11:	Three basic mechanisms of PLD film growth	48
Figure 12:	Influence of impact energy on type of carbon based film produced	50
Figure 13:	Schematic illustration of SEM and its collection/detection of secondary electrons emitted from the sample surface.....	53
Figure 14:	Schematic illustration of Zygo interferometer.	55
Figure 15:	Schematic illustration of surface roughness and surface waviness which is accessible by mechanical dektak profilometry.....	57
Figure 16:	Schematic illustration of He+ backscattering in an RBS geometry	60

Figure 17: Schematic illustration of (a) core electronic configuration and XPS phenomena at the (b) excitation and (c) after relaxation.....	63
Figure 18: Schematic illustration of Raman scattering.....	68
Figure 19: The construction of envelopes in the transmission spectrum...75	
Figure 20: Determination of the refractive index from the transmission spectrum maxima and minima.....	75
Figure 21: Schematic diagram of Pulsed laser deposition.....	78
Figure 22: Photograph of the dual beam pulsed gas feeding/pulsed laser deposition setup	79
Figure 23: Typical DLC films synthesized by (a) standard PLD and (b) dual pulsed gas flow beam-pulsed laser beam.	82
Figure 24: Evolution of the average surface roughness versus the DLC films' thickness and illustration of the coalescence phenomena of the C, C-H clusters onto the substrate's surface	88
Figure 25: Typical interferogram obtained by Zygo interferometry (a) and in false color (b) as well as the deduced surface roughness profile (c).....	91
Figure 26: Evolution of the peak to valley roughness versus the DLC films' thickness and illustration of the surface smoothing on large scale.	92
Figure 27: Scanning electron microscopy of DLC films deposited at (a) unheated [sample E3] and (b) heated 500°C [sample H] glass substrates.....	94
Figure 28: Typical DLC films deposited onto unheated glass substrates with thicknesses of (a) 420 nm [sample C4] and (b) 740 nm [sample C6].	96
Figure 29: Rutherford Backscattering profiles of DLC films deposited onto Si(100) at different times during a fixed deposition pressure of $1 \cdot 10^{-2}$ mbars (Table 1).....	100

Figure 30: Rutherford Backscattering profiles of DLC films deposited onto Si(100) at different times during a fixed deposition pressure of $1 \cdot 10^{-2}$ mbars (Table 1).....	101
Figure 31: Typical ERDA profile of DLC/Si(100) with its simulation by RUMP program (Table 1).....	102
Figure 32: ERDA profiles of DLC films deposited onto Si(100) at different pressures during a fixed time of 25min (Table 1).....	103
Figure 33: Comparison of typical Raman spectra of carbons	106
Figure 34: Room temperature Raman spectra of samples E1, E4 and E5 (Table 7).....	110
Figure 35: Schematic illustration of the factors affecting the positions and heights of the Raman G and D peaks of non-crystalline carbons.	113
Figure 36: Room temperature Infrared spectroscopy spectra of samples E1, E2, E3 and E4 (7).....	116
Figure 37: Typical core level XPS spectra of a DLC film: carbon (C) 1s, oxygen (O) 1s, and silicon (Si) 2p.	120
Figure 38: Typical core level XPS spectra of a DLC film at the Cs1 edge for samples of series E.	122
Figure 39: Thickness evolution of sp^2 and sp^3 populations for samples of series E.	126
Figure 40: Experimental optical transmittance spectra of DLC films deposited at different voltages: D3 (O O O O), D4 () and D6 (●●●●).	130
Figure 41: Dispersion relation of DLC films deposited onto glass substrates.....	131

LIST OF TABLES

Table 1:	Properties of Diamond material; (a) is the typical values, 1050 and 1054, (b) typical value, 0.2, (c) typical value, 1.5 to 4.8 at 127 to 927°C, I is lattice impurity type (I), and II is lattice impurity type (II).....	6
Table 2:	Properties of graphite material ; (a) is the typical values, 1050 and 1054, (b) typical value, 0.2, (c) typical value, 1.5 to 4.8 at 127 to 927°C.....	7
Table 3:	Summary of the properties and applications of Diamond-like carbon films.	17
Table 4:	Properties of the various forms of carbon. The data is taken from H. Ronkainen	18
Table 5:	IR absorptions of C-H bond	72
Table 6:	Variation of IR vibrational frequencies in hydrogenated amorphous carbon (a-C:H).....	73
Table 7:	The deposition parameters of the deposited DLC films at different conditions.	84
Table 8:	Used morphological, elemental-chemical and optical characterization techniques.	86
Table 9:	The average surface roughness versus the DLC film's thickness determined by mechanical surface profiling	87
Table 10:	Summary of the study of H concentration in carbon and DLC films obtained from different methods	104
Table 11:	Raman results of the G and D peaks of samples E1, E4 and E5 (Table 7).....	109
Table 12:	IR vibrational frequencies in hydrogenated amorphous carbon (a-C:H).....	115
Table 13:	IR vibrational mode assignments in the C-H stretch region for the DLC films with different thicknesses deposited onto Si(100).....	117

Table 14:	Summary of the study of C1s and sp^3 content (%) of DLC films prepared by different methods in previous work.....	119
Table 15:	Summary of the XPS studies on samples of series E and D and their corresponding simulation parameters.....	123
Table 16:	Thickness evolution of sp^2 and sp^3 populations for samples of series E.....	127
Table 17:	Summary of the optical properties of DLC films produced by PLD in an atmosphere of CH_4	129

CHAPTER 1

1. Introduction

Carbon is among the primary element in nature. It is the element found in the sixth place of the list of abundance and is found in the state of containing two isotopic forms such as C_{12} and C_{13} in nature. The C_{12} consists of 6 protons and 6 neutrons. Natural carbon is a tetravalent as the result of the 6 electrons and 4 other revolving the outer orbital ($2sp^2$) [Gop-2002]. Carbon is well established element via its natural and synthetic as well as numerous polymorph forms such as diamond, graphite, fullerene, carbon nanotubes and amorphous carbon in addition to additional families such carbon black, carbon fibers, porous carbon, glassy carbon, diamond-like carbon (DLC), and the new recently discovered carbon forms: fullerenes and carbon nanotubes [Gop-2002,Sum-2004]. From bonding viewpoint, and as indicated in Figure 1, the hybridization of carbon sp^1 «linear coordination», sp^2 «trigonal», and sp^3 «tetrahedral» [Gop-2002] due to its crystalline and disordered structures [Rob-2002], gives clarity about how carbon molecules in each everyone of the 3 chemical structures atomically structures itself [Gop-2002, Hid-1999]. This family of bonding give rise to the key forms of carbon which are naturally the most investigated and

applied materials. These forms are (i) natural carbon diamond, (ii) graphite carbon, (iii) carbon nano-tubes «CNTs» and, the famous diamond like-carbon known generally via their abbreviation as DLC.

Diamond is known as archetypal material, inhomogeneous with some defects which make the material in fact not suitable for certain applications [Mor-1999]. The name of diamond was derived from the Latin word *adamas* which mean untamable or unconquerable defining hardness [Gop-200].

Diamond has exceptional optical and electrical properties. Its optical transparency is significant in a very large optical spectral range extending from the UV to far infrared [Ued-1999] associated to its large band gap of about diamond of $E_g=5.5$ eV [Web-1998, Gop-2002]. The specific sp^3 hybridization of carbon in the diamond form is that each carbon atom is bonded tetrahedrally to neighboring carbon atoms at an angle of 109.5° as a result of σ bonds originating from the sp^3 hybridization.

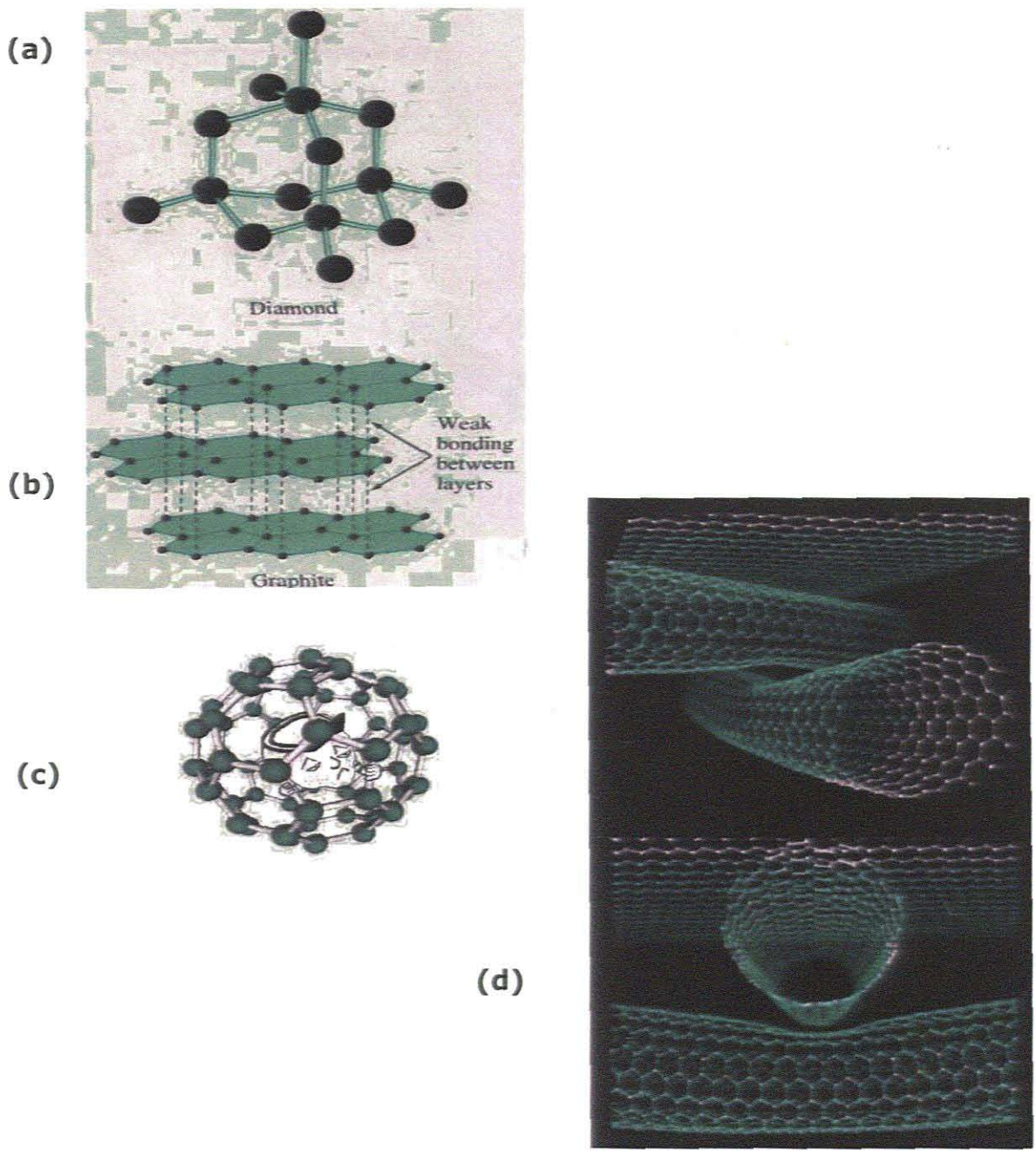


Figure 1: Major crystalline polymorph forms of carbon [Gop-2002, Hid-1999].

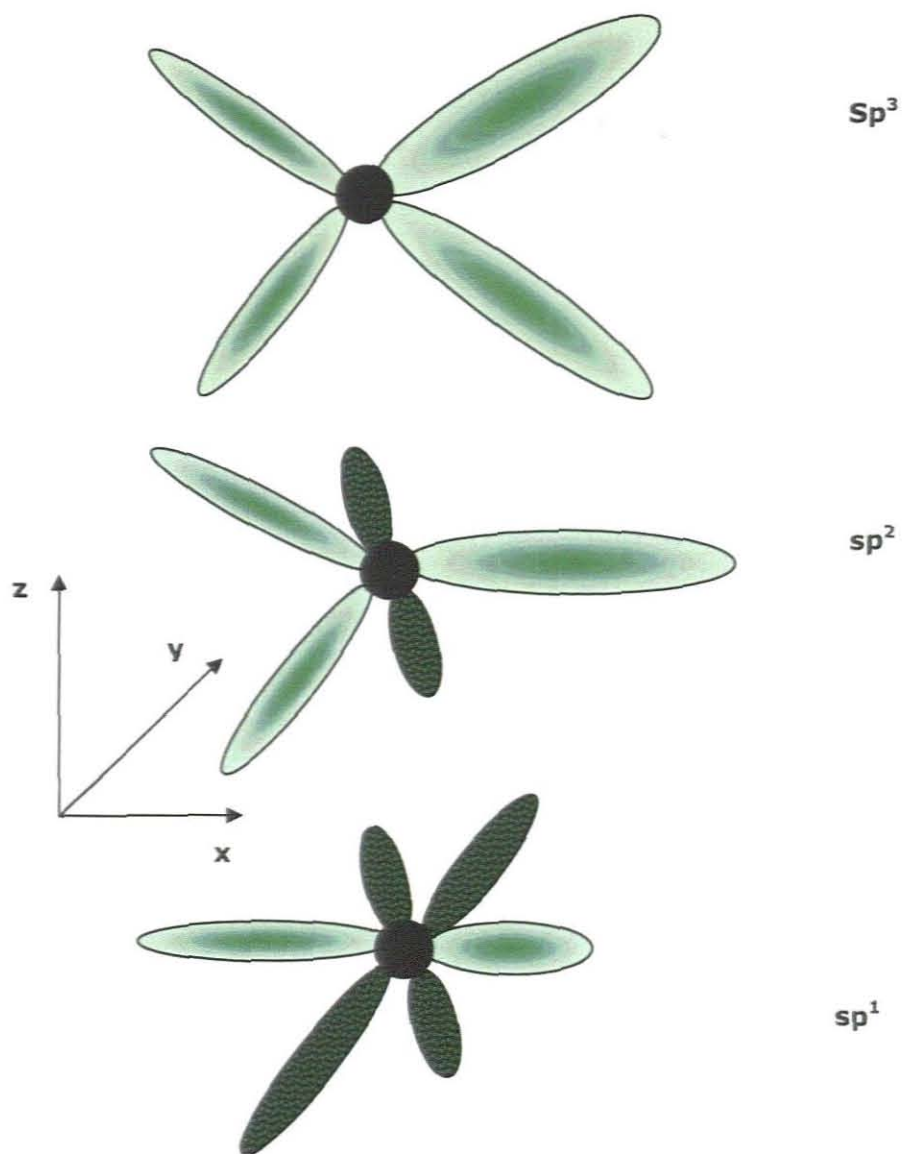


Figure 2: Schematic representation of sp^1 , sp^2 , and sp^3 hybridization of carbon [Gop-2002, Hid-1999].

The corresponding short covalent bond length is «C-C \approx 0.14 nm». In addition, the high density «3.5g/cm³» of diamond makes it the highly dense form of carbon at room temperature-atmospheric pressure. Due to the covalent C-C bonds, the diamond is quite chemically inert; it is resistant to chemicals and there are no reactions between it with concentrated acids or any strong oxidizing agents [Sea-2003]. Nano-structured diamond or thin films of diamond can be produced at relatively high temperature «800°C» and high pressure using microwave chemical vapor deposition process «MPCVD» [Mor-1999, Lin-2002].

The cubic crystallographic structure found in diamond consists of sp³ carbon-carbon bonds. These nano-structured diamond form exhibits a significant mechanical hardness «*Knoop hardness of \approx 7000 kgmm⁻²*» and a large thermal conductivity «*1000 Wm⁻¹ at 273 K*». The cubic structure of diamond can be seen with packing of infinite layers of {111} planes and the pile up along the planes {111} has ABCDC structure as illustrated in figure 1.a. The properties of diamond are summarized in table1 [Kaz-1998].

Form	Diamond
Density, g/cm ³	3.52
Young's modulus, GPa	^a 910-250
Poisson's ratio	^b 0.1-0.29
Compression strength, GPa	8.68-6.53
Vickers hardness, GPa	60-100
Thermal conductivity at 25°C, W/m-°C	600-1000 (type Ia) 2000-2100 (type II)
Coefficient of thermal expansion at 25 to 200°C, 10 ⁻⁶ /deg C	^c 0.8-4.8
Specific heat at 25°C, kJ/kg-K	0.502-0.519

Table 1: Properties of Diamond material; (a) is the typical values, 1050 and 1054, (b) typical value, 0.2, (c) typical value, 1.5 to 4.8 at 127 to 927°C, I is lattice impurity type (I), and II is lattice impurity type (II).

The second well known form is the graphitic form so called graphite. The name of graphite derives from the Greek verb «graphain» means writing. It has been used as a writing material from the beginning of mid 15th century and was called black lead. It is used in pencil and called pencil lead because there were feeling graphite contains lead. The sp² configuration is found in graphite, each atom is bonded trigonal to each other and also forms σ bonds but the remaining electron is found in the p π orbital. The angle between the atoms is 120°. The graphite is highly anisotropic solid [Gop-2002] with a crystal lattice parameters a₀=0.246 nm and c₀=0.6708 nm relatively to the position of atoms [Kaz-1998].

The physical property of graphite shows that the material is stiff and quit large along the plane due to the σ bonds. Along perpendicular direction graphite is weak as the results van der Waal's force [Web-1998, Rob-2002]. The atomic packing of graphite crystal is hexagonal «Alpha» with the arrangement of- ABABAB- stacking order as shown by Figure 3. The summary of the major properties of graphite are shown in Table 2 as follows [Kaz-1998].

Property	Graphite
Density, g/cm ³	2.26
Young's modulus, GPa	Single crystal: 1060 (a direction) 36.5 (c direction), Pyrolytic graphite, 28-31, Molded graphite, 5-10
Compression strength, GPa	0.065-0.089
Vickers hardness, GPa	Pyrolytic graphite, 2.4-3.6 Molded graphite, 3.9-9.8
Thermal conductivity at 25°C, W/m-°C	Pyrolytic graphite: a and b directions, 190-390 c direction, 1-3, Molded graphite, 31-159
Coefficient of thermal expansion at 25 to 200°C, 10 ⁻⁶ /deg C	Pyrolytic graphite: a and b directions, -1 to 1 c direction, 15-25, Molded graphite, 3.2-5.7
Specific heat at 25°C, kJ/kg-K	0.690-0.719

Table 2: Properties of graphite material; ; (a) is the typical values, 1050 and 1054, (b) typical value, 0.2, (c) typical value, 1.5 to 4.8 at 127 to 927°C

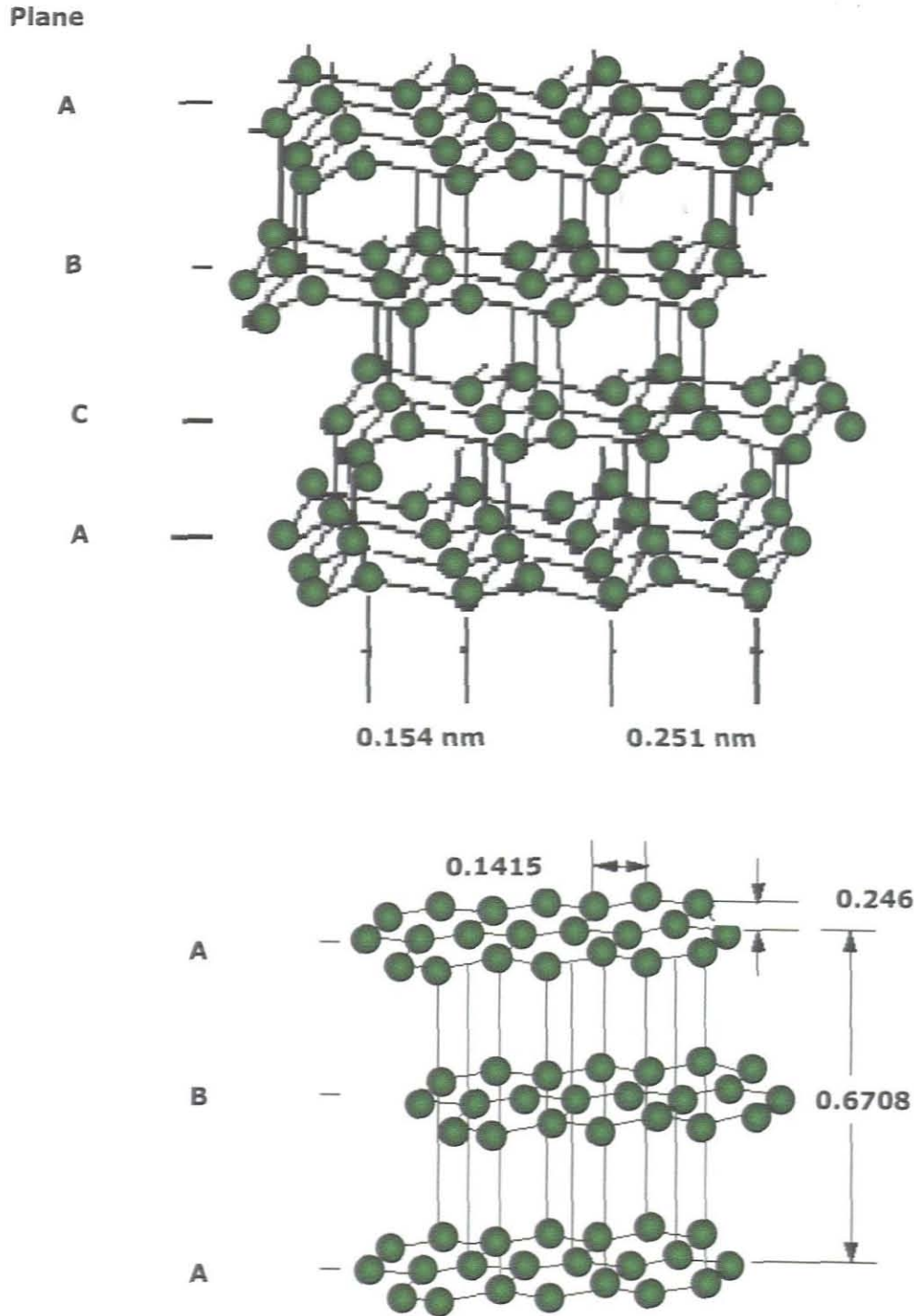


Figure 3: Schematic diagram of hexagonal structure of graphite (ABAB).

The third major forms of carbon are fullerenes and carbon nanotubes. These later tubular nano-structures were recently discovered with fullerenes. The synthesis of carbon nanotubes was pioneered in 1991 by Iijima of NEC in Japan. Carbon nanotubes were first produced by arc discharge between graphite electrodes, the collected particles were fine tube-like structures. The name carbon nanotubes were coined after some analysis. Carbon nanotubes are divided into two main types: single-walled nanotubes «SWNTs» and multi-walled nanotubes «MWNTs». SWNTs are long tubular 1 sheet of carbon. These tubes can be open at their ends or either limited at one ends with half spheroidal fullerene via an acidic reaction as the fullerene end consists of combined sp^2 and sp^3 bonds. In addition to their multi-functional transport properties «they can be either insulators, semiconductors or metallic», their mechanical strengths of carbon nanotubes is about 6000 times stronger compared to steel and it can be used in electro mechanical systems (MEMS) and in aerospace [Gop-2002]. The structure of CNTs is shown by Figure 1d. The electronic properties of carbon nanotubes are easy to be characterized as the results of small in dimensions. CNTs can also be produced by PLD using C_{NiCo} target or graphite [Noo-2005].

The fourth family of carbon which is the main concern family within this research work is an artificial diamond so called Diamond-Like Carbon and abbreviated as «DLC». Diamond-like carbon is described as an amorphous carbon containing relatively high degree of sp^3 bonding [Hid-1999, Hel-2001, Sam-1999, Rob-2002, Xia-2002, Sea-2003, Joh-2006] and is one amongst the synthetic form of carbon which has both sp^3 and sp^2 coordinations.

The term DLC includes all the materials with properties similar to graphite and those of natural diamond [Gop-2002, Fil-2003]. Their unique physic-chemical properties [Sun-2004] include high hardness, high wear resistance, low friction coefficient, chemical inertness, high electrical resistance, and optical transparency in the visible as well as in the infrared regions depending on the deposition conditions. Ahalapitiya et al report that the physical properties of DLC depend upon the sp^3/sp^2 ratio [Aha-1999]. The sp^2 and sp^3 atomic coordinations network is randomly distributed [Mul-1999]. Diamond-like carbon is divided into three main families [Jac-2005]:

- ***Amorphous carbon «a-C»***,
- ***Tetrahedral amorphous carbon «ta-C» and***,
- ***Hydrogenated amorphous carbon «a-C:H»***.

In this later component, it was demonstrated that the hydrogen atoms at the surface of the carbon films enhances the sp^3/sp^2 ratio [Gop-2002, Hid-1999], stabilize the sp^3 bond «diamond» and increase the optical gap as well as the electrical resistivity [Sta-1998]. Due to its enhanced mechanical and infrared optical characteristics, it is a material of choice in the mining sector «machining drills» and micro-electronic industry such as a protection of computer hard drive magnetic discs. In addition its bio-compatibility makes it useful bio-coating in a replacement of hip joints, heart valves, and stents [Sea-2003, Heo-2004, Bon-2005, Heo-2006]. DLC can be doped with other elements without changing some of the properties like hardness and low friction coefficient [Vas-2004] opening opportunities in electronics in both its p - and n -type forms as in the case of standard semiconductors doped with Boron and phosphorus respectively [Sea-2003].

Among others, Sunil et al [Sun-2004] have confirmed the DLC doping with additional periodic elements such as Si, N and numerous metal atoms, as well as F to improve its properties. In the previous studies the doping of DLC with materials such as Ni, W, and Ti reduces the wear resistance films. Indeed, DLC usually is affected by internal stresses which make the film poor in some of the applications. Its nitrogen doping reduces the internal compressive stress without influencing its mechanical hardness [Heo-2004, Vas-2004]. In addition, it was confirmed in a reproducible way that the doping of the a-C:H films with Si modifies the structure and improves the adhesion, thermal stability as well as the tribological properties under humid condition [Chu-2002].

2. Dissertation's overview and objectives

In this research work, while this chapter is intending to give a general overview about carbon nanostructures with a focus on DLC nanostructures, chapter two gives a survey literature review about DLC in general. Chapter three described the different types of deposition techniques used to synthesize and engineer DLC nanostructures. Chapter four describes the pulsed laser deposition, a technique of choice used in this research work. Chapter five covers the experimental part related to chapter 4. Chapter six contains the conclusions and future outlook of this work.

The present work reports on the synthesis of nanostructured diamond-like carbon coatings by a novel dual pulsed laser deposition/gas feeding joint technique and their properties. Therefore the main objectives of this research are:

- (i) The demonstration of the feasibility double pulsed gas feeding/pulsed laser ablation for room temperature synthesis of diamond-like carbon.***

- (ii) The optimization of the deposition's conditions to ensure a reproducibility of synthesis based on various characterization techniques.***

CHAPTER 2

2. Literature review

2.1. Diamond-Like Carbon family

Among the natural and synthesis of carbon forms including diamond, graphite, fullerene, carbon nanotubes, the amorphous carbon «a-C» or diamond-like carbon is the major focus within this research work [Gop-2002, Yib-2003, Sun-2004]. DLC is described as metastable form of carbon, containing mixture of sp^3 and sp^2 hybridization. These two hybridizations are found in diamond and graphitic carbon. Hence, the properties of the DLC films depend strongly on the ratio of the hybridization ratio of sp^3 and sp^2 coordinations. The amorphous carbon films rich in sp^3 content described as tetrahedral amorphous carbon, at some other stage ta-C films are highly stress and are easily flaked off from the substrate. Amorphous carbon «a-C:H» is known by its specific physical state such as its softness combined with its higher degree of optical transparency than the other hydrogen free forms [Hid-1999, Sam-1999, Hel-2001, Rob-2002, Yib-2003, Joh-2006]. As one could expect, the sp^2/sp^3 ratio of this type of carbon films depend on the deposition conditions, although the sp^3 content can be maximized if the substrate temperature is maintained at room temperature as the heat influences the graphitization [Jac-2005]. Diamond-like carbon is one of the synthetic form of carbon having the tendency to contain both sp^3 and sp^2 coordination, with superior properties similar to those of diamond because of the availability of sp^3 bonds [Sun-2002]. Those superior properties can be distinguished via the high hardness, high wear resistance, low

friction coefficient, chemical inertness, elastic moduli, high electrical resistance, and optical transparency in the visible and infrared. Naturally, these characteristics are strongly dependent on the deposition conditions of the DLC hydrogenated films in particular, vis-a vis of the bombarding particles' energy at the surface of the and the hydrogen atmosphere as per sustained by the phase diagram of figure 4.

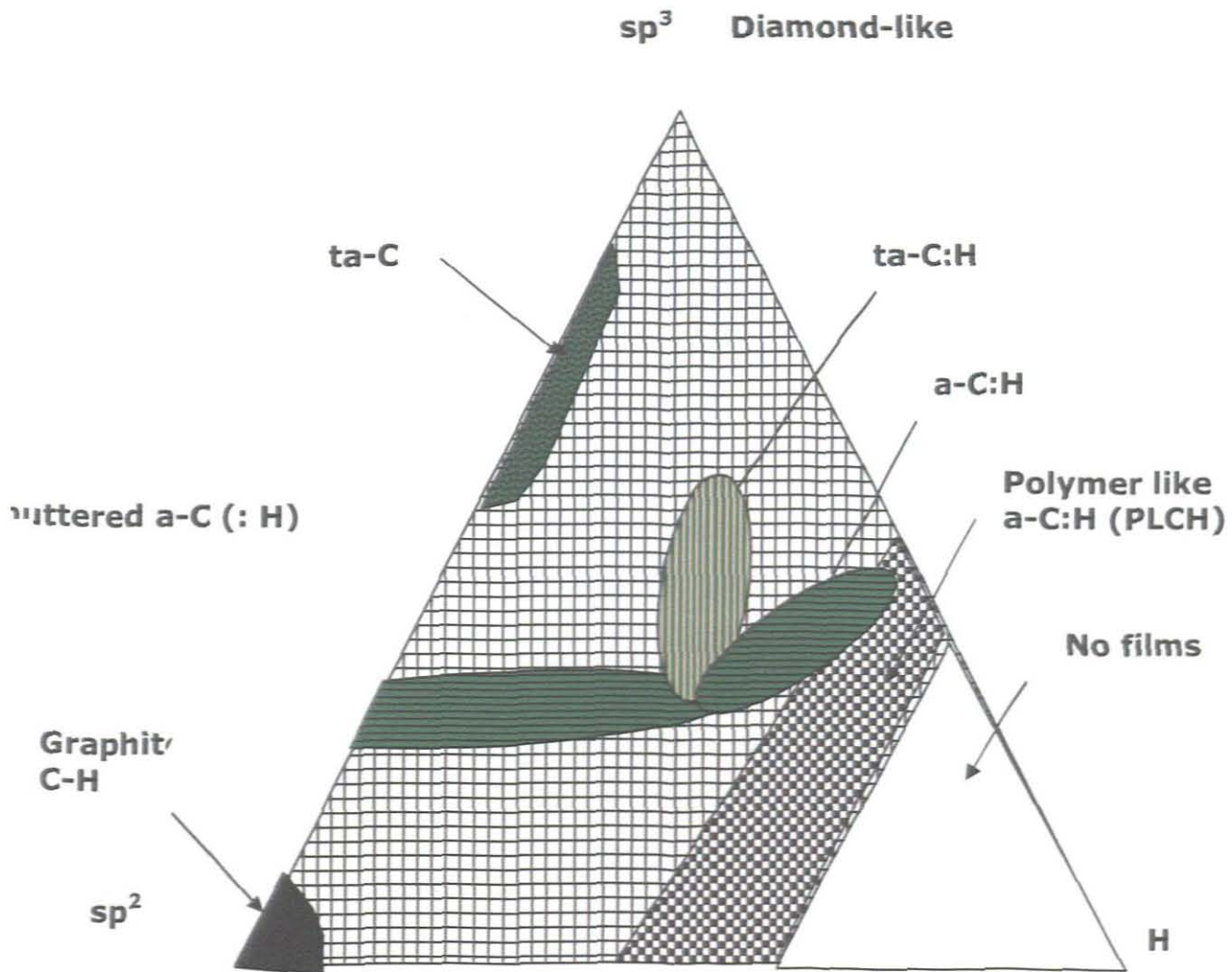


Figure 4: Ternary phase diagram for the classification of DLC coatings [Rob-2002].

As mentioned previously and illustrated within figure 4, this DLC family is divided into 3 main types, namely amorphous DLC «a-C», hydrogenated tetrahedral amorphous carbon «ta-C:H», and hydrogenated DLC «a-C: H» and. The first type of DLC contains relatively high degree of sp^3 bonding. The second type of DLC contains relatively high degree of sp^3 bonding with hydrogen content as indicated in table3-4 [Rob-2002, Sea-2003]. The third type contains low sp^3 bonding. The amount of hydrogen on the films has been confirmed to increase the sp^3/sp^2 ratio as much as it is located in a certain concentration range [Hid-1999, Sun-2002]. In all three cases, the sp^3/sp^2 ratio is considered as a signature of diamond/graphite nature [Web-1998].

As one moves from ordered graphite to nano-crystalline graphite «nc-G» to amorphous carbon «a-C» and at the end to sp^3 bonded ta-C, the sp^2 groups become first smaller, and then disordered, and finally change from ring structure to chain configurations. The evolution of the sp^2 phase clustering can be represented by the so called amorphization trajectory as indicated in Figure 5. This amorphization trajectory consists of 3 stages from graphite to ta-C. These are: (i) graphite to nc-G, (ii) nc-G to sp^2 a-C and at finally (iii) a-C to ta-C. The sp^2 clustering evolution and the sp^3 content evolution follow different paths as indicated in Figure 5. The general classification of the DLC structure accepted within the scientific community is as follows (Figure 4):

- a. a-C:H films with the highest hydrogen content of about «40-60%». These films can have up to 70% of sp^3 bond population where most of it is H-terminated and so the material is soft with a low density. These DLC films are called polymer-like a-C:H «PLCH».

- b. The band gap of this family usually deposited by plasma enhanced chemical vapour deposition at low bias voltage, is found to within the range of 1-4 eV.
- c. a-C:H films with an intermediate H content of about 20-40%. Yet these second class of DLC films have lower sp³ content, they have more C-C sp³ bonds than the polymer like a-C:H. Hence, they exhibit better mechanical properties with an optical gap ranging from 1 to 2 eV. These films are called diamond-like a-C:H «DLCH» They are usually deposited by plasma enhanced chemical vapour deposition, electron cyclotron resonance or reactive sputtering at moderate bias voltage.
- d. Hydrogenated tetrahedral amorphous carbon films «ta-C:H» are a class of the DLCH in which the C-C sp³ content can be increased while keeping a fixed H content. Because of the higher sp³ content which is about 70% and 25-30% H «atomic %», the ta-C:H films are indeed a different category with a net different Raman signature, higher density of the order of 2.4g/cm³ associated to a Young modulus which can reach 300GPa. The optical band gap of this DLC films which are deposited generally by plasma enhanced chemical vapour deposition at high bias of magnetron sputtering, can be as high as 2.4 eV.
- e. a-C:H with low H content , less than 20 at.%. These coatings have a large sp² content and sp² clustering. Their gap is low of about 1 eV. This family is called graphite-like a-C:H. As in the case of the ta-C:H films, they are deposited generally by plasma enhanced chemical vapour deposition at high bias of magnetron sputtering.

Property	Type of use	Application
Transparency in visible and IR; optical band =1.0-4.0eV	Optical Coatings	Antireflective coatings and wear resistant coatings for IR
Chemical inertness to acids, alkalis and organic solvents	Chemically passivating coatings	Corrosion protection of magnetic media, biomedical
Nan-smooth	Very thin coatings <5nm	Magnetic media
Wide range of electrical resistivities= $10^2-10^{16}\Omega/cm$	Insulating coatings	Insulating films
Low dielectric constants <4	Low-k dielectrics Field emission	(interconnect dielectrics) (Field emission flat panel displays)
High hardness; H=5-80GPa; low friction coefficient. <0.01-0.7	Tribological, wear resistant coatings	Magnetic hard drives, magnetic tapes, razor blades (bearing, gears)

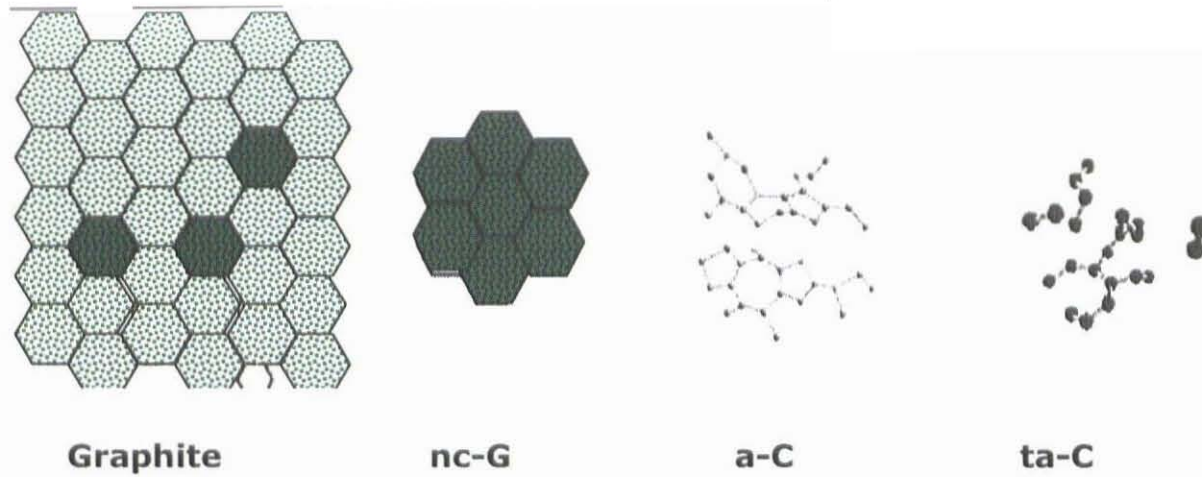
Table 3: Summary of the properties and applications of Diamond-like carbon films, data taken from Sunil Kumar Pal [Sun-2002]

The amount of hydrogen in deposited films increases the optical gap and electrical resistivity and stabilizes the diamond structure by maintaining the sp^3 hybridization configuration [Sta-1998]. From spectroscopy investigations, it was deduced that the other major role of hydrogen atoms on carbon network is to saturate the carbon dangling bonds and to soften them [Zha-1999]. Figure 6 shows clearly the paramount effect of hydrogen content upon the DLC films' density and therefore the whole of their physical properties and specifically their hardness characteristics [A.C. Ferrari et al, Phys. Rev.B.62, 11089, 2000].

Material	Density (g/cm³)	Hardness (GPa)	%sp³	At,%H	Band gap (eV)
Diamond	3.515	100	100		5.5
Graphite	2.267		0		-0.04
C₆₀			0	0	3
Glassy C	1.3-1.55	2-3	-0		0.01
a-C, eva.	1.9-2.0	2-5	1		0.4-0.7
a-C, sputt.	1.9-2.4	11-15	2-5		0.4-0.7
a-C, MSIB	3.0	30-130	90±5	<9	5.5-1.5
a-C:H, hard	1.6-2.2	10-25	30-60	10-40	0.8-1.7
a-C:H, soft	0.9-1.6	<5	50-80	40-65	1.6-4
Polyethylene	0.92	0.01	100	67	6
ta-C	3.0	55-65	Mainly	<1	
ta-C:H^b	2.4	50	70	30	2.0-2.5

Table 4: Properties of the various forms of carbon. The data is taken from H. Ronkainen [Hel-2001]. Data b is taken from J. Robertson [Rob-2002]

(a)



(b)

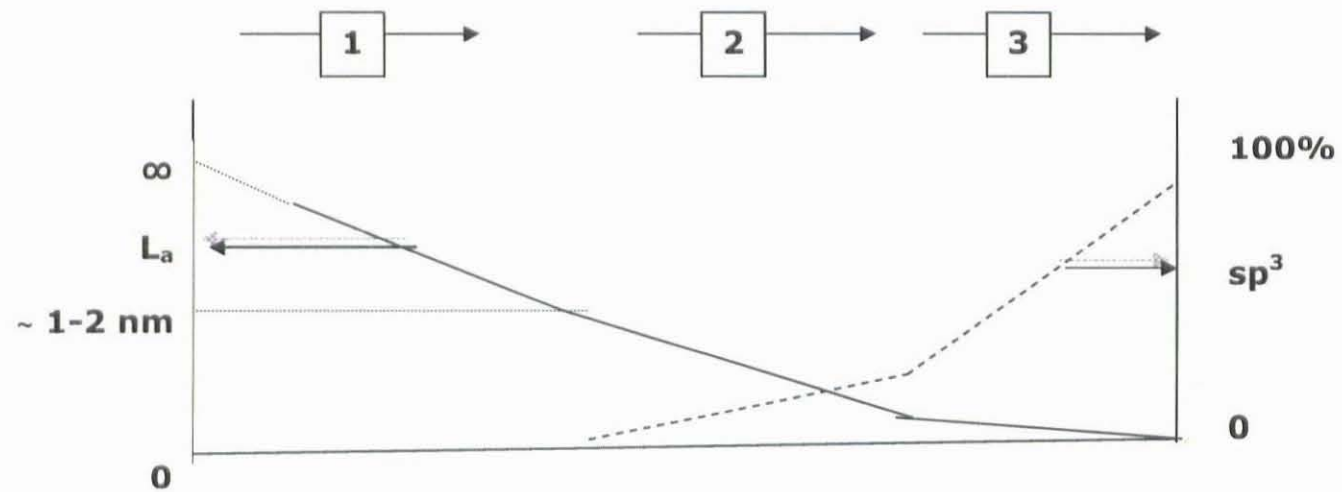


Figure 5: (a) Schematic representation of the variation of the sp² bonds along the 3 amorphization stages. (b) Schematic comparison of the evolution of sp² cluster size « L_a » and sp³ content [Ferari-2000].

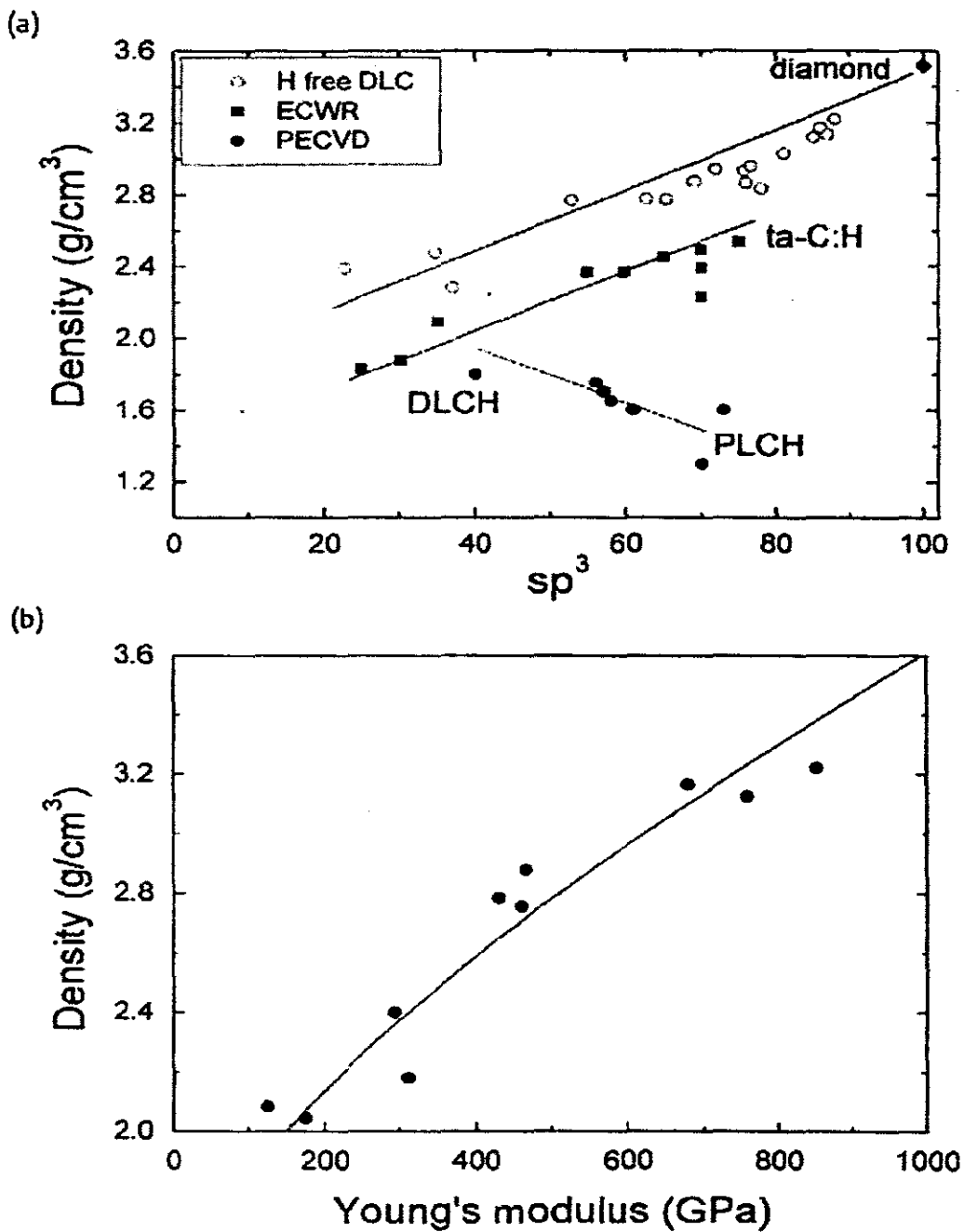


Figure 6: (a) Density versus sp^3 fraction for different DLC coatings. (b) Density versus Young's modulus for ta-C DLC films [Ferari-2000].

2.1.1. Growth mechanism of diamond like carbon

As mentioned previously, the crucial property of DLC is its sp^3 bonding. The deposition process which promotes this sp^3 bonding is a physical process: ion bombardment [J. Robertson: Diamond-like amorphous carbon, Materials Science and Engineering R37 (2002), 129-281]. Accordingly, the highest sp^3 fractions are formed by C^+ ions with energy of about 100 eV. The atomistic description of such sp^3 formation in presence of a hydrogen rich atmosphere can be easily understood in the case of a-C:H for example. The proposed model of sub-plantation by Robertson et al is the model which fits better with the experimental observations. Within this model illustrated by Figure 7, it is proposed that the sub-plantation phenomenon creates a metastable increase in density which induces a change in the local bonding to sp^3 . This change to sp^3 with this phenomenon of sub-plantation does not require any preferential displacement of favoured species' sputtering. Only sub-surface growth in a restricted volume is needed to obtain the sp^3 bonding [Rob-2002].

If one considers the system at the atomic scale in more detail in the energy range of interest i.e. 10-1000eV, the carbon ions have a penetration depth of few nanometer. They lose their kinetic energy largely by elastic collisions with the target atoms so called nuclear stopping. The cross-section of the collisions decreases as the energy is raised, as this is the repulsive part of the inter-atomic potential. Hence, an ion of zero energy impinging on a surface sees an impenetrable barrier of percolating spheres. At a higher ion energy, the atomic radii decrease, so the interstices look larger. At some energy, the ion can pass through an interstice and so penetrate the surface layer. This ion energy is called the

penetration threshold ζ_p . Another important ion energy is the displacement threshold ζ_d . This is the minimum energy value of an incident ion required to displace an atom from a bonded site and create a permanent vacancy interstitial pair. Hence, the surface region will act as an attractive potential barrier of height ζ_d , the surface binding energy. This raises the kinetic energy of an ion naturally by ζ_b when it enters the surface. Thus the net penetration threshold for free ions becomes $\zeta_p = \zeta_d - \zeta_b$. As the surface binding energy equals the cohesive energy, if this is about 7.4 eV for carbon with $\zeta_d = 25$ eV, then $\zeta_p \sim 32$ eV. If carbon ions are incident on an amorphous carbon target, there would be two cases.

A low energy carbon ion will not have enough energy to penetrate the amorphous carbon target, so it will stick on the surface and remains in its lowest energy state which is a sp^2 . If the incident carbon ion energy is higher than ζ_p , it has the probability to penetrate the surface and enter a sub-surface interstitial site. This will increase the local density. The local bonding environment will be affected accordingly to minimize its energy. In the highly energetic conditions of ion bombardment taking place during the growth process, atomic hybridizations will adjust so to changes in local density and become more sp^2 if the density is low and more sp^3 if the density is high. As the ion energy increases further, the ion range increases, and the ion penetrates deeper into the solid. A rather small fraction of this energy is consumed to penetrate the surface and 30% approximately is dissipated in atom displacements.

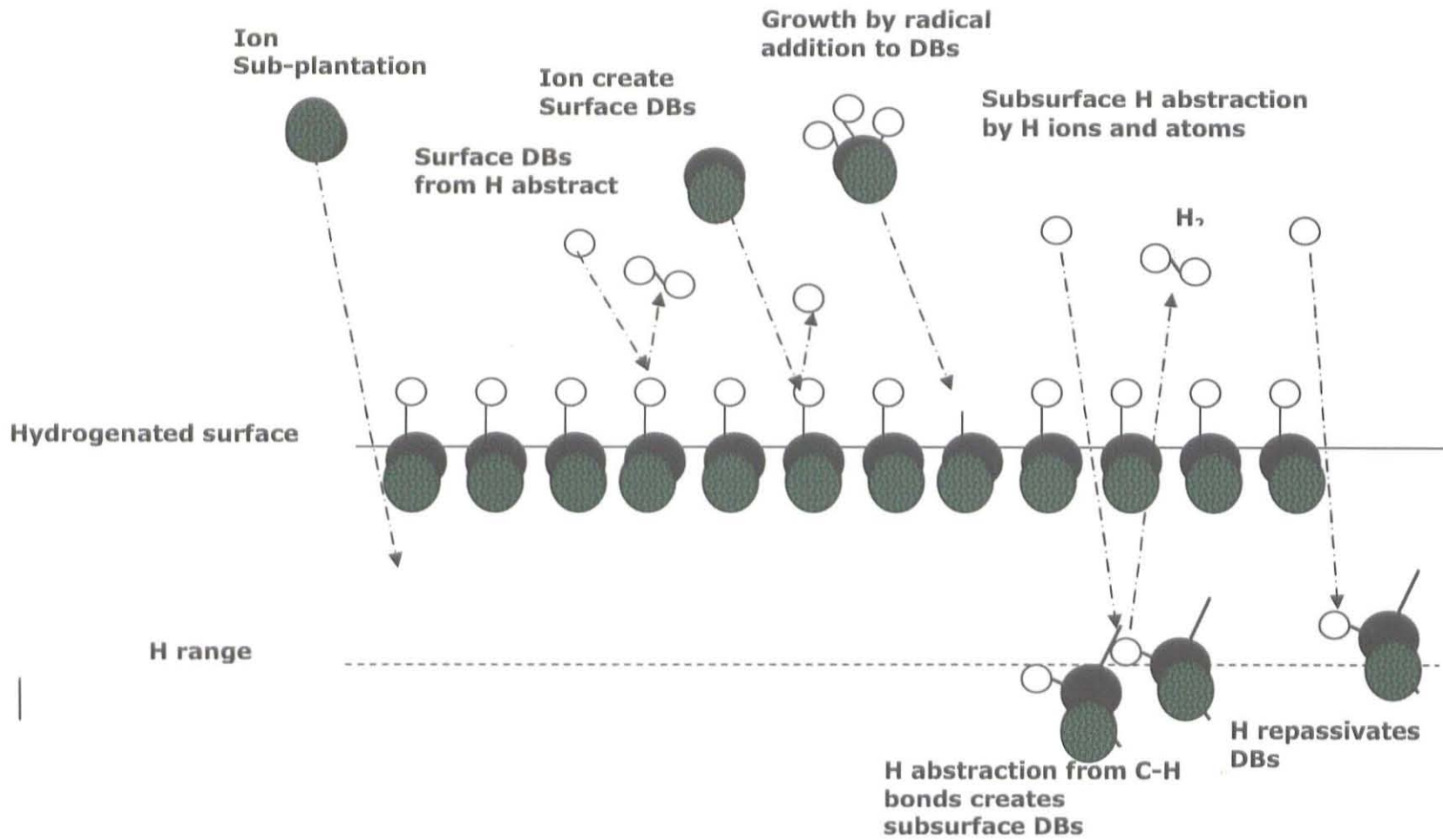


Figure 7: Schematic component processes during the growth phase of an amorphous C-H layer [J. Robertson-2002].

The rest of the ion energy dissipates as phonons. The whole process consists of 3 phases, (i) a collisional phase of 10^{-13} s, (ii) a thermalization phase of 10^{-12} s and (iii) a relaxation phase after 10^{-10} s. The two last processes allow the excess density to relax and cause a loss of sp^3 bondings at higher ions energies.

2.1.2. Properties of DLC

To locate the DLC within the carbon family, it is necessary to consider the diamond as the reference material. Diamond is the hardest material with a density as much as 3.5 g/cm^3 combined to a molar density of $0.293 \text{ g-atom/cm}^3$, associated with a room temperature specific heat of about 6.195 J/mol K and a bulk modulus of $4.4\text{-}5.9 \times 10^{11} \text{ N/m}^2$ in addition to a very large band gap of $E_g = 5.5 \text{ eV}$. In such a diamond structure, each an every atom is bonded to other four atoms [Figure 1] via a strong σ bonding and therefore it has short covalent C-C bonds of about 0.14 nm [Gop-2002]. While graphite is known as soft and stable materials with hexagonal arrangement of carbon atoms with weak π bonds which are perpendicular to the plane. As underlined previously, the structure of amorphous carbon consists of random network of sp^2 and sp^3 atomic coordination which are signature of (e.g. graphite) [Sun-2002, Gop-2002]. Carbon containing low degree of sp^3 bonding has low density $1.6\text{--}2.2 \text{ g/cm}^3$, 30 GPa and optically opaque with a band gap of $< 1.4 \text{ eV}$. Sp^3 bonding rich carbon of about 75% such as DLC exhibit high density of $2.8\text{--}3.4 \text{ g/cm}^3$, with hardness in the range of $50\text{--}100 \text{ GPa}$ and are optically transparent, with a medium range band gap of about $1.7\text{--}2.3 \text{ eV}$ [Mul-1999]. Riedo et al [Rie-2000] have reported that DLC grown by pulsed laser deposition «PLD» at base pressure of $1.5 \times 10^{-7} \text{ Pa}$ using Nd:YAG laser source at relatively higher laser fluence produce films containing as much as

53% of sp^3 bonding carbon population. Bonelli et al [Bon-2002] reported that high sp^3/sp^2 bond ratio of the films in optimized Hydrogen rich atmosphere depend mainly on the laser fluence and is characterized by a threshold phenomenon. The structure of the films deposited on silicon by PLD at a pressure of 10^{-2} Pa has threshold fluence $\approx 5 \text{ Jcm}^{-2}$ and display the signature of ta-C on the films with high sp^3 , containing low macroscopic stresses ($< 2 \text{ GPa}$) and hardness of about 70 GPa [Che-2002].

2.1.3. Surface properties

The name diamond-like carbon has been coined as results of its abilities to provide excellent properties similar to diamond on the surface. However the properties on the surface of the diamond-like carbon depend up on the deposition conditions for specific industrial applications [Kri-2002, Sun-2005]. An amorphous carbon or hydrogenated carbon high fraction of sp^3 is called diamond-like carbon, since is highly bonded a-C up to (80-90) % bonding of sp^3 , hence ta-C:H is hydrogenated in nature. Both a-C and ta-C:H has structure similar to a-Si where the atoms are in a random arrangement [Rob-2001].

The bond types have an effect on the material properties of amorphous carbon films. If the sp^2 type is predominant the film will be softer with lower density which caused by the termination of H, if the films contains relatively high H content of about 40-60 at % the films will have high sp^3 (70%) type is predominant the film will have better mechanical properties [Cin-2007].

2.1.4. Mechanical properties

Diamond-like carbon has excellent mechanical properties including high hardness, high wear resistance, low friction coefficient and high ratio of elastic modulus to the density. These properties make diamond-like carbon suitable for use in various applications such as coating for hard disks, speaker diaphragms or surface acoustic wave devices. It is essential to study the elastic properties and the hardness of diamond-like carbon films for these applications. As the result of the elastic properties DLC will be useful in application for micro-electromechanical systems (MEMS) [Sun- 2005]. The mechanical properties of the films are different from the bulk materials as the result of the defects or texture in the films due to the isolated sp^3 or dangling bonds. Raman spectroscopy is useful technique to give significant information of the sp^2 configuration [Sun-2005, Rob-2001].

Hardness is defined as the measure of the yield stress of a material [Rob-2002]. The most common mechanical properties of DLC films such as the hardness and the young's modulus are due to its strong and the directional sp^3 bonds. The σ bonds of the graphitic bonding or the C-H bonds of hydrocarbon polymers do not influence the modulus since they do not have the abilities form a three dimensional network [Rob-1994].

The nano-hardness and young's modulus of DLC films are 15.9GPa and 135GPa, depending on the deposition of condition such the decrease of bias voltages. The nano-hardness of a-C:H deposited in the atmosphere of methane has the maximum value of 17GPa [Yan-2004] and the hardness of DLC films with the value of 20GPa caused by low amount of hydrogen content [Rob-2002]. Nitrogen has a great effect on DLC films ECR-CVD. The hardness and Young's

modulus of nitrogen doped-DLC films is decrease from 29.18 GPa down to 19.74 GPa and 193.03 GPa down to 144.52 GPa by reducing the flow rate of nitrogen gas [Hua-2007].

The synthesized DLC film is usually affected by the compressive stress especially the thickness [Rob-2002]. The high compressive stresses have been studied by many researchers, producing DLC films which are deposited on various substrates like glass, silicon, stainless steel, etc. The residual internal stress has been found dependent up on the thickness of the films and increases with the thickness. The high internal or residual stress affect the film when is used for hard coatings by reducing the adhesion strength, microhardness, and wear resistance [Sam-1999, Sum-1998]. The internal stress and adhesion are the two aspects which depend on the stability of the film and substrate [Hid-1999, Yan-2004]. As the results of high internal stress the DLC films become hard and peel off from the substrate [Kul-2000]. There are two conditions governing the peeling of the films:

1. By lowering peeling thickness it shows that the internal stress and the quality of the coating (sp^3) is high.
2. The other case when the peeling thickness is higher it shows that the internal stress the quality of the coating is lower.

The peeling of the films is measured by stylus profiler essential for surface topology [Esa-2006]

Friction is defined as the dissipation of energy as two surfaces move over each other. The friction is caused by the contact of two surfaces just at a few high points or asperities. The friction force is due by several aspects such as adhesion, deformation or abrasion at the contact.

Given the fact that A is area of contact and Y the shear strength of the contact, therefore the lateral friction force is given by:

$$F = AY \dots\dots\dots \text{Equation 1}$$

The true area of contact arise from the load W together with real contact pressure, which is equal to the hardness of the softer material H , then load W is expressed as:

$$W = AH \dots\dots\dots \text{Equation 2}$$

Whereby H is related to the share strength by $H = cY$, and $c = 3-5$, then the coefficient of friction μ is written as $\mu = \frac{F}{W} = \frac{Y}{H} \approx 0.2$. The coefficient of friction μ depends on the humidity. The literature also explains that the coefficient of friction of ta-C is larger compared to that of a-C:H in the vacuum about 0.1 to 0.15. Xiao Liu et al [Xia-2002], report that the internal friction Q_{osc}^{-1} changes by the deposition of thin film onto the oscillator. The internal friction Q_{film}^{-1} of the thin film can be calculated with respect to the internal friction of the substrate Q_{sub}^{-1} , considering the increase above the bare oscillator (substrate) internal friction, therefore the internal friction of the film is calculated by

$$Q_{film}^{-1} = \frac{G_{sub} t_{sub}}{3G_{film} t_{film}} (Q_{osc}^{-1} - Q_{sub}^{-1}) \dots\dots\dots \text{Equation 3}$$

Where t and G represent the thickness and shear moduli of substrate and film, $G_{sub} = 6.2 \times 10^{11} \text{ dyn/cm}^2$ and is described as shear modulus of silicon along the direction of $\langle 110 \rangle$, for DLC films, G_{film} is given by $3.4 \times 10^{12} \text{ dyne/cm}^2$. Ronkeinen [Hel-2001] report that ta-C coating has stable friction performance if its coefficient of friction

against the steel pins is in the range of 0.14 to 0.19. In the past years, scientist participated in the Frontier Carbon Technology Project of NEDO produces low-friction and low-wear of DLC films together with DLC films rich in adhesion strength. DLC films with low-friction and low-wear rich in superior tribological properties were obtained by CVD methods [Waz-2005].

The wear property of DLC films such friction coefficient measurement depend on the nature of the film as well as the tribotesting conditions. For example the friction coefficient of hydrogenated a-C:H films in vacuum is low compared in ambient conditions (20% < Relative Humidity < 60%) from the range from 0.007 to 0.02 and 0.1 to 0.4. Hydrogen in the film increases the friction coefficient, hence hydrogen free exhibit lower friction of < 0.15 [Kri-2006]. Sinul Kumar Pal [Sun-2002] find wear rate of the value of 10^{-6} & $10^{-8} \text{ mm}^3 / \text{Nm}$, also mention that the instruction of Si or metal improves the adhesion behavior which also cause the reduction of wear between substrate and DLC films. The wear behavior of DLC coatings affected by the nature of films and tribological testing conditions [Sun-2002] such as:

- (a) Mechanical parameters: type of contact and contact pressure
- (b) Kinematic parameters: nature of motion, velocity
- (c) Material parameters: nature of substrate and pin material
- (d) Physical parameters: temperature during friction
- (e) Chemical parameters: nature of environment i.e. humidity, dry etc.

The wear rate of DLC films is in the range of $10^{-7} \text{ mm}^3 / \text{N.m}$ to half of $10^{-8} \text{ mm}^3 / \text{N.m}$ reported by Wazumi Kouichirou et al [Waz-2005].

2.1.5. Optical properties

Diamond-like carbon is a metastable amorphous material with small band gap of 2.0-2.5eV compare to diamond of 1.2-5.5eV. Diamond-like carbon film is characterized by its transparency in the infrared whereby it transmit less about 70%-75% at 2900 cm^{-1} compare to the films deposited on quartz substrate [Rob-2002, Kon-2000*, Gri-1999, Hua-2004]. DLC film is weakly absorbing in the visible range and increases the absorption in the U-V in the range of 200nm-800nm [Gri-1999, Hua-2004]. The optical properties of diamond-like carbon such the index of refraction known as real part (n) and the excitation coefficient (K) also called imaginary part both depend on the deposition parameters and the amount of hydrogen incorporated with the films. Diamond-like carbon exhibit the index of refraction of 1.7 to 2.4 at 632 nm which is influence by hydrogen content, as the hydrogen content decreases the index of refraction increases. Hence, the higher is the index of refraction indicates the quality of the films i.e. stronger cross, higher hardness, and better wear resistance [Gri-1999].

Hydrogen free a-C exhibit higher refraction index of 2.71 compare to the film produced in an atmosphere of hydrogen. The mixture of acetylene and hydrogen above 67% reduces the refractive index of the film from 2.71 to 2.05, this indicate that hydrogen concentration has enormous influence on the optical properties of the film [Šil-2005]. DLC is used in various optical applications due to its transparency over the IR region. For example antireflective and scratch resistance for wear protective coatings for IR optics at the wavelength of $8\text{-}13\mu\text{ m}$ made of Ge, ZnS, ZnSe. The function of DLC on the optics mentioned above is to protect them against corrosion, rain impact, as well as Al mirrors for thermal imaging systems against deterioration in certain condition [Gri-1999].

CHAPTER 3

3. Diamond-Like Carbon by non radiative deposition techniques

The deposition of DLC nano-structures and thick coatings was first performed by Aisenberg in early 1970s using ion beam deposition methodology [Sta-1998, Hel-2001 Sun-2004]. Nowadays various synthesis techniques are used to grow high quality DLC films such as the popular pulsed laser deposition «PLD» [Yib-2003], ion beam deposition «IBD», radio-frequency and magnetron sputtering, as well as chemical vapor deposition «CVD» [Joh-2006]. In addition to this initial list of non-equilibrium techniques, plasma enhanced chemical vapor deposition «PECVD» [Sum-1998, Sam-1999, Rie-2000, Pan-2003, Sun-2004] which is used to coat very large and complexes shaped surfaces. Sean Pearce [Sea-2003] revealed that medium energy ions of about $\approx 100\text{eV}$ will provide good quality DLC films. Naturally, there are other synthesis techniques which have been used to synthesize DLC films among them one could quote: Mass Selected Ion Beam «MSIB» and cathodic arc discharge.

3.1. Ion Beam Deposition

The ion beam deposition «IBD» type of method was the pioneering technique used to synthesize the first series of DLC nano-structured coatings by Aisenberg and Chabot. The ion beam deposition «IBD» consists of using 2 different ion sources: an injected hydrocarbon gas as precursor of hydrogen and a solid carbon target being sputtered.

In a typical standard production of DLC, methane gas is released with a suitable flow, whereby the graphite target creates relatively amount of solid phase ion source [Sea-2003]. While the IBD combines both the advantages of the physical vapor deposition and chemical vapor deposition techniques, the synthesis of hard films is very difficult at relatively high power/high pressures [Joh-2006]. The common feature of this method is that the DLC film is condensed from a beam containing medium energy ~ 100 eV carbon or hydrocarbon ions. Via their impact on the growing film that causes the sp^3 bonding formation. This physical process contrasts with the chemical vapor deposition of diamond in which a chemical process stabilizes the sp^3 bondings. It was found that the optimal conditions provide a carbon ion flux at about 100eV per carbon atom, with a narrow energy distribution in addition to the single energetic species and a minimum number of non energetic species. In a typical IBD set up, a hydrocarbon gas such as CH_4 is ionized in a plasma.

An ion beam is extracted through a grid from the plasma source via a bias voltage. The carbon ions or hydrocarbon ions are accelerated to constitute the ion beam in the high vacuum deposition chamber. The ion source runs at a finite pressure, so that the beam contains a large flux of non ionized neutral species. This can reduce the flux ration of ions to neutrals to as low as 2-10%. The best conditions of IBD deposition are obtained at higher ion energies within the range of 100-1000 eV.

3.2. Plasma Enhanced Chemical Vapor Deposition

The Plasma Enhanced Chemical Vapor Deposition «PECVD» is known as a popular adequate growth method at relatively high temperature. The charged and neutral particles that form during the production of the films by CVD are governed by random collision process and are often electrically neutral on average [Joh-2006]. Various hydrocarbon source materials are used as suitable precursors to generate both carbon and hydrogen species such as methane, ethane, acetylene, benzene, ethylene, propane, isopropane, etc.... The production of DLC films by bombarding hydrocarbon using CVD is possible if the substrate has impact energies ranging from 50eV to < 1000eV. At the bias voltage of about $\sim -100V$, DLC films does not depend upon the hydrocarbon sources [Sun-2004]. The reagents formed as a result of the volatile chemical vapour reaction between the precursors are decomposed and grown onto the substrate heated to high temperature. This type of deposition method allows the possibility to grown good quality films uniform in thickness. In addition to the high rate of deposition, the CVD permits to coat very complexes shaped surfaces. The major limitation of this technique is the high temperature of the growth surface i.e. the substrate. Hence, polymeric and low melting point substrates cannot be coated with such a method.

3.3. Sputtering Deposition

The third usually used technique for the DLC synthesis is the sputtering approach. In this whereby the target i.e. graphite, is bombarded with inert gas ions such as Argon, the sputtered atom, ions and atom cluster originating from the target are directed to the surface of the substrate via an applied voltage. There are several sputtering variations corresponding to different configurations. Among them, one could quote the standard magnetron and radio-frequency sputtering. This sputtering approach allows high yield of DLC and uniform coatings with good adhesion [Joh-2006, Sea-2003]. The sputtering is the most widespread industrial process for the deposition of DLC. The most universal configuration is the magnetron sputtering because of the low sputtering yield of graphite. External magnets are placed surrounding the target to induce a spiral motion of the electrons in the plasma due to the Lorentz force so increase their path length and hence the ionization rate in the plasma. As ion bombardment enhances the formation of sp^3 bonding, the magnetic field can be configured to pass across the substrate, so this causes the Ar ions to also bombard the substrate. A DC bias can be applied to the substrate to vary the ion energy and to avoid localized charge effects. The a-C:H is produced by reactive sputtering by using a plasma of Ar and hydrogen or methane. An alternative version consists of bombarding with Ar ions beam the graphite target to create the carbon flux. A second Ar ion beam is used to bombard the growing film, to densify it and to favor the formation of sp^3 bondings. It is called ion beam assisted deposition or ion plating. Even if it is the preferred industrial technique which is easily scaled up, it has a relatively low ratio of energetic ions to neutral species and hence, it does not produce the hardest DLC coatings.

3.4. Diamond-Like Carbon by Pulsed Laser Deposition

Pulsed laser ablation «PLD» is the unique synthesis technique which relies of an intense photonic beam to create plasma as the ones obtained in the non radiative based techniques mentioned previously. Pulsed laser deposition is for many reasons a versatile technique. Since with this method the energy source is located outside the chamber, the use of ultrahigh vacuum as well as ambient gas is possible. Combined with a stoichiometry transfer between target and substrate this allows depositing all kinds of different materials, e.g., high-temperature superconductors, oxides, nitrides, carbides, semiconductors, metals and even polymers or fullerenes can be grown with high deposition rates. The pulsed nature of the PLD process even allows preparing complex polymer-metal compounds and multilayers.

In UHV, implantation and intermixing effects originating in the deposition of energetic particles lead to the formation of metastable phases, for instance nanocrystalline highly supersaturated solid solutions and amorphous alloys. The preparation in inert gas atmosphere makes it even possible to tune the film properties (stress, texture, reactivity, magnetic properties...) by varying the kinetic energy of the deposited particles. All this makes PLD an alternative deposition technique for the growth of high-quality thin films in particular DLC type nano-structures. A specificity of the PLD is the several physical phenomena which take place during and after the generation of the plume following the laser beam-target interaction, in particular the shock wave and its effect on the velocity distribution and its angular geometry. The high fluence of

the laser beam and the shock wave as well as the photonic radiations of the substrate could induce high pressure-high temperature conditions suitable and ideal for the synthesis of dense carbon with sp^3 type bondings. As shown in Figure 11. The shock wave area is situated within the region of 200-400 kBars and 1000-2100°C in term of pressure and temperature. This region matches within the diamond zone of the P-T phase diagram. Consequently, due to the local high intensity of the laser during its interaction with the graphite target and the shock wave generated during the plasma generation/expansion, the pulsed laser deposition would be an ideal synthesis tool of DLC films in presence of a hydrogen rich atmosphere. This is why this processing technique is considered in this research work to synthesize DLC nano-structures.

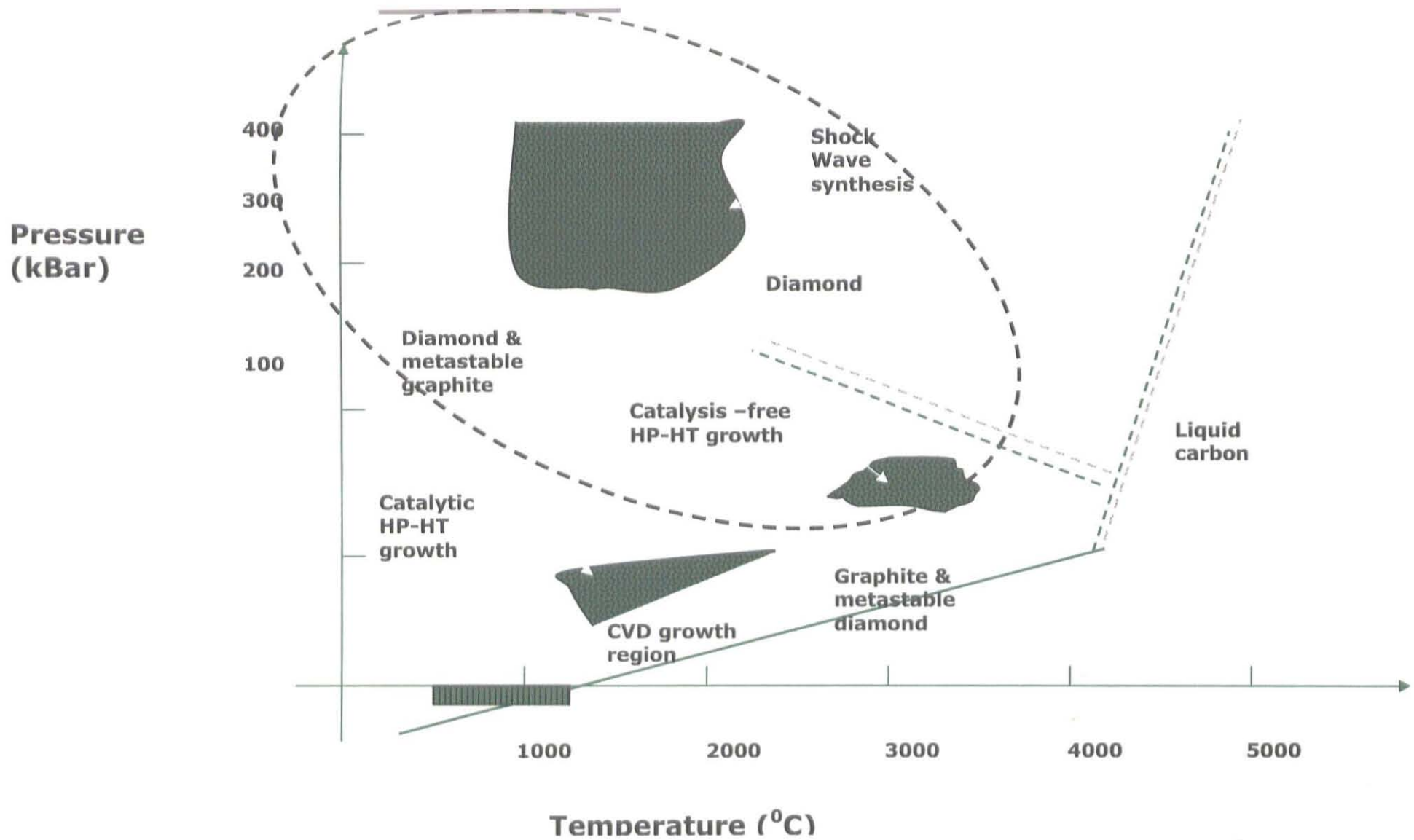


Figure 8: High pressure-high temperature phase diagram of carbon.

From historical viewpoint, the interaction of a laser radiation with solid surfaces was investigated as early as 1962, when Breech & Cross analyzed the emission spectrum of material vaporized by laser pulses. The first demonstration of PLD, in 1965, did not unfortunately produced significant interest, as the films deposited were inferior to those obtained via other deposition techniques, such as chemical vapor deposition or molecular beam epitaxy. The technique remained dormant for approximately the next twenty years until Dijkamp and Venkatesan used PLD to grow a film of high temperature superconducting complex material $\text{YBa}_2\text{Cu}_3\text{O}_7^+$. The superconducting films obtained were found to be superior in quality to those previously grown using other deposition methods and triggered worldwide interest in the technique. Currently, research applications include growing films for magneto-optic storage devices, developing multilayer devices for x-ray optics and depositing diamond films on components for protection and insulation.

Relatively to the standard thin films techniques, in principle PLD is an extremely simple technique, which uses pulses of laser energy to remove material from the surface of a target yet the source creating the plasma is spatially and physically isolated from the vacuum chamber where the target is located. The vaporized material originating from the target, containing neutrals, ions, electrons etc., is known as a laser plasma plume and expands rapidly away from the target surface «velocities typically $\sim 10^6$ cm/s in vacuum». Film growth occurs on a substrate upon which some of the plume material recondenses. In practice, however, the situation is not so simple, with a large number of variables affecting the properties of the film, such as the laser fluence, the background gas pressure and the substrate temperature in addition to the target-

substrate distance. These variables allow the film properties to be manipulated with a certain degree of flexibility, to suit targeted applications yet the mechanisms of pulsed laser ablation are complex. Indeed during such a laser-target interaction, numerous events can take place which mainly are (Figure 12):

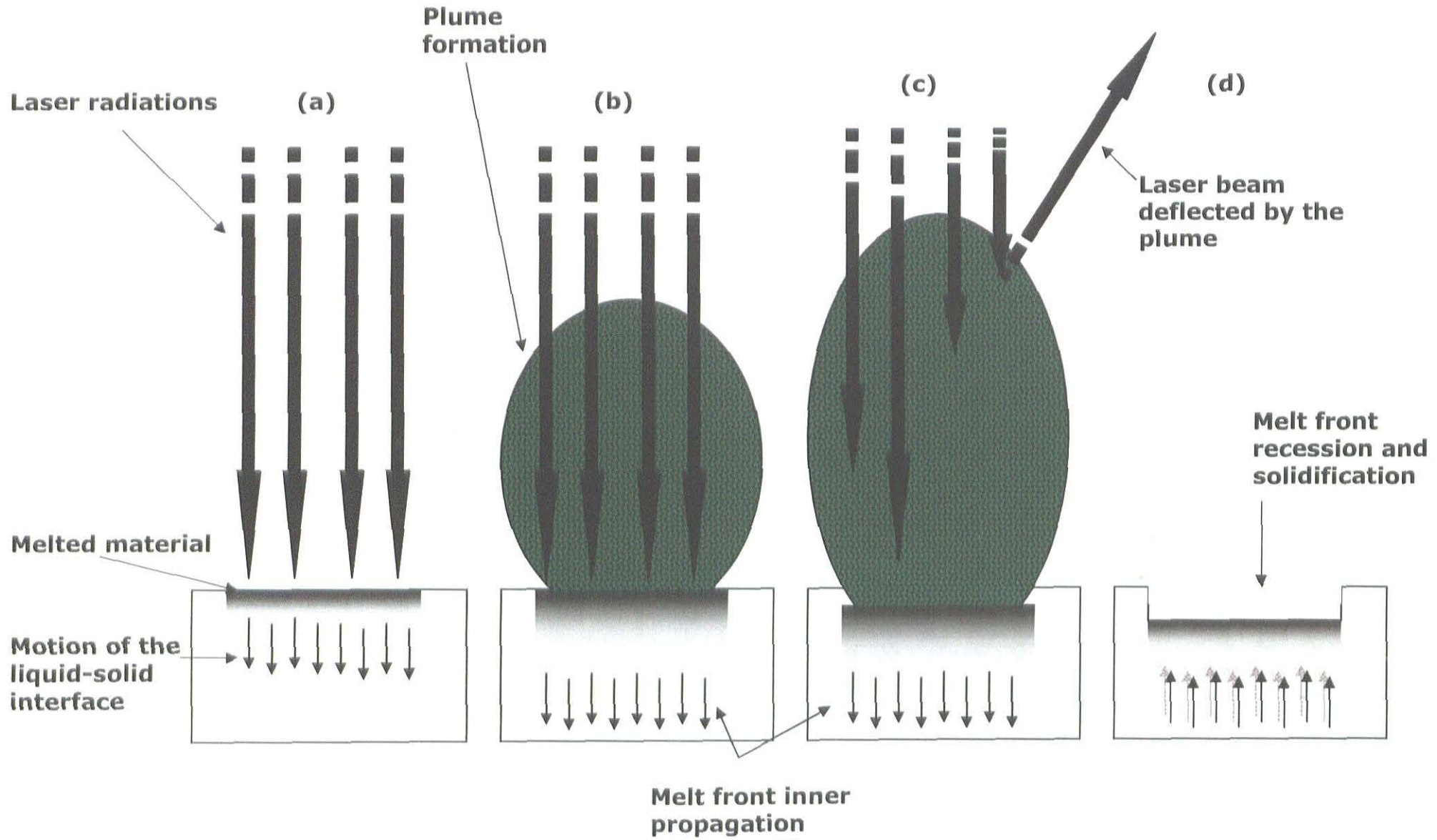
- (i) Collisional sputtering
- (ii) Thermal Sputtering
- (iii) Electronic Sputtering
- (iv) Exfoliation Sputtering
- (v) Hydrodynamic Sputtering

The interaction between laser pulses and the target depends strongly on the intensity of the incoming laser beam. Classically and excluding femtosecond laser sources, the intensity is on the order of $10^8 \sim 10^9$ W/cm corresponding to a pulse duration of a few nanoseconds. Therefore, there is enough time for the pulses to absorb and heat the target surface, and finally, lead to the removal of matter. As mentioned just before, there are many different mechanisms through which energy can be transferred to the target:

Firstly, in the so called collisional sputtering, the momentum of the incident beam is transferred to the target, which results in an ejection of particles from the surface. The mechanism is of great importance if the incoming beam consists of massive particles, such as ions. In the case of photons, the maximum transfer of energy is negligible.

Figure 9: Schematic illustration of the time scale key phases of the PLD

TIME →



Secondly, in the so defined as thermal sputtering, the absorbed laser beam melts and finally vaporizes a small area of the target material. The surface temperature of the target is typically above the boiling point of the ablated material but the observed material removal rates typically require even higher temperatures. Therefore, the mechanism can only partly explain the formation of the ablation cloud.

Thirdly, the so called electronic sputtering is considered to be the principal interaction mechanism of a laser pulse with the target. The mechanism is not a single process but rather a group of processes, all of which have the common feature of involving some form of excitations and ionizations. Such processes take place at different time scales as illustrated in figure 12. This later gives schematically the key elements of the PLD during the laser beam-target interaction. Within the time scale, (a) Initial absorption of the laser radiation indicated by long arrows where melting and vaporization begins. The shaded area indicates melted material while short arrows indicate the motion of the solid-liquid interface. (b) Illustrates the melt front during its propagation into the inner part of the solid target where vaporization continues and the laser-target interaction starts to become important. In (c), the absorption of the incident beam by the plume and plasma formation. During stage (d), the melt front recedes to eventual re-solidification. More accurately, the incident photons strike the target, producing electron-hole pairs and electronic excitations in a 10^{-15} s timescale. After a few 10^{-12} s, the energy is transferred to the crystal lattice, and during the laser pulse, within a few ns, a thermal equilibrium between the electrons and the lattice is reached.

- (i) Neutral atoms,
- (ii) Electrons,
- (iii) Ions.
- (iv) Clusters of different compounds of the target elements are observed near the target surface.

The visible light of the plume is due to fluorescence phenomena and recombination processes in the plasma. Although atomic transitions have typical lifetimes of a few 10^{-9} s, collisions can re-excite atoms such that the emission lines are observed many 10^{-6} s after the initial laser pulse.

The fast and strong heating of the target surface by the intense laser beam, typically up to temperatures of more than 5000K within a few ns, corresponding to a heating rate of about 10^{12} K/s) ensures that all target components irrespective of their partial binding energies evaporate at the same time. When the ablation rate is sufficiently high «which normally is the case at laser fluences well above the ablation threshold», a so-called Knudsen layer is formed and further heated «for instance by Inverse Bremsstrahlung» forming a high-temperature plasma, which then adiabatically expands in a direction perpendicular to the target surface. Therefore, during PLD, the material transfer between target and substrate occurs in a material package, where the separation of the species is small. The expansion of the whole package can be well described by a shifted Maxwell-Boltzmann center-of-mass velocity distribution as given by:

$$f(v_z) \propto v_z^3 \exp[-m_A(v_z - v_{cm})^2 / (2k_B T_{eff})] \dots \dots \dots \text{Equation 4}$$

with a center-of-mass velocity v_{cm} and an effective temperature T_{eff} . Then, adiabatic collisionless expansion occurs transferring the concentration of the plasma plume towards the substrate surface. Thus one can understand that complex structures such as oxides or perovskites are built up again at the substrate surface, when the substrate temperature is high enough, because all components are transferred from target to substrate at the right composition. In the case of DLC deposits, as in the case polymers, the substrate should stand at relatively adequate temperatures.

In terms of components and equipment, a PLD unit requires a laser source which for the DLC films is optimally an excimer sources i.e. emitting in the UV spectral range and an ensemble of optics consisting of a series of lenses and apertures, mirrors, beam splitters, a laser Windows and a deposition system. This later consists of a vacuum chamber, a target manipulation system, a substrate holder and heaters as well as pumps, gas flow, and vacuum gauges and particle filters. Generally excimer laser sources are used. Their wavelengths are as follows: XeF 351 nm, XeCl-308 nm, KrF-248 nm, KrCl-222 nm and ArF-193 nm.

The capability for stoichiometric transfer of material from target to substrate, i.e. the exact chemical composition of complex materials such as complex oxides, can be reproduced in the deposited film. Relatively high deposition rates, typically $\sim 10\text{nm}/\text{min}$, can be achieved at moderate laser fluences, with film thickness controlled in real time by simply turning the laser on and off. The fact that a laser is used as an external energy source results in an extremely clean process without filaments. Thus deposition can occur in both inert and reactive background gases.

The use of a carousel, housing a number of target materials, enables multilayer films to be deposited without the need to break vacuum when changing between materials.

The plasma plume created during the laser ablation process is highly forward directed, therefore the thickness of material collected on a substrate is highly non-uniform and the composition can vary across the film. The area of deposited material is also quite small, typically $\sim 1\text{cm}^2$, in comparison to that required for many industrial applications which require area coverage of $\sim (7.5 \times 7.5)\text{cm}^2$. The ablated material contains macroscopic globules of molten material, up to $\sim 10\ \mu\text{m}$ diameter. The arrival of these particulates at the substrate is obviously detrimental to the properties of the film being deposited. The fundamental processes, occurring within the laser produced plasmas, are not fully understood; thus deposition of novel materials usually involves a period of empirical optimization of deposition parameters.

Concerning the usage of the PLD to synthesize DLC nano-structures on non heated substrates, their qualities depend upon the kinetic of ablated carbon species and hydrocarbons formed within the plasma during their transit to the substrate as well as their degree of thermalization within the deposition chamber. In the PLD deposited carbon based nano-structures, 3 major mechanisms have to be considered. These 3 cases are illustrated by Figure 11. In the case of DLC coatings, most of carbon films produced at low energies (case 1) becomes more graphitic. The second case is an intermediate region where the carbon species have kinetic energies in the range of 10-100 eV. The last case where the particles with kinetic energies of greater than 100 eV can be produced [Jar-2000].

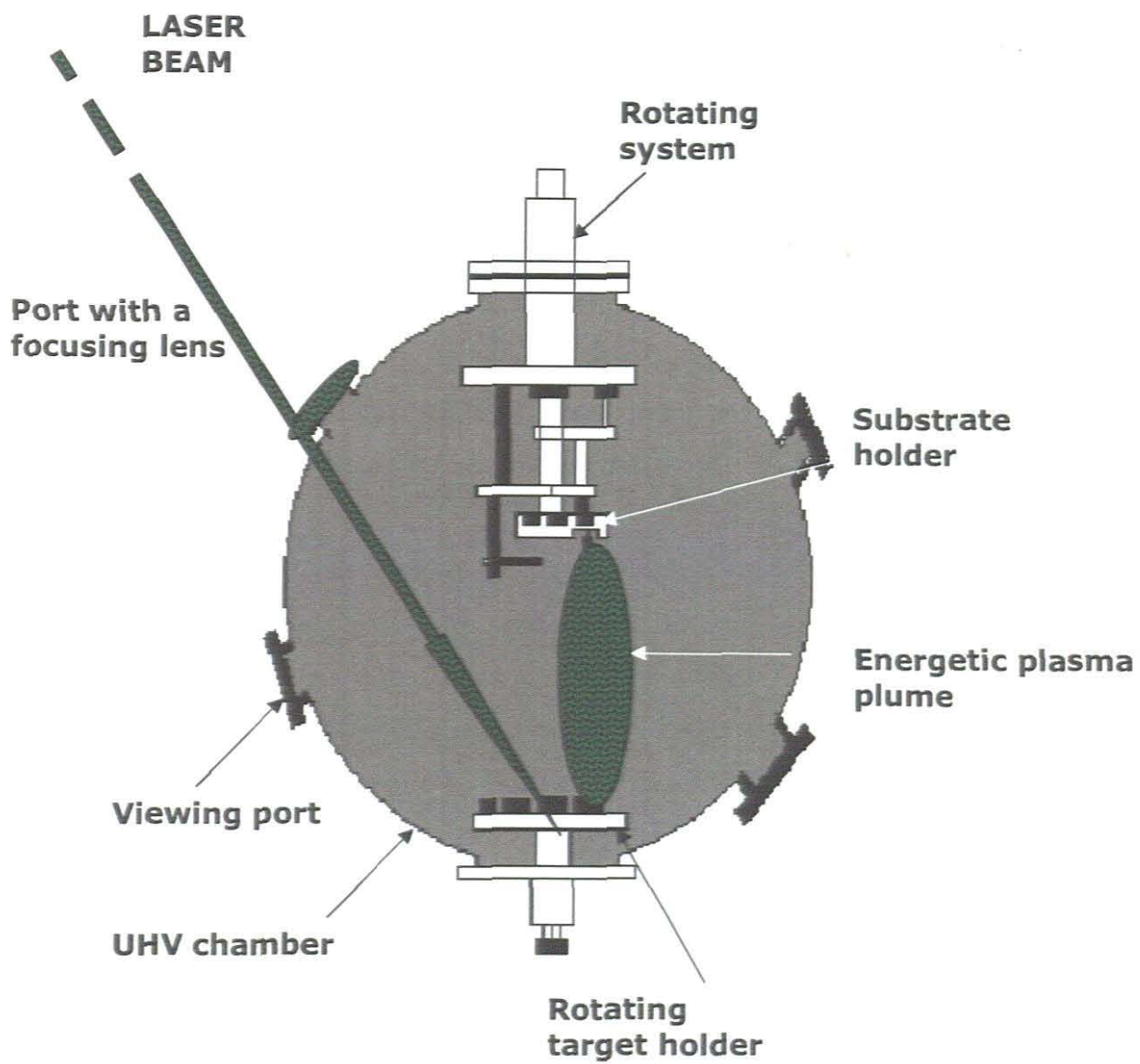
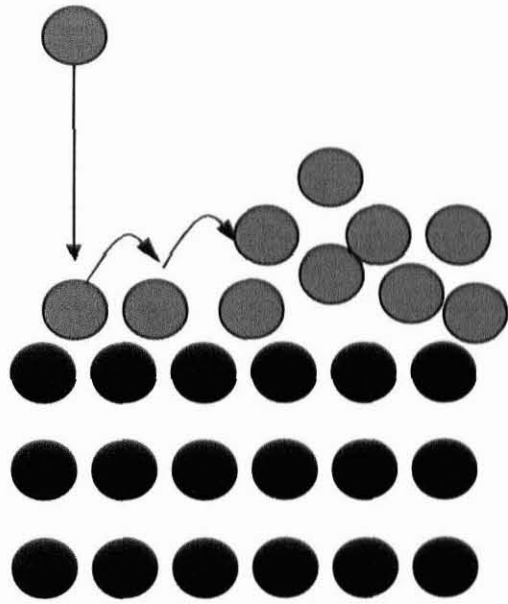


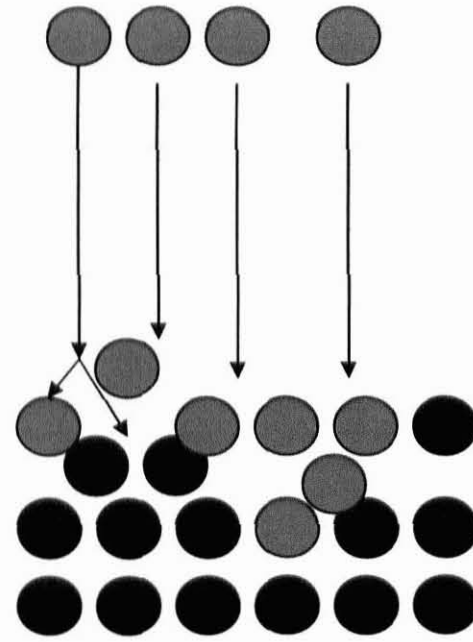
Figure 10: Schematic diagram of a standard apparatus of PLD.

The formation of DLC films is favored by the bombardment of carbon or hydrocarbon radicals onto a substrate with impact energies in the range of 50eV to several hundred of eV. The deposited film usually affected by the impact energy from the work of Angus et al and reported by Pankaj [Pan-2003] as shown in Figure 9. Hence the PLD is an adequate method for DLC synthesis.

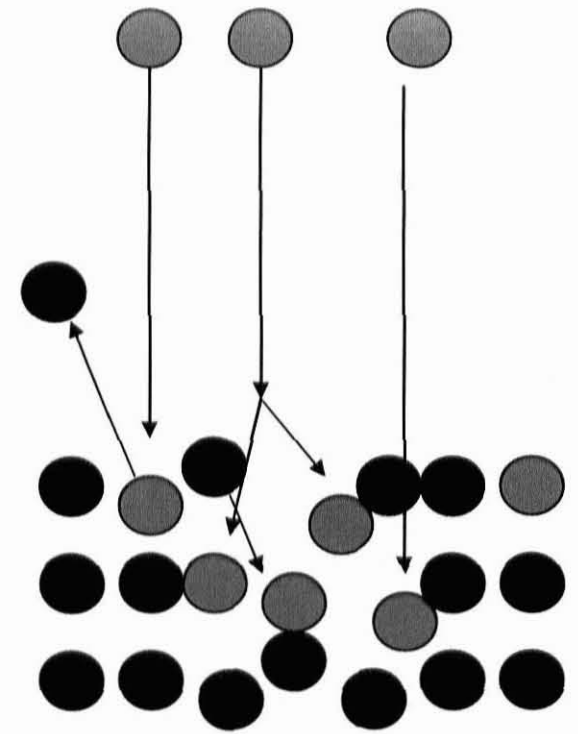
The production of diamond-like carbon by pulsed laser deposition was first performed by Marquardt et al [Hid-1999, Sta-1998], where they found that the transition of the carbon from soft to hard carbon was result by the increase in laser pulse power density over $\sim 5 \times 10^{10}$ for 6ns laser pulses at a wavelength of $\lambda = 1062$ nm using a Nd:YAG laser source [Hid-1999]. Yohanna et al [Yoh-2006] reported that PLD is able to produce DLC coatings with PLD can indeed produce ta-C films like other deposition methods such as MSIB and FCVA [Yib-2003, Jar-2000]. The review of producing carbon materials by PLD was reviewed extensively by Voevodin and by Siegal et al [Rob-2002]. PLD grow quality films with high sp^3/sp^2 bond ratio with low or no hydrogen content. Precursive species which has higher energies than other methods. Moreover PLD has ability to control the sp^3/sp^2 -ratio and therefore the properties such as hardness, Young's modulus, surface smoothness, optical gap, and conductivity. PLD produces excited species of high energies in the vapour/plasma plume [Yib-2003].



(a)



(b)



(c)

Figure 11: Three basic mechanisms of PLD film growth [Joh-2006].

PLD is able to grow DLC films at low deposition temperature and high rates at a vacuum ranging from 10^{-4} - 10^{-5} Pa due to controllable parameters [Sta-1998, Bon-2002] and can produce film at relatively high vacuum conditions by P. Fierlinger et al [Fie-2005/06]. Jarmo report that low substrate temperature and high thermal conductivity of the substrate are essential for DLC films growth [Jar-2000]. The production of high quality DLC films at room temperature by PLD in atmosphere filled with atomic hydrogen has higher resistivity than films without hydrogen [Sta-1998].

Helena Ronkainen [Hel-2001] report that the production of Diamond-like carbon hydrogen-free films by PLD has low coefficient of friction less than 0.1 in vacuum and 0.3 in an atmosphere of nitrogen, also mention that hydrogen-free carbon films by cathodic vacuum arc have less coefficient of friction ranging from 0.04 to 0.18 in ambient atmosphere. Camps E et al [Cam-2003] reported that PLD has ability to grow high sp^3/sp^2 bond ratio with or no hydrogen content and the film of the material depending on the deposition temperature. In the work of C.-L Cheng et al [Che-2001] it is report that the parameters of PLD such as laser wavelength and substrate temperature cause an effect on the properties and to the applications of DLC films. J Haverkamp et al [Hav-2003] found that DLC films deposited on silicon substrate at room temperature by PLD in the present of hydrogen,

have higher resistivity and low fraction of sp^3/sp^2 bonding of carbon of about 72.2% compare to the previous report of 80% or above, this results was obtained using EELS in TEM. The diagram of Figure 12 serves as a standard reference within the DLC community. This will be used within the framework of this research work.

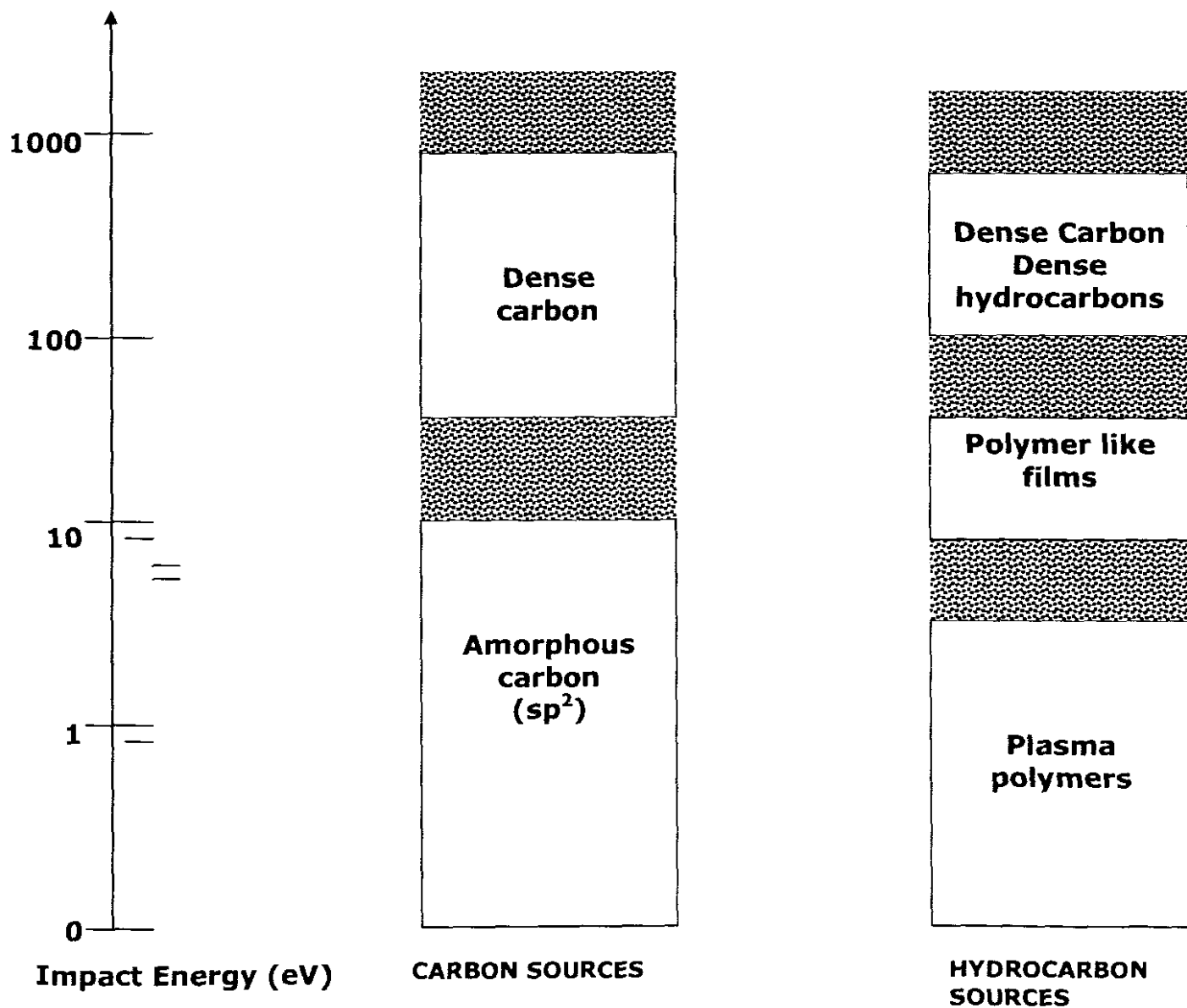


Figure 12: Influence of impact energy on type of carbon based film produced [after Pan-2003]

CHAPTER 4

4. USED CHARACTERISATION TECHNIQUES

4.1. SURFACE MORPHOLOGY

4.1.1. Scanning Electron Microscopy

Scanning Electron Microscopy «SEM» is used to study the surface topology, and provides information on the chemical composition of the sample surface [She-2005]. The principle of SEM is shown in figure 16. An electron beam originating by thermionic effect from a filament emitter «LaB₆» and focused via a magnetic lensing system is sent directly to the surface of the sample to be investigated [Joh-2006]. During the incident electrons-sample surface interaction, the electrons go via different physical interactions [All-2000]. These are mainly, (i) ionization followed by secondary electrons emission, (ii) backscattering electrons and (iii) X-rays emissions as well as (iv) Cathode-Luminescence phenomenon. When the sample surface is bombarded with electrons, the strongest region of the electron energy spectrum is due to secondary electrons.

The secondary electron yield depends on many factors, and is generally higher for high atomic number targets, and at higher angles of incidence. Secondary electrons are produced when the incident electron excites an electron in the sample and loses some of its energy in the process. The excited electron moves towards the surface of the sample undergoing elastic and inelastic collisions

until it reaches the surface, where it can escape if it still has sufficient energy.

Their energies are a function of the initial energy E_0 and the surface work function, which defines the amount of energy needed to remove electrons from the surface of a material. One of the major reasons for coating a non-conductive specimen with conductive materials such as carbon is to increase the number of secondary electrons that will be emitted from the sample.

Secondary electrons, by convention, are those emitted with energies less than 50 eV. This is only a small fraction of the electrons emitted from the sample. The mean free path length of secondary electrons in many materials is approximately about 1nm. Thus, although electrons are generated throughout the region excited by the incident electron beam, only those electrons that originate less than 1nm deep in the sample escape to be detected as secondary. This volume of production is very small compared with backscattered electrons and emitted X-rays. Therefore, the resolution using secondary electrons is better than either of these and is effectively the same as the electron beam size. The shallow depth of production of detected secondary electrons makes them very sensitive to topography and they are used for scanning electron microscopy. This superior SEM sensitivity is enhanced by using optimal secondary electrons collection system combined with an efficient detecting system covered by a Faraday cage as shown in Figure 13.

In this work a LEO S440 was used to determine the surface topology of the deposited DLC films by PLD. The operating voltage was about 10kV with a probe current of (20pA).

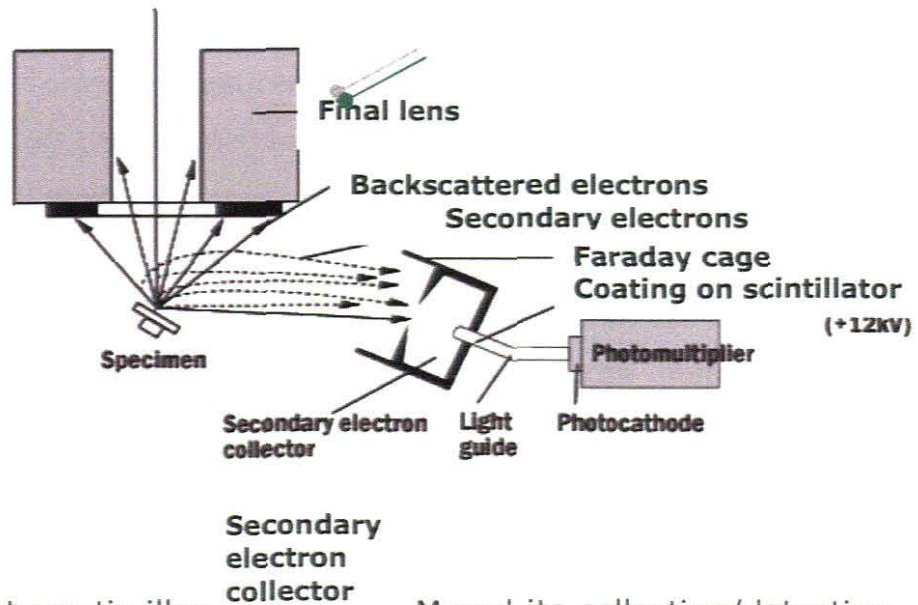
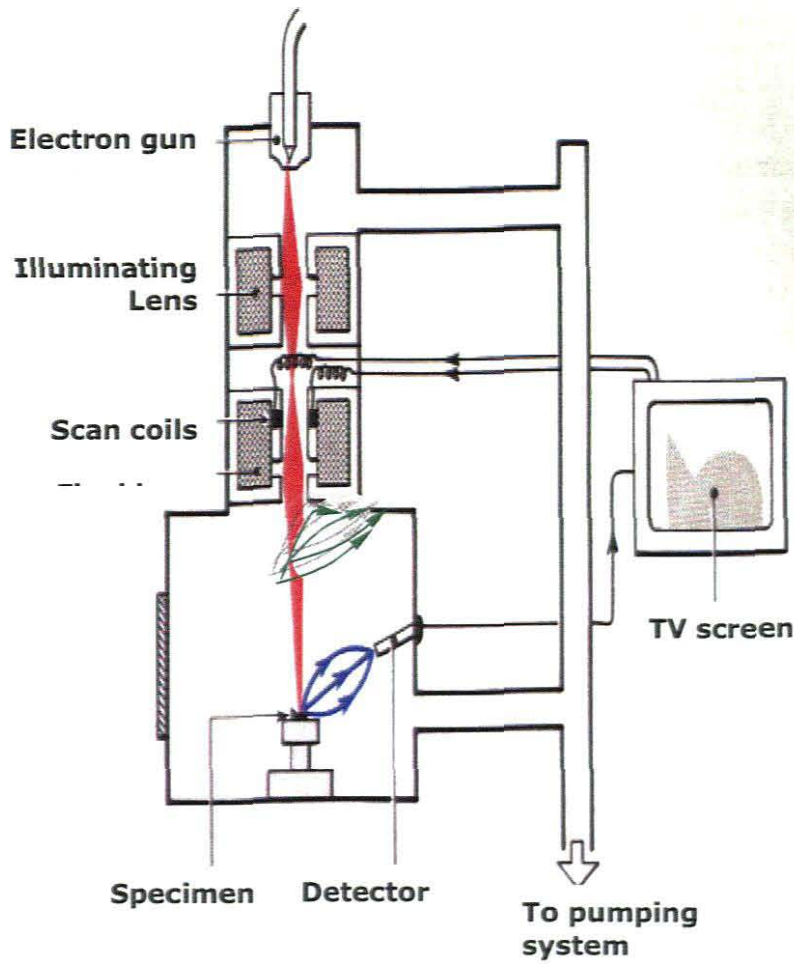


Figure 13: Schematic illustration of secondary electron detection and its collection/detection of secondary electrons emitted from the sample surface.

4.1.2. Surface Zygo interferometry

Zygo interferometer was used to study the structure of the DLC films. A white light Zygo interferometer is used determine the step heights, texture, roughness, and other surface topography parameters. Figure 14 shows the principle of the white light Zygo interferometer on how the data is collected from the specimen. It is a standard two-beam interferometer functioning by dividing originally coherent light into two beams of equal intensity, directing one beam onto the reference mirror and the other onto the specimen, and measuring the optical path difference «the difference in optical distances» between the resulting two reflected light waves. In order to implement this method, various instrument types have been devised, employing several devices to split the light wave and to provide the appropriate optical paths. In this case, the relationship between the reference mirror and the specimen is similar in principle in which the interference fringes successively appear as the height changes by $\lambda/2$.

In order to perform a measurement of the surface observed by the field of view of the objective, the objective lens is translated vertically and linearly so that the focal plane moves through the entire height range of the surface being measured. As it does so the interference fringes will move and follow the height profile of the surface and this information is processed by the instrument to calculate the height profile to a very high precision as it is based on the difference of optical path. If we take the simple example of a spherical surface and the objective moving downwards then the interference fringes will appear as a small set of concentric circles emanating from the top of the sphere as the focal plane of the objective intersects it as in the case of Newton rings. The concentric

fringes will then grow larger as the focal plane moves and intersects the sphere lower down. Software processes the interference data to create a colour coded height profile of the surface

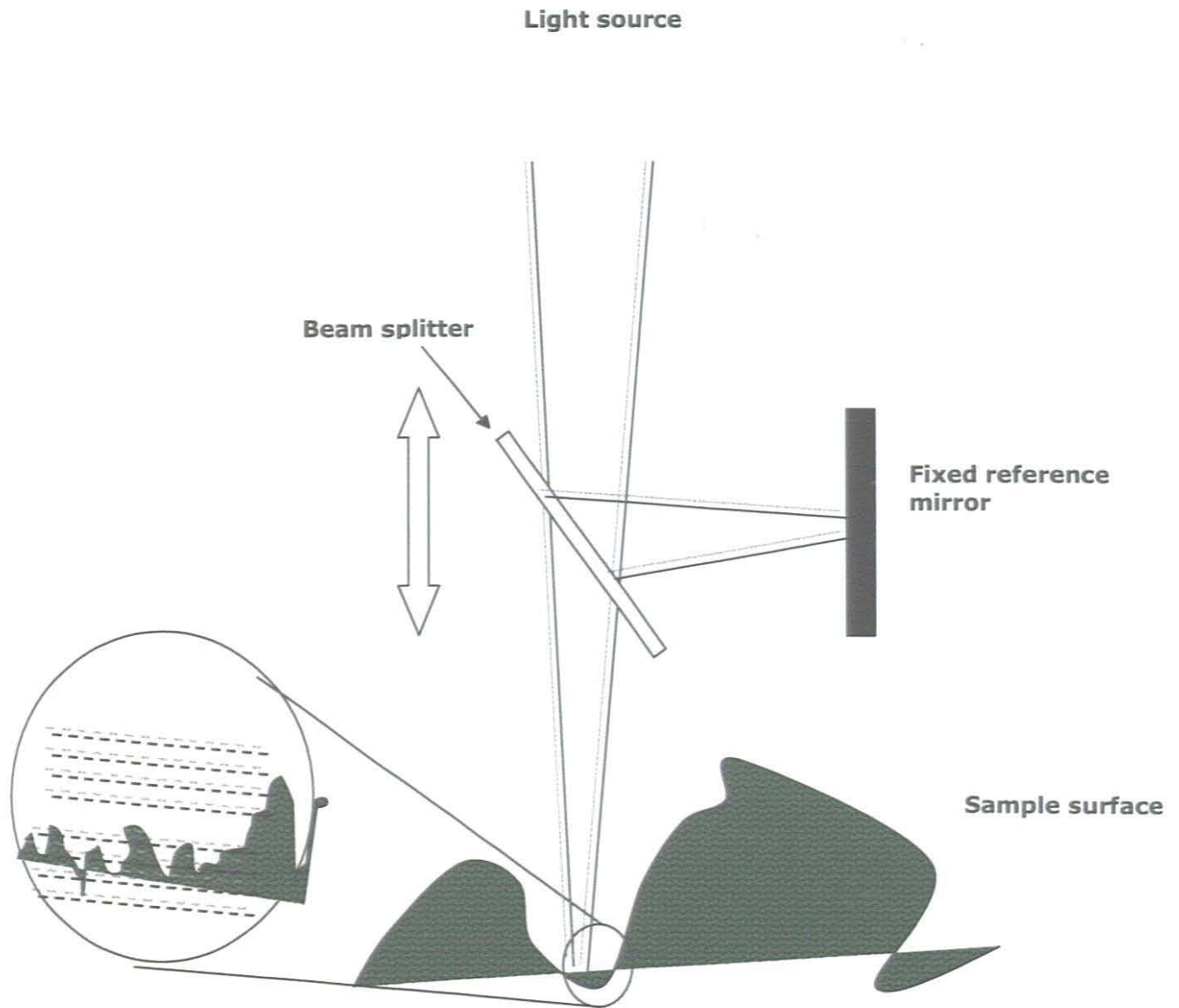


Figure 14: Schematic illustration of Zygo interferometer.

under measurement and thus roughness and waviness as well as sphericity of the sample surface can be deduced. The measurement of this research work were performed using non destructive white interferometer Zygo «MLIS-6891».

4.1.3. Surface Mechanical Profilometry

The surface roughness average R_a and root-mean-square RMS are two important parameters used to determine the heights of peak and valley in roughness profile of the film in addition to the waviness. The relationship between surface roughness and wave is represented in figure 15. The roughness width refers to the distance parallel to the nominal surface between successive peaks or ridges which constitute the major pattern of the roughness. The waviness height refers to the peak to valley distance. The lay indicates the direction of the major surface pattern. Theoretically, the roughness average (R_a) is defined by:

$$R_a = \frac{1}{L} \int_0^L |Y(x)| dx \dots\dots\dots \text{Equation 5}$$

where R_a describes the arithmetic average deviation from the mean line, L and y describe the sampling length and the ordinate of the profile curve respectively [Mik-1999]. The RMS roughness R_q is defined as:

$$R_q = \left[\frac{1}{L} \int_0^L Z_R(x)^2 dx \right]^{1/2} \approx \left[\frac{1}{N} \sum_{i=1}^N Z_{R_i}^2 \right]^{1/2} \dots\dots\dots \text{Equation 6}$$

Naturally an identical formulation is valid for the waviness. One should mention that the quality of the measurement with such a mechanical profilometry depends consequentially on the sharpness of the stylus and its hardness.

In this work the surface roughness of the films, R_a , was measured by using the Dektak 6M stylus profiler at a minimum range of 2620kÅ.

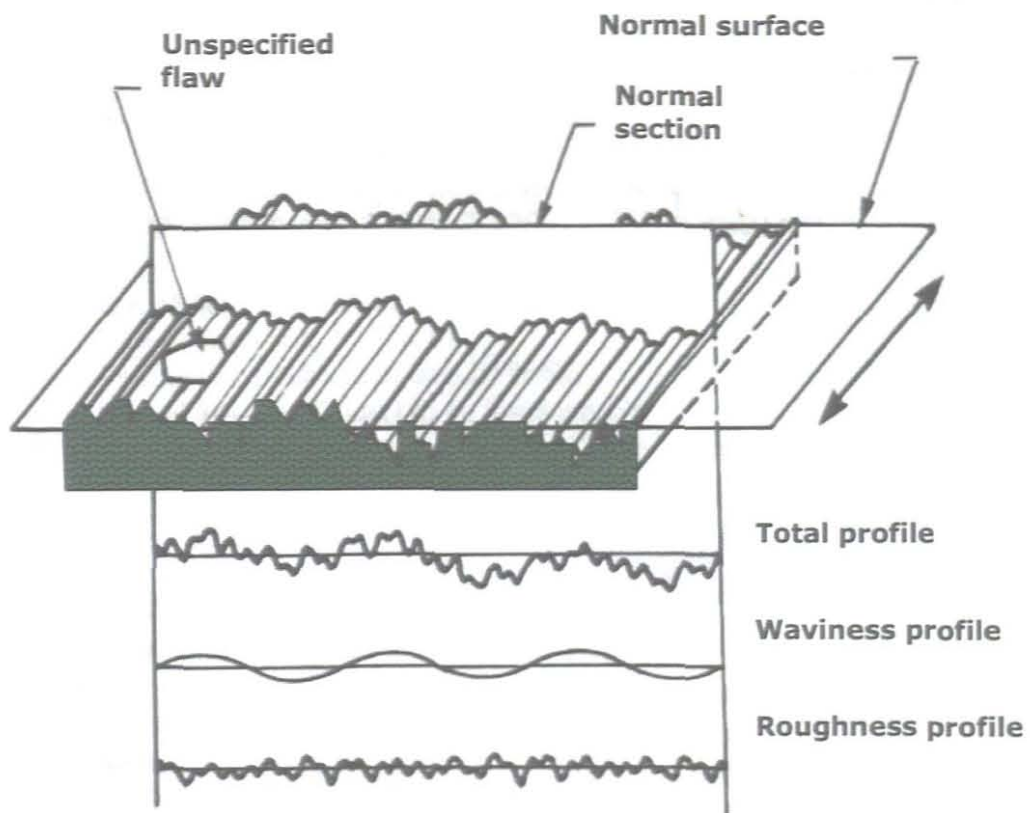


Figure 15: Schematic illustration of surface roughness and surface waviness which is accessible by mechanical dektak profilometry.

4.2. Chemical analysis

4.2.1. Rutherford backscattering Spectrometry

The Rutherford backscattering Spectrometry denoted as RBS is a technique of choice allowing detecting heavy elements contaminants and films thickness as well as elemental depth profiling on our DLC nano-structures in addition to interfacial diffusion with the substrate if any. As illustrated by Figure 16, it consists of bombarding the sample by energetic He⁺ ion beam and collects the backscattered ones. The net loss in energy of these later species is related to the nature and the depth position as well as their concentrations of the scattering atoms in the sample.

RBS is a non-destructive standard technique used to determine the nature of the elements in appropriate sample together with their stoichiometry and depth distribution [Bar-1997, Kar-2002]. The analysis of RBS depends on the energy, angle and particle mass region in which the scattering is expected to take place due to coulomb potential [Art-2001]. There are major important aspects of RBS: (a) Kinematics of the elastic collision and (b) Elastic scattering cross sections.

Kinematics of elastic back scattering is also defined as the kinematic factor K which is given by the energy of the scattered ion divided by initial ion energy as:

$$K = \frac{E_1}{E_0} \dots\dots\dots \text{Equation 7}$$

The kinematic factor K comes after the conservation of the momentum and energy. By knowing the values of K the energy the

elastic scattered ions can be obtain and separated from the inelastically scattered ions.

The energy of the scattering ion is useful for as it will give birth to several energy peaks situated at different energy channels. The energy of center mass frame is determined from the ion energy obtained from the laboratory coordinates and is given by $E_{cm} = E_{lab} (1/m_1+1/m_2)$, m_1 and m_2 represent the masses of the incident ion and target. The relationship between backscattering angle θ in the laboratory and the center of mass frame is given by:

$$\theta_{cm} = \arcsin\left(\frac{m_{ion}}{m_{target}} \sin \theta\right) + \theta \dots\dots\dots \text{Equation 8}$$

where cm is the center mass, m_{ion} mass of the ion in back scattering, and m_{target} is mass of the target. The Rutherford cross section is given by the expression bellow, in the laboratory frame of reference:

$$\frac{d\sigma}{d\Omega} = \left(\frac{Z_1 Z_2 e^2}{16\pi\epsilon_0 E}\right)^2 \frac{4}{\sin^4 \theta} \frac{\left[\sqrt{1 - \left(\frac{m_1}{m_2}\right)^2 \sin^2 \theta} + \cos \theta \right]^2}{\sqrt{1 - \left(\frac{m_1}{m_2}\right)^2 \sin^2 \theta}} \dots\dots\dots \text{Equation 9}$$

where Z_1 and Z_2 are atomic numbers and m_1 and m_2 are the masses of probing ion and scattering center within the target, respectively, E is the incident laboratory energy of the ion and θ is the laboratory scattering angle.

The experimental measurements of RBS presented within this research report were performed using He⁺ ion beam with energy of 2MeV. Two detectors were used: Detector1 «-100V» was fixed at an angle of 165° relatively to the He+ beam direction and detector 2 with tilt angle of -10° and a gain of 300x0.52. The simulation software RUMP was used to determine the chemical composition as well as the thickness of the DLC nano-structures.

RBS

Rutherford Backscattering Spectrometry

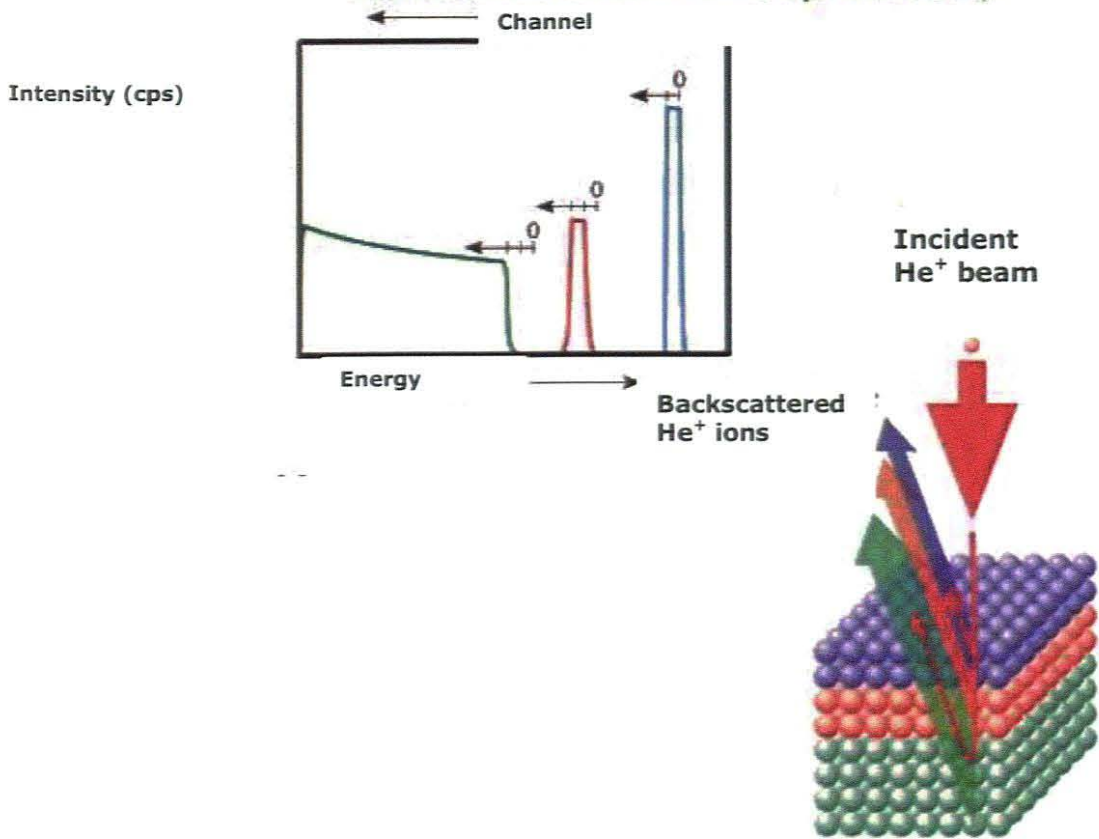


Figure 16: Schematic illustration of He⁺ backscattering in RBS geometry [www.physik.uni-kiel.de/.../methods/rbs.jpg].

4.2.2. Elastic Recoil Detection Analysis

Elastic recoil detector analysis «ERDA» is a complementary ion beam analysis to RBS as it allows the detection of very light elements in particular hydrogen. In this analytic technique heavier ion collides with the lighter target atoms and later they recoils again [Art-2001, Tim-2002]. As for the RBS, there are two major concepts in ERDA each one is responsible for an analytical capability: (i) Ion energy loss and (ii) Scattering kinematics and scattering cross section. As in the case of RBS, the scattering between an energetic ion with the sample's light elements is considered as a classical two body collision.

In this present study the ERDA was performed using beam type He⁺, beam energy 3MeV, using two detectors, detector 1 (-100V/165o/Tilt=-75o, Gain (300x0.346) RBS, detector 2 (+50V/30o/Tilt=-75°, Gain (1Kx0.634).

4.2.3. X-ray Photoelectron Spectroscopy

X-ray Photoelectron Spectroscopy «XPS» is a non destructive surface technique used to determine the composition of the film as well as identifying the atomic environment and hence the bond nature and its electronic valence [Fil-2003]. It is used to distinguish the chemical shift related to the nature of the chemical bonding. In general XPS detect photoelectrons with the kinetic energy in the range of 100-1500eV [Asa-1987, Nam-2005]. It is mostly a surface technique, as the escape depth of the photo-electrons ranges from 2 to 5 nm. The detection limit of this technique is approximately 0,1at%. As illustrated in figure 20, XPS consists of irradiating the

sample's surface with energetic X-rays so to excite inner core electrons and induce emission of specific photoelectrons. The intrinsic energy of these photoelectrons is related to the electronic configuration of the elements located at the sample's surface and their neighbours. More precisely, the emitted photoelectrons from different elements have a kinetic energy E_k given as [Sea-2003]:

$$E_k = h\nu - E_b - \phi \dots \dots \dots \text{Equation 10}$$

where E_k and $h\nu$ are the kinetic energy of the ejected electrons and the energy of the X-ray radiation respectively. E_b is the binding energy of the core electrons while Φ is the work function. XPS has been a technique of choice in the early studies of DLC nano-structures and thick coatings [Yib-2003, Vas-2004]. By knowing the energy of the X-ray photons and measuring the kinetic energy of the extracted electrons, one can determine the binding energy of the extracted electrons. This technique is unique and can be used to identify the elements from which the electrons were extracted. The advantage of this technique is that it can detect most of all the elements except Hydrogen and Helium.

In the present work, a Quantum 2000 scanning XPS unit was used to determine the chemical bonding of C_{1s} and other elements using a monochromatic Al X-rays source with an emitting power of about 17.9W. The beam focus was approximately of the order of $100.0 \mu m$ with an impinging angle of 45° while its energy was kept at around 29.35eV.

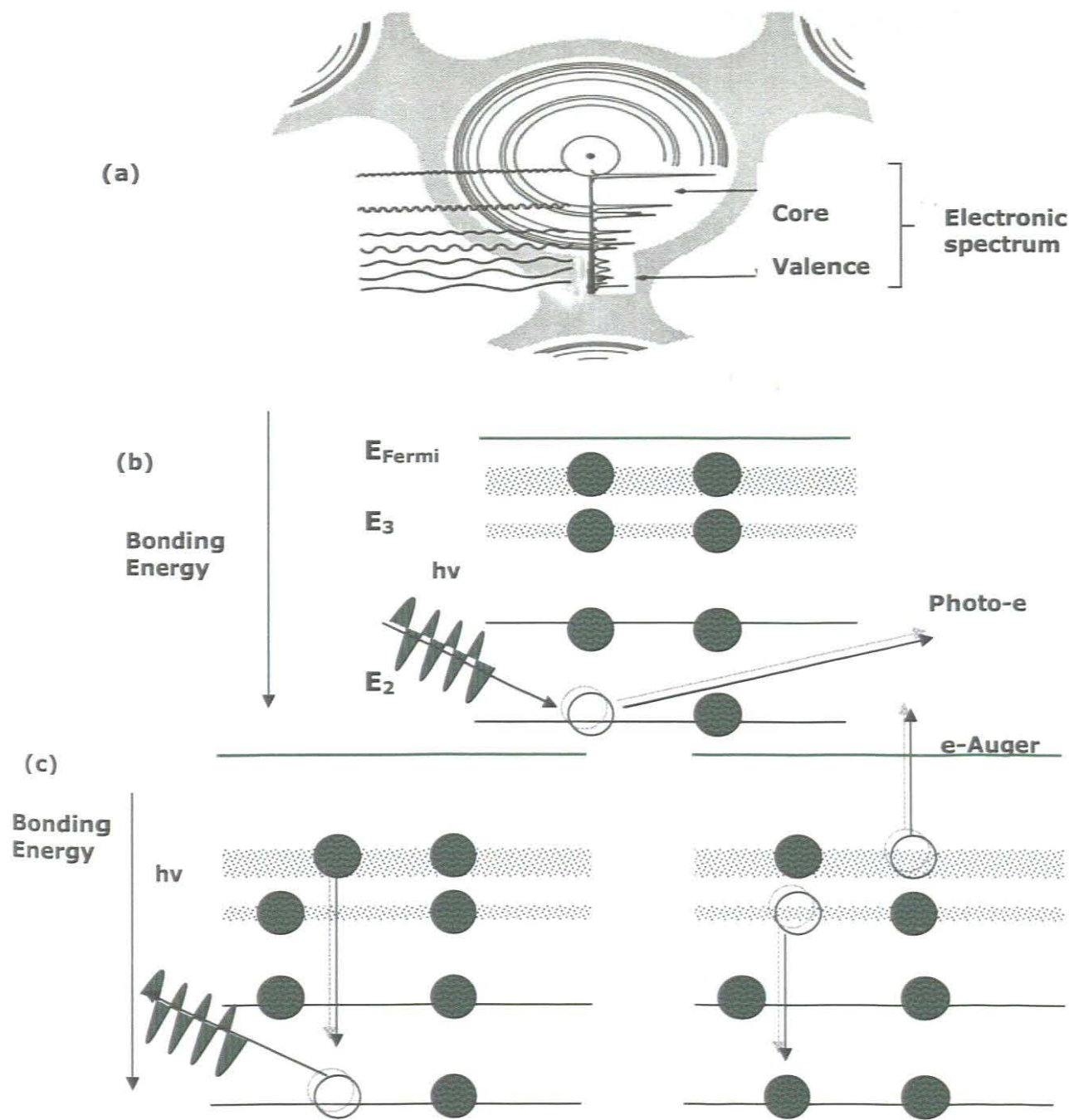


Figure 17: Schematic illustration of (a) core electronic configuration and XPS phenomena at the (b) excitation and (c) after relaxation.

4.3. VIBRATIONAL & OPTICAL PROPERTIES

4.3.1. Raman Spectroscopy

Raman spectroscopy is a complementary technique to infrared absorption. It gives information about vibrational and rotational transitions in molecules but does it in a different way. A laser source irradiates the sample with frequency ν_s and the scattered light is collected and analyzed for spectral difference relative to the laser value. Most of scattering proceeds elastically i.e. Rayleigh scattering type, without any change of the incident photon energy, ν_s , but few photons scatter inelastically, due to their interactions with the vibrating molecule and molecules vibrating with a frequency ν_i , as well rotation, ν_r , in the molecule. Since at room temperature most of vibrational states are not excited, the inelastic scattering is also mostly observed with lowering the photon energy, $\nu_s - n \nu_i$ or to the "red" of laser energy. It is called Stokes scattering (Figure 21). The anti-Stokes scattering with $\nu_s + n \nu_i$, is of a lower intensity which can be increased by raising the temperature because these transitions originate from vibrationally excited states [Han-2000, Jac-2005]. In rotational Raman intensity of Stokes and anti-Stokes transitions are very similar at room temperature. Classically, at the microscopic level, the electric field of the exciting laser source is applied to a molecule or atoms in a crystal inducing its distortion (Figure 18). The distorted molecule acquires a contribution to its dipole moment, even if it is nonpolar initially:

$$\Delta \mu = \alpha E \dots \dots \dots \text{Equation 11}$$

The term α is the polarizability of the molecule which is a measure of the polarizability/distortion induced on the electron cloud around the molecule. The induced dipole emits or scatters light at the optical

frequency of the incident light wave. The polarizability is typically different when the field is applied (a) parallel, \parallel , or (b) perpendicular, \perp , to the molecular axis or in different directions relative to the molecule. The molecule in such a case has an anisotropic polarizability. For small values of E , i.e. in the linear regime, the polarizability is the same for the field oriented in the opposite directions along the same axis, $\Delta\mu(-E) = -\Delta\mu(E)$. Thus the distortion induced in a molecule by the incident electric field returns to its initial value after a rotation of only 180° . This is the origin of $\Delta J = 0, \pm 2$ selection rule (rotational quantum number) in rotational Raman spectroscopy. Vibrational Raman scattering occurs because a molecular vibration can change the polarizability. The change is described by the polarizability derivative, $\delta\alpha/\delta Q$, where Q is the normal coordinate of the vibration. The selection rules for Raman-active vibrations are thus linked to molecular symmetry and identify vibrations that change molecule's polarizability, i.e.: $(\delta\alpha/\delta Q)^2 > 0$

The Raman selection rule is analogous to the more familiar selection rule for an infrared-active vibration, which states that there must be a net change in permanent dipole moment during the vibration. From group theory it is direct to show that if a molecule has a centre of symmetry, vibrations which are Raman-active will be silent in the infrared, and vice versa. The scattering intensity is proportional to the square of the induced dipole moment, that is to the square of the polarizability derivative, $(\delta\alpha/\delta Q)^2$. Therefore, if a vibration does not greatly change the molecular polarizability, then the polarizability derivative will be near zero, and the intensity of the Raman band will be low. The vibrations of a highly polar species, such as the O-H bond, are usually weak. An external electric field can not induce a large change in the dipole moment and stretching or bending the bond does not change this. Typical strong Raman scatterers are species with distributed electron clouds, such as carbon-carbon

double bonds. The π -electron cloud of the double bond is easily distorted in an external electric field. Bending or stretching the bond changes the distribution of electron density substantially, and causes a large change in induced dipole moment. This makes Raman spectroscopy an ideal tool to study DLC films.

The corresponding selection rules for Raman spectroscopy are as follows: (i) the normal modes of vibration of molecules are Raman active if they are accompanied by a changing polarizability. For CO_2 - symmetric stretch is Raman active, asymmetric stretch and bending are not, (ii) if the molecule has a center of symmetry, and then no modes can be both infrared and Raman active. A mode can be inactive in both. The rule applies to CO_2 but to neither H_2O nor CH_4 . The advantages of Raman spectroscopy are: (i) it has different selection rules than do direct electronic, vibrational and rotational spectroscopies, so it provides complementary information, (ii) Raman spectroscopy uses visible light and (iii) water molecule which could contaminate investigate samples, is a relatively weak Raman scatterer, but a strong infrared absorber. Because of this Raman spectroscopy is often the technique of choice for the study of molecules in aqueous environments, for example biological samples.

Raman spectrometry presented within this research work was conducted at the department of Chemistry of the Tshwane University of Technology-Pretoria. The measurements were conducted at room temperature using Nd:YAG laser of the excitation wavelength emitting at the fundamental (1064nm), with the Germanium detector cooled at liquid nitrogen at a power of about 200 mW. The spectral resolution was about (4cm^{-1}), with a zero filling factor of 2. To ensure better statistical measurements, 512 averaged scans at 180 degree back scattering geometry on each sample have been conducted.

4.3.2. Infrared spectroscopy

In a molecule, the atoms are not held rigidly apart. Instead they can move, as if they are attached by a spring of equilibrium separation R_e . This bond can either bend or stretch. If the bond is subjected to infrared radiation of a specific frequency in the range of $300 - 4000\text{cm}^{-1}$, it will absorb the energy, and the bond will move from the lowest vibrational state, to the next highest. In a simple diatomic molecule, there is only one direction of vibrating, stretching. This means there is only one band of infra red absorption. Weaker bonds require less energy, as if the bonds are springs of different strengths. If there are more atoms, there will be more bonds, and therefore more modes of vibrations.

This will produce a more complicated spectrum. For a linear molecule with "n" atoms, there are $3n-5$ vibrational modes, if it is nonlinear, it will have $3n-6$ modes. For example, water (H_2O), has 3 molecules, and is nonlinear: therefore it has $(3 \times 3) - 6 = 3$ modes of vibrations.

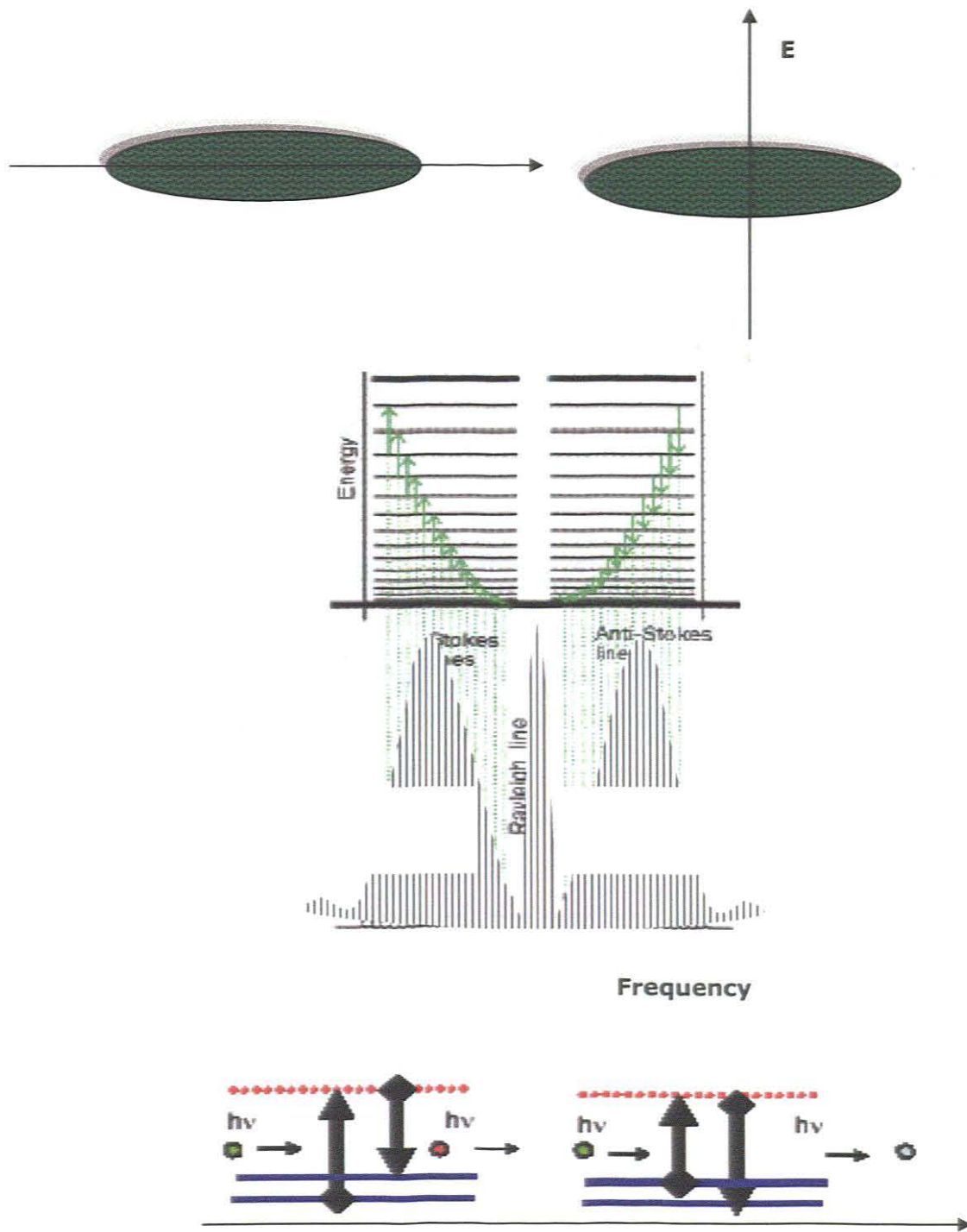


Figure 18: Schematic illustration of Raman scattering.

There is one important restriction; the molecule will only absorb radiation if the vibration is accompanied by a change in the dipole moment of the molecule. A dipole occurs when there is a difference of charge across a bond. If the two oppositely charged molecules get closer or further apart as the bond bends or stretches, the moment will change. To calculate the frequency of light absorbed requires Hookes law:

$$\nu_{osc} = \frac{1}{2\pi} \sqrt{k \frac{m_1+m_2}{m_1m_2}} \dots\dots\dots\text{Equation 12}$$

k = force constant indicating the strength of the bond, m₁ and m₂ are the masses of the two atoms. By looking at this equation, we can see that if there is a high value of k, i.e. the bond is strong, it absorbs a higher frequency of light. So, a C=C double bond would absorb a higher frequency of light than a C-C single bond. Also, the larger the two masses, the lower the frequency of light absorbed. In order to derive the relationship between vibrational energy and molecular structure, it is necessary to solve the Schroedinger equation for vibrational-rotational interactions. This later is remarkably simple and very similar to the relationship obtained from considering the classical model of balls and springs.

$$E = \frac{h}{2\pi} \sqrt{\frac{k}{\mu}} \left(n + \frac{1}{2} \right) \dots\dots\dots\text{Equation 13}$$

Excluding the (n + 1/2) term, the two equations are equivalent. The Schroedinger equation is a differential equation which vanishes unless certain terms in it has very discrete values. For n, the allowed

values are 0,1,2,... The energy of vibration associated with a molecule in its lowest energy of vibration, $n = 0$ is then:

$$E = \frac{h}{4\pi} \sqrt{\frac{k}{\mu}} \dots\dots\dots \text{Equation 14}$$

This relation allows estimating about what would happen to the vibrational energy of a molecule at absolute zero. According to quantum theory the molecule would continue to vibrate. From the relationship $E = hv$, one can evaluate the vibrational frequency as:

$$\nu = \frac{1}{2\pi} \sqrt{\frac{k}{\mu}} \dots\dots\dots \text{Equation 15}$$

This equation states that the vibrational frequency of a given bond in a molecule depends only on the stiffness of the chemical bond and the masses that are attached to that bond. Similarly, once the structure of a molecule is defined, the force constants and reduced mass are also defined by the structure. This also defines the vibrational frequencies and energy of absorption. Stated in a slightly different manner, a molecule will not absorb vibrational energy in a continuous fashion but will do so only in discrete steps as determined by the parameters in the previous equations. Upon absorption of vibration energy, this vibrational quantum number can change by +1 unit. At room temperature, most molecules are in the $n = 0$ state.

In the case of carbon-hydrogen stretching frequencies and since k and m_H are the only two variables, if we assume that all C-H stretching force constants are similar in magnitude, one would expect the stretching frequencies of all C-H bonds to be similar. This expectation is based on the fact that the mass of a carbon atom and whatever else is attached to the carbon is much larger than the mass of hydrogen. The reduced mass for vibration of a hydrogen atom would be approximately the mass of the hydrogen atom which is independent of structure. All C-H stretching frequencies are observed at approximately 3000 cm^{-1} , exactly as expected. Fortunately, force constants do vary some with structure in a fairly predictable manner and therefore it is possible to differentiate between different types of C-H bonds.

This is due to the fact that the C-H bond strength increases as the s character of the C-H bond increases. Some typical values are given below in for various hybridization states of carbon. Bond strength and bond stiffness measures different properties. Bond strength measures the depth of the potential energy well associated with a C-H. Bond stiffness is a measure of how much energy it takes to compress or stretch a bond. While these are different properties, the stiffer bond is usually associated with a deeper potential energy surface. As indicated by the following IR absorptions, that increasing the bond strength also increases the C-H bond stretching frequency.

Type of C-H bond kcal/mol cm-1	Bond Strength	IR Frequency	
sp ³ hybridized C-H	CH ₃ CH ₂ CH ₂ -H	99	<3000
sp ² hybridized C-H	CH ₂ =CH-H	108	>3000
sp hybridized C-H	HCC-H	128	3300

Table 5: IR absorptions of C-H bond

Hydrogen on sp³ carbon atoms all absorb between 2850 and 3000 cm⁻¹ while hydrogen's attached to sp² and sp¹ carbon sites absorb at 3000-3250 cm⁻¹ and 3300 cm⁻¹ respectively. The following table shows the different stretching modes of C-H and the oscillator strength of various types C-H modes together with their wave numbers [Rob-2002].

Experimentally, a thermonicolet Nexus 470 was used to determine the chemical bonding of present in DLC film. This spectrometer has ability to collect spectra in the mid-IR, far-IR and near-IR. The process variables for this experiment are spectral data, sampling area, and depth of penetration. The air background spectrum and glass or Si substrates spectrum was also obtain with the intension of comparing with the one for the deposited DLC films. 100 scans were taken to each an every sample to ensure there's no noise which can lead to the convolution to DLC films. J. Robertson [Rob-2002] states that the oscillator strength of some of C-H stretching modes is not constant.

Wavenumbers (cm ⁻¹)	Configuration	Olefinic or aromatic	symmetric or antisymmetric
3300	sp ¹		
3085	sp ²	Olefinic	A
3035	sp ²	Aromatic	
2990-3000	sp ²	Olefinic	S
2975	sp ²	Olefinic	S
2955	sp ³		A
2920	sp ³		A
2920	sp ³		
2885	sp ³		S
2855	sp ³		S
1480	sp ³		A
1450	sp ³		A
1430	sp ³	Aromatic	
1415	sp ²	Olefinic	
1398	sp ³		S
1375	sp ³		S
2180	sp ¹		
1640	sp ²	Olefinic	
1580	sp ²	Aromatic	
1515	sp ² /sp ³		
1300-1270	sp ² /sp ³		

Table 6: Variation of IR vibrational frequencies in hydrogenated amorphous carbon (a-C:H), Data from J. Robertson [Rob-2002].

4.3.3. UV-VIS-NIR optical Spectroscopy

In this method the light source shined through a sample and then the absorption is measured. The measured absorption caused by the electronic transitions in the sample. Normally the optical band gap (E_g) of thin films is assumed by considering the linear part of the absorption spectrum. The optical band gap of the material can be found using Tauc type plot at the point whereby the line intersects with the energy [Sea-2003]. In previous studies the optical properties of material were obtained constructing the transmission spectrum. Therefore Figure 19 show how determine the $T_M(\lambda)$ and $T_m(\lambda)$, both represent the maxima transmittance and minima transmittance as a function of wavelength (λ). T_s in Figure 19 represent the transmittance value measured from a spectrophotometer [Tan-2006]. The two transmittances are found by allocating all the extreme points of the interference fringes in the transmission spectrum. Therefore the refractive index of the thin films found by considering the two envelopes, $T_M(\lambda)$ and $T_m(\lambda)$ together with the refractive index of the substrates. Figure 20 shows the best fitting of determining the refractive index of the thin film as function of wavelength (λ).

Theoretically the thickness of the films is calculated from interference equation of wave by considering either two or more points of maxima and minima as shown by the following equation:

$$d = \frac{\lambda_1 \lambda_2}{2(\lambda_1 n_2 - \lambda_2 n_1)} \dots \dots \dots \text{Equation 16}$$

Where d is the thickness found from the maxima and minima of two points. In this work a CARRY 1E UV-Visible spectrophotometer was used to determine the optical properties of DLC film.

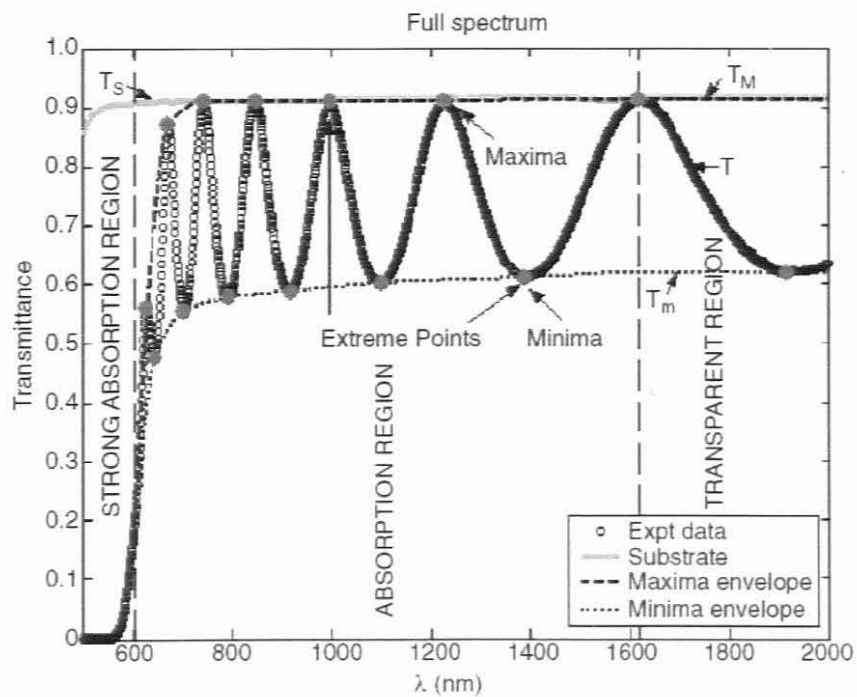


Figure 19: The construction of envelopes in the transmission spectrum [Tan-2006].

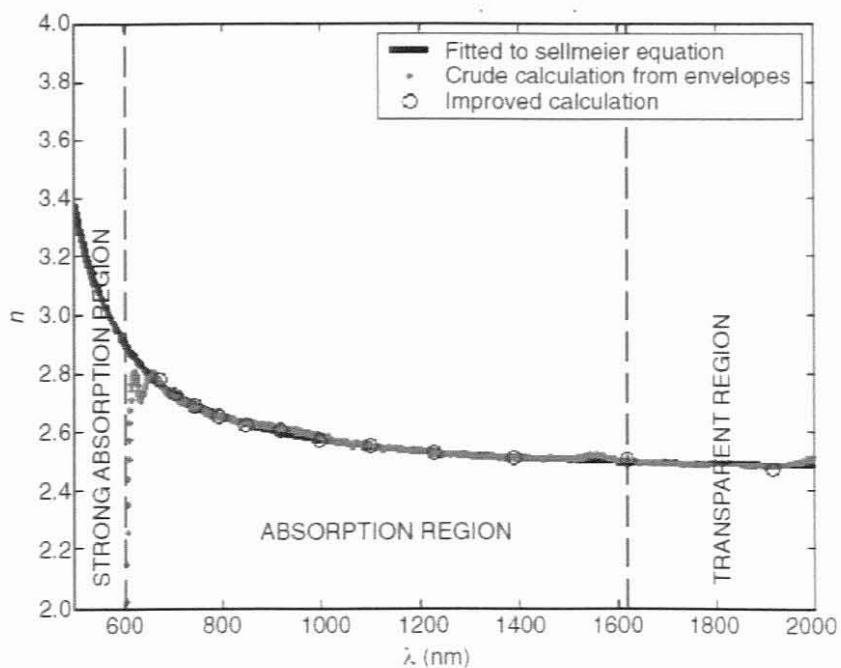


Figure 20: Determination of the refractive index from the transmission spectrum maxima and minima [Tan-2006].

CHAPTER 5

5.1. EXPERIMENTS & DISCUSSIONS

5.1.1. Synthesis by double pulsed gas-feeding/pulsed laser deposition

As per mentioned in chapter 2-section 2, due to its energetic & shock wave intrinsic properties as well as the possible implantation assisted effect, pulsed laser ablation was chosen to synthesize the nano-structured DLC films onto room temperature substrates. In addition, this work presents the first DLC synthesis by dual double pulsed gas feeding/pulsed laser deposition. As it is illustrated in Figure 24, it consists of ablating pure carbon target and injection of pulsed flow of methane or hydrogen onto the growth zone at the vicinity of the substrate's surface. This configuration is expected to thermalize less the ablated carbon species within the plume and permits a local interaction between the gas pulses and the carbon species. In addition, the pressure in the chamber can be kept constant at a certain extent which indeed minimizes the thermalization effect. The pressure of the chamber was maintained by a turbo pump to ensure identical initial conditions throughout the full process of deposition. Methane gas was introduced by valve onto the surface of the substrate in order to produce the desired films. Before each deposition, the chamber is evacuated at a base pressure of $\approx 10^{-5}$ mbar using three pumps.

Excimer laser source was preferred so to minimize thermal effects if any by radiative phenomenon during the extension of the plume. In

this work, the XeCl laser source emitting at $\lambda \approx 308$ nm with pulse duration of about 25 ns was used. The used experimental setup consisting of a Lambda Physik EMG 203 MSc unit at the University of Stellenbosch is shown in Figure 25. The incident laser radiation was focused onto a focal lens and deviated by beam splitter at an angle of 45° through a quartz window chamber, onto the highly pure graphite target

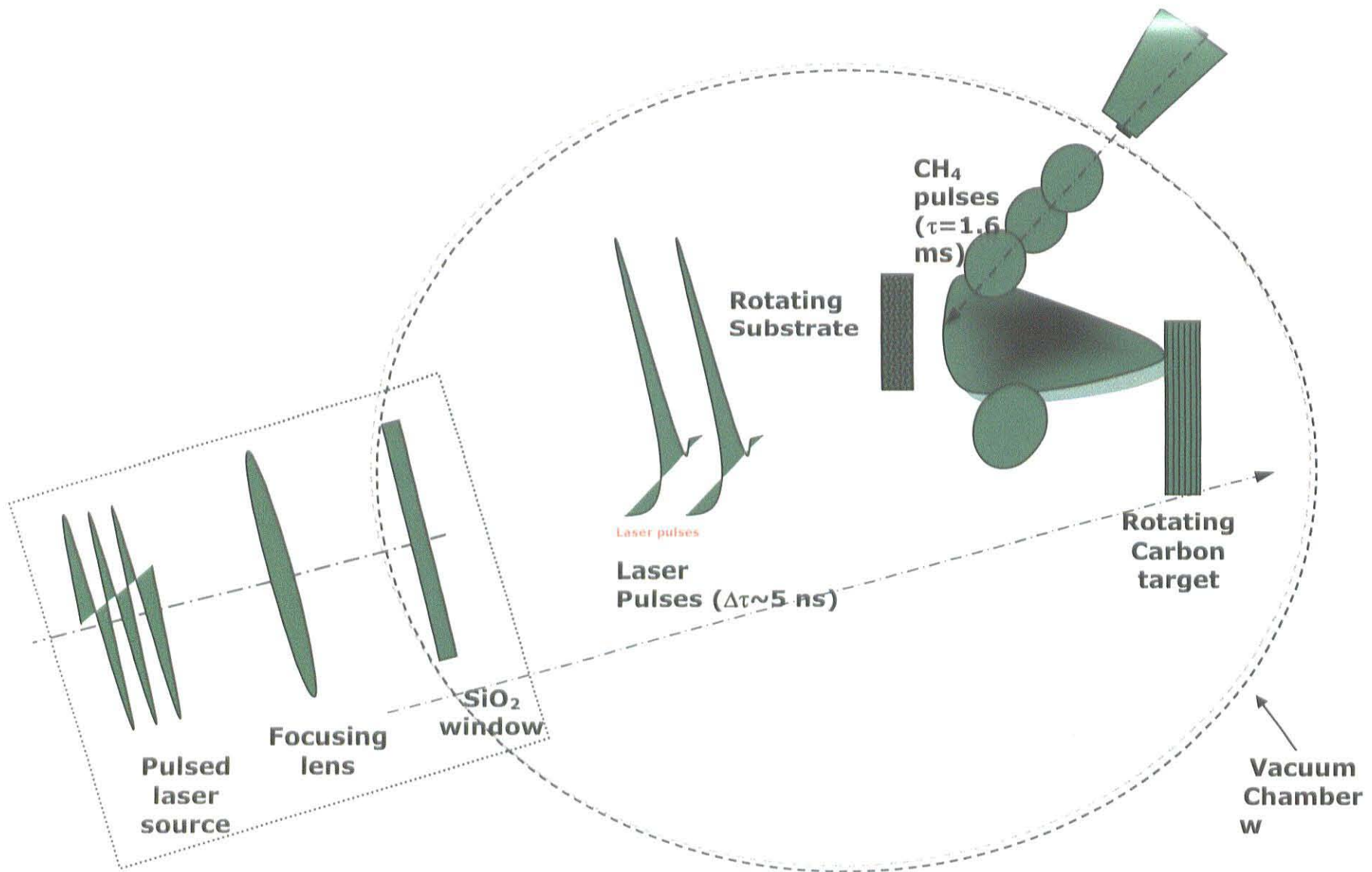


Figure 21: Schematic diagram of Pulsed laser deposition.

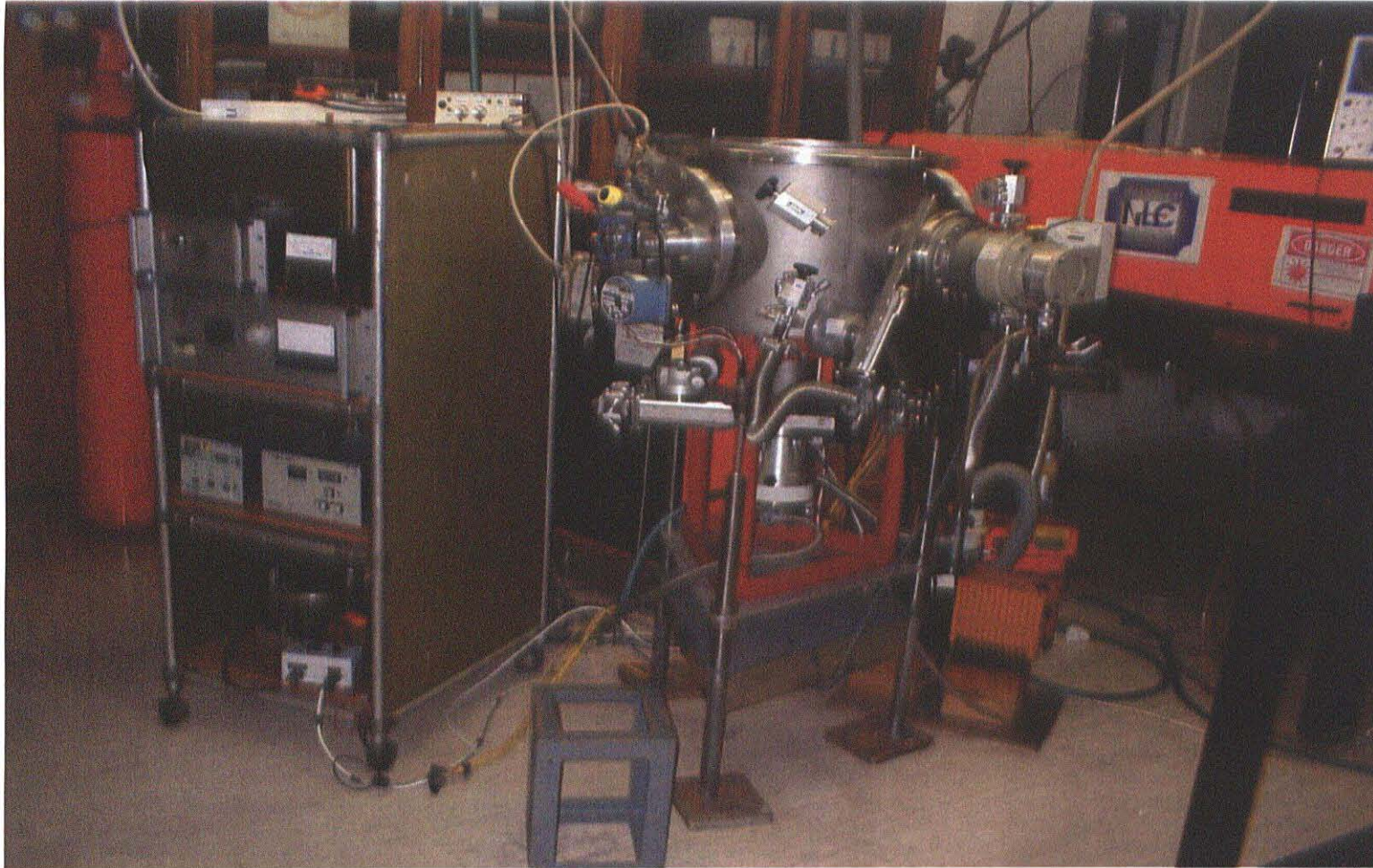


Figure 22: Photograph of the dual beam pulsed gas feeding/pulsed laser deposition setup.

at an incidence angle of approximately 45° . During the deposition, the target holder was kept rotating in order to prevent hole formation on the surface of the target. Likewise the substrates were rotated to ensure a better chemical homogeneity and the thickness uniformity of the deposits.

Two types of substrates were used in this work, silicon (100) and float glass. The sizes of these substrates were of the order of 1 cm^2 in dimension. Before any deposition, the substrates were cleaned within the standard method. They were ultrasonically cleaned in organic solvent, acetone and dried thereafter at a temperature of about 130°C to remove adsorbed water surface layers.

Concerning the pulsed laser deposition, the same set up was used along the series of experiments carried out. Single and multi substrate holders were used during the deposition of DLC films. The multi substrate holder was able to accommodate up to six samples. A rotating 20cm in diameter of high purity graphite target was used «Carbon Lorraine». The XeCl excimer laser was operated in general at a frequency of about 10Hz with pulses' width of 5ns . Naturally, various parameters including repetition rate, fluence/energy, initial pressure, working pressure, deposition time, and voltage were considered depending on the working conditions. The distance between the substrate and target surface was varied as well within the range of $5\text{--}8\text{cm}$ by moving the substrate assembly in and out. The spot size on the laser beam onto the target's surface was controlled by adjusting the focal length of the external lens. The base pressure in the chamber was fixed at approximately $\approx 10^{-5}\text{ mbar}$ in order to obtain good quality films. Once the chamber pumped to a base pressure of $\approx 10^{-5}\text{ mbar}$, methane gas (99.9%) was introduced at

the value of $\approx 10^{-2} \text{ mbar}$ generally under a form of pulses with a flow period of 1ms.

The deposition parameters of the DLC films by PLD described in this work are summarized in table 5. The deposition took place at room temperature ($25^{\circ}C$). The flow of methane gas onto the surface of the substrate was introduced by valve at the pulsed rate of 1.6 ns. The deposition condition was optimized to ensure the deposited films are uniform, whereas some of the parameters were changed for comparison purposes. It has been noticed that high amount of pressure in the chamber increases the scattering centers. Table 5 summarizes all the deposition conditions with their corresponding DLC nano-structures. Various deposition conditions were considered so to correlate the physical properties to the ablation and growth mechanism effects. Indeed, in the case of using PLD, the kinetic energy of the particles is fundamentally determined by the ablation mechanism and the composition of the target and its optical absorption cross section in addition to the plume dynamic.

Numerous techniques of characterization were used to deduce not only the optimal conditions but also to understand the physical phenomena related to this novel dual beam deposition. Table 6 reports the characterization methodologies used in this research work.

Figure 23 shows two sample series. While the first series are those obtained by standard pulsed laser deposition, the second class is those obtained by the current room temperature dual pulsed laser-pulsed gas flow deposition. In both cases, the obtained films are generally yellow to brownish in color, characteristic of DLC films. The films deposited by standard PLD present a low adhesion properties to the substrates (both glass or Si) while the series

prepared by the double pulsed gas flow-laser beam exhibit a very good adhesion on glass substrates as well as on silicon. This major difference could be caused by a difference in terms of thermalization process of the ablated species reaching the substrate.

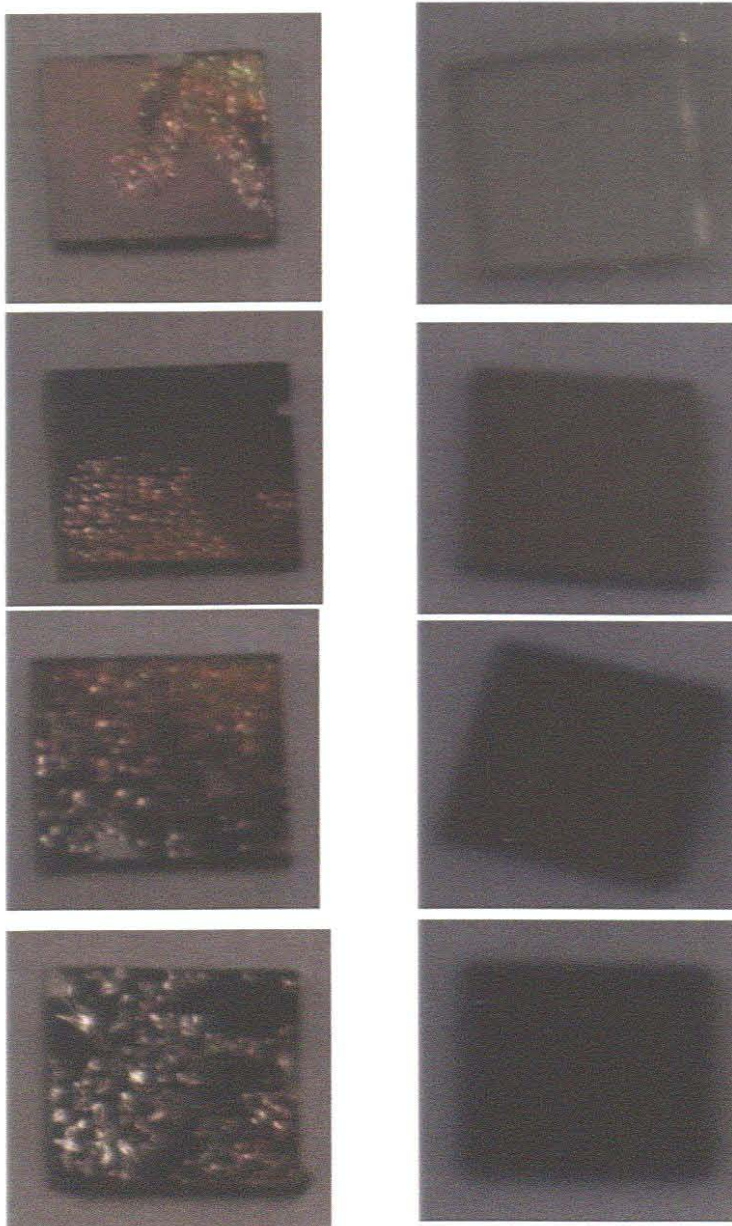


Figure 23: Typical DLC films synthesized by (a) standard PLD and (b) dual pulsed gas flow beam-pulsed laser beam.

Due to the local methane feeding of the dual PLD version, the carbon and hydrogenated carbon clusters have more kinetic energy once they are on the substrate. Hence, their relaxation onto the substrate is larger minimizing the stress at the DLC film/substrate interface.

5.1.2. Characterization techniques and characterization conditions

The surface morphology investigations were performed at room temperature by scanning electron microscopy «SEM», Zygo optical interferometry and mechanical surface mapping. The elemental-chemical analysis were carried out by Rutherford backscattering «RBS», Elastic recoil detection analysis «ERDA» as well as X-ray photoelectron spectroscopy «XPS». This later was, in addition used to investigate and quantify the C-C sp^2 - sp^3 type bonds. The accurate sp^2/sp^3 and C-C as well as C-H bonding nature were studied by Raman and infrared spectroscopies at room temperature.

The SEM investigations were carried out on the unit located at the University of Cape Town. The operating voltage was about 10kV with a probe current of about(20pA). The Zygo interferometry measurement were performed using non destructive interferometer Zygo «MLIS-6891» at the National Laser Centre-Pretoria while the surface mechanical topography studies were conducted at the University of Western Cape. A dektak 6M stylus profiler at a minimum range of 2620kÅ^m was used.

The presented measurements of RBS were performed using He⁺ ion beam with an energy of 2MeV on the Van de Graaf unit of iThemba LABS. Two detectors were used: Detector 1 «-100V» was fixed at an angle of 165° relatively to the He⁺ beam direction and detector 2 with a tilt angle of -10° & a gain of 300x0.52. The simulation software RUMP was used to deduce the chemical composition as well as the thickness of the DLC nano-structures.

Sample Code	substrate	Frequency (Hz)	Fluence (mJ)	Initial Pressure (mbar)	Working Pressure (mbar)	Time (min)	Voltage (V)
A	Glass	16	82	5x10 ⁻⁵	2x10 ⁻²	120	24
B	Glass	16	290	5x10 ⁻⁵	6x10 ⁻²	30-60	24
C:1	Glass	16	345	5x10 ⁻⁵	1x10 ⁻¹	25	18
C:2	Glass	16	382	5x10 ⁻⁵	1x10 ⁻¹	25	19
C:3	Glass	16	327	5x10 ⁻⁵	1x10 ⁻¹	25	20
C:4	Glass	16	309	5x10 ⁻⁵	1x10 ⁻¹	25	21
C:5	Glass	16	345	5x10 ⁻⁵	1x10 ⁻¹	25	22
C:6	Glass	16	327	5x10 ⁻⁵	1x10 ⁻¹	25	23
D:1	Glass	16	309	6x10 ⁻⁵	9x10 ⁻²	25	18
D:2	Glass	16	309	6x10 ⁻⁵	9x10 ⁻²	25	19
D:3	Glass	16	327	6x10 ⁻⁵	9x10 ⁻²	25	20
D:4	Glass	16	345	6x10 ⁻⁵	9x10 ⁻²	25	21
D:5	Glass	16	345	6x10 ⁻⁵	9x10 ⁻²	25	22
D:6	Glass	16	363	6x10 ⁻⁵	9x10 ⁻²	25	23
E:1	Silicon(100)	16	136	5x10 ⁻⁵	2x10 ⁻²	20	24
E:2	Silicon(100)	16	136	5x10 ⁻⁵	2x10 ⁻²	30	24
E:3	Silicon(100)	16	136	5x10 ⁻⁵	2x10 ⁻²	40	24
E:4	Silicon(100)	16	136	5x10 ⁻⁵	2x10 ⁻²	50333	24
E:5	Silicon(100)	16	136	5x10 ⁻⁵	2x10 ⁻²	60	24
G	Silicon(100)	10	163	5x10 ⁻⁵	2x10 ⁻²	120	24
H	glass	3	181	5x10 ⁻⁵	2x10 ⁻²	20	23

Table 7: Deposition parameters of the deposited DLC films at different conditions.

Likewise, the ERDA were performed at the van de Graaf unit of iThemba LABS using a 3 MeV He⁺ beam, with a 2 detector configuration, detector 1 (-100V/165o/Tilt=-75o, Gain (300x0.346) RBS and detector 2 (+50V/30o/Tilt=-75°, Gain (1Kx0.634).

THE XPS investigations were achieved at the metrology laboratory of the CSIR on a Quantum 2000 scanning XPS unit for the chemical bonding of C_{1s} and other elements using a monochromatic Al X-rays source with an emitting power of about 17.9W. The beam focus was approximately of the order of 100.0 μm with an impinging angle of 45° while its energy was kept at around 29.35eV. The Raman spectrometry investigations were conducted at the department of Chemistry of the University of South Africa-Pretoria. The measurements were performed at room temperature using a Nd:YAG laser of an excitation wavelength emitting at the fundamental (1064 nm), associated to a Germanium detector cooled at liquid nitrogen. The spectral resolution was about 4 cm^{-1} , with a zero filling factor of 2. To ensure a better statistical measurement, 512 averaged scans at 180 degree backscattering geometry on each sample have been conducted. The UV-VIS-NIR optical transmission measurements were carried out on a standard Carry 1E UV-Visible spectrophotometer in the spectral range of 200nm - 1000nm.

Sample	SEM	FT-IR	XPS	Raman	UV-VIS	RBS	ERDA	Stylus	Zygo
A		•	•						
B	•	•	•						
C	•	•			•			•	
D	•	•						•	•
E		•	•	•		•	•	•	•
F	•	•		•		•	•		
G		•	•					•	
H	•								

Table 8: Used morphological, elemental-chemical and optical characterization techniques.

5.1.3. Surface morphology properties

As mentioned previously, the surface morphology was first investigated by mechanical topography for the different DLC nanostructures deposited on silicon and glass substrates. As well established, this mechanical surface topography allows an appreciable estimation of the surface roughness even if generally this later is convoluted with the diameter of the stylus' pin diameter. Table 9 reports the corresponding average value of the surface roughness of the different samples. The study is more focused towards the effect of the deposition time on the average surface roughness «Ra». The major reason is that «Ra» could shed light on the nature of the growth mechanism of the deposited DLC. As shown by Figure 24 reporting the evolution of Ra versus the DLC films' thickness, the average roughness during the initial stages of

deposition seems to decrease monotonously with the DLC films' deposition time i.e. with a thickness from 28 nm to 17 nm.

Sample Code	Frequency (Hz)	Time (min)	Ra (nm)	Pressure (mbar)	Thickness (nm)	Voltage (kV)
E:1	16	20	28.5	0.02	-	24
E:2	16	30	17.5	0.02	-	24
E:3	16	40	24.7	0.02	-	24
E:4	16	50	21.7	0.02	-	24
E:5	16	60	17.3	0.02	-	24
F:1	5.7	60	17	0.01	-	24
G	10	120	21.4	0.02	353	24
C:3	16	25	-	0.01	450	20
C:4	16	25	-	0.01	420	21
C:6	16	25	-	0.01	740	23

Table 9: The average surface roughness versus the DLC film's thickness determined by mechanical surface profiling

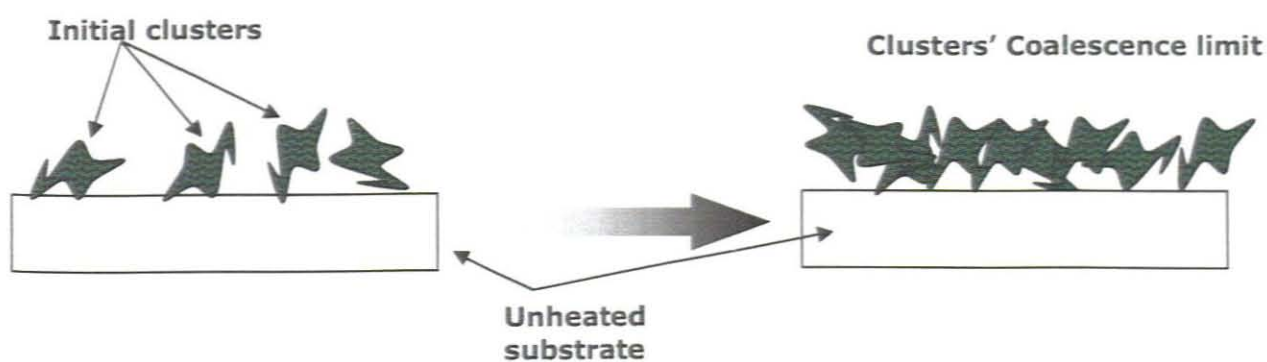
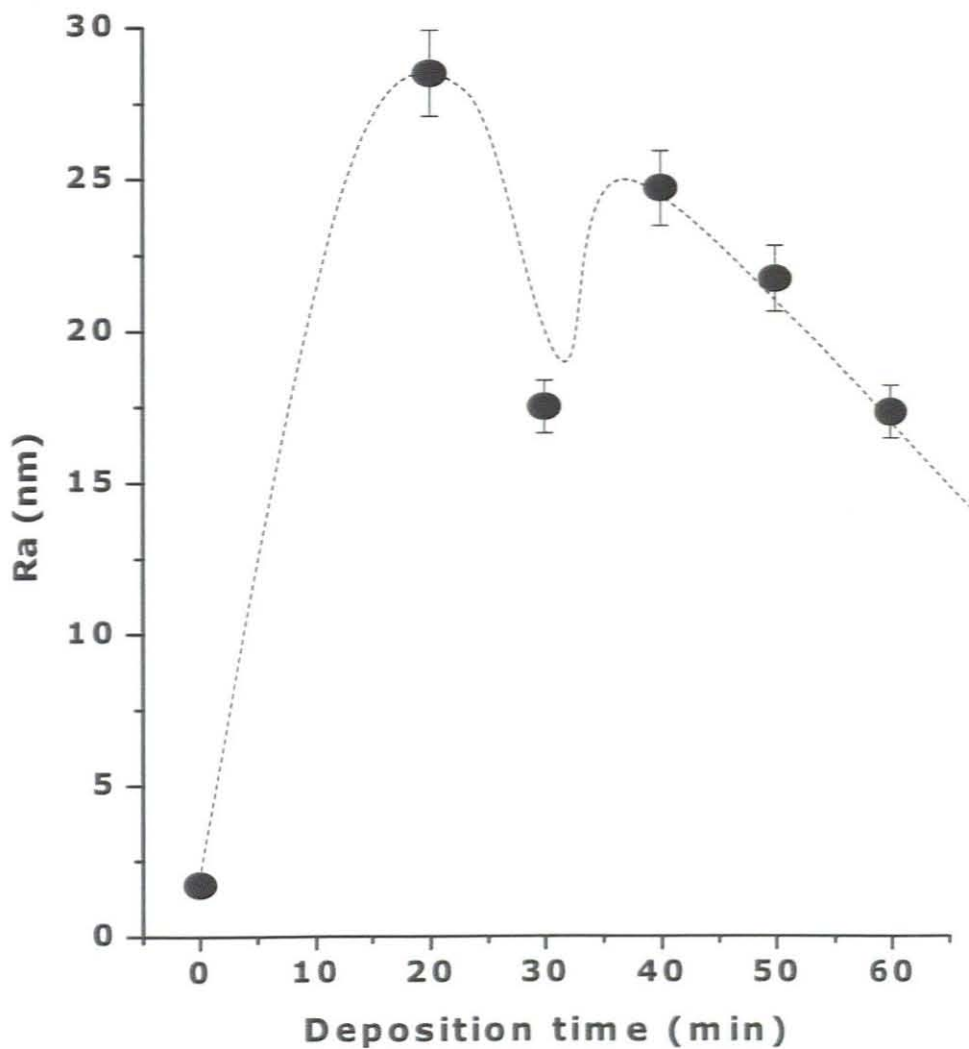


Figure 24: Evolution of the average surface roughness versus the DLC films' thickness and illustration of the coalescence phenomena of the C, C-H clusters onto the substrate's surface.

Excluding the large roughness at the initial growth stage of about 28 nm, such an evolution of «Ra» could be considered as a reflection of the growth rate and the growth shape of the DLC nano-structures as in the case of standard thin films' growth mechanism. As illustrated in Figure 27, initially, the clusters of carbon and hydrogenated carbon are considered to grow independently within the relatively cold surface of the substrate being it a silicon or glass substrate. Thereafter they start to coalesce following a threshold value of the DLC's thickness which seems to be located within the deposition time in the range of 20-30 minutes. From this coalescence value, the DLC nano-structures start to smoothen forming quasi-leveled smooth surface. Hence, the coalescence limit could be considered as located at the vicinity of 30 min in terms of deposition time/thickness correspondence.

While the mechanical surface topography is limited to a reduced surface area, the optical topography via the Zygo interferometry scanning allows the possibility to scan larger surface areas of about 2 mm² in average. Therefore, it is suitable to have a more accurate topography in terms of long range deposited clusters and coverage rate. Table 8 reports the room temperature Zygo interferometry measurements while Figure 25 shows a typical Zygo interferogram. More accurately, Figure 26 shows the evolution of the peak to valley roughness versus the deposition time and hence versus the DLC films' thickness. Excluding the last point corresponding to the thickest sample of the series «60 min» which exhibits a very large value of about 2300nm, the peak to valley roughness decreases with the films' thickness with an average slope of 6.9 nm/min. This drop in the peak to valley roughness indicates that the films have a tendency to smoothen following the coalescence stage as schematically illustrated in Figure 24. This could be considered as a sign of amorphization state. This sustained by the X-ray diffraction

investigations carried out on all DLC samples deposited without heating. The samples showed no Bragg peaks but rather very large non intense peak centered around 25 deg; a signature of an amorphous state indeed. The very large value of the order of 2250 nm for the thickest DLC film could only be due to a droplet, an intrinsic property of the pulsed laser ablation.

As both the average surface roughness and the peak to valley roughness have a tendency to decrease subsequent to the percolation threshold and coalescence limit, one could extrapolate that the ablated species tend to form nano-scaled clusters with a very local atomic ordering if any. These clusters could consist of pure Carbon or Hydrogenated Carbon as the deposition conditions remain unchanged during the deposition time. These surface observations concur with the DLC literature [Pan-2003].



Figure 25: Typical interferogram obtained by Zygo interferometry (a) and in false color (b) as well as the deduced surface roughness profile (c).

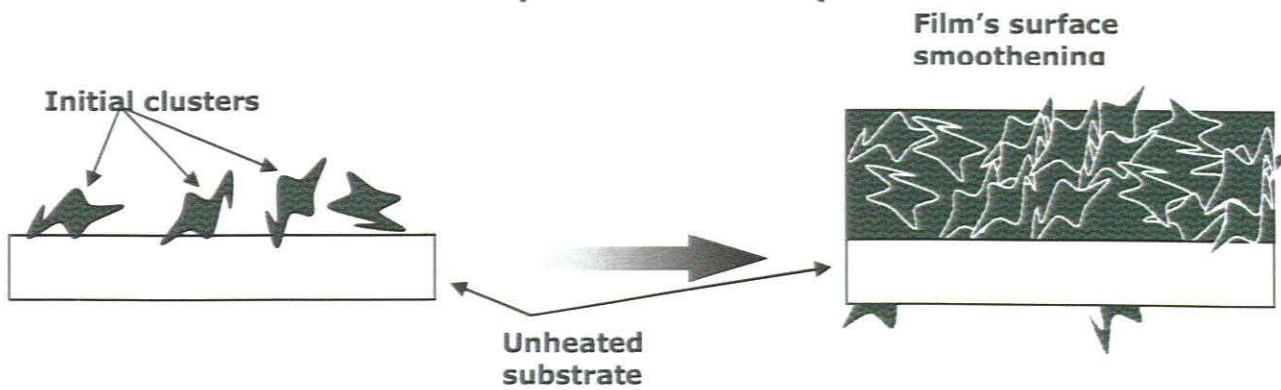
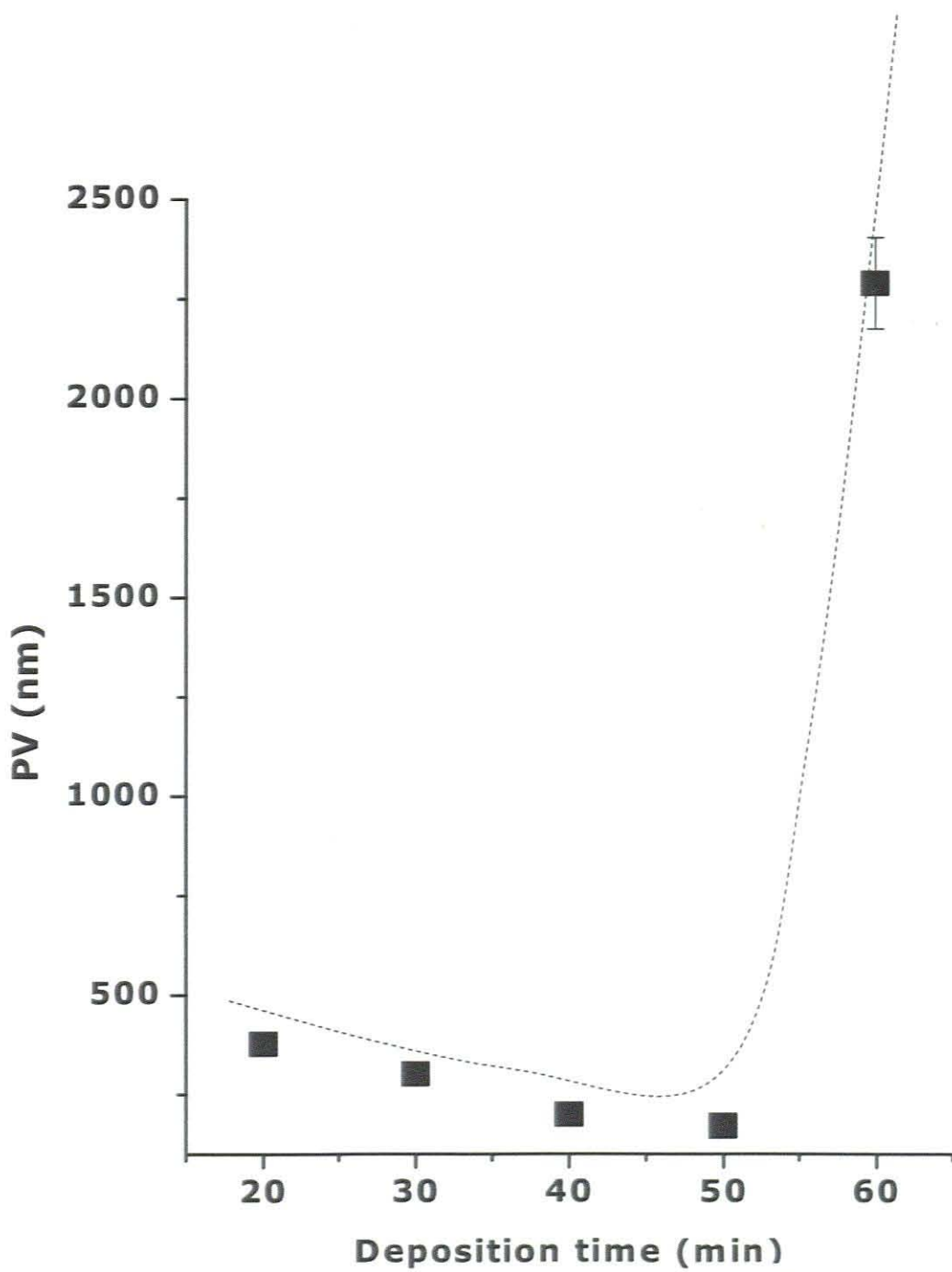


Figure 26: Evolution of the peak to valley roughness versus the DLC films' thickness and illustration of the surface smoothening on large scale.

The surface topography by both mechanical and optical interferometry has been complemented by scanning electron microscopy. Figure 30.a reports a typical high resolution SEM of a DLC film deposited on unheated substrate with a thickness above the threshold value. The films are continuous, smooth and do not exhibit grain morphology sustaining the amorphous state of the films. This concurs with the previous surface morphology results as well as with the literature; usual DLC films produced by PLD method at low temperature are amorphous but could contain few macroscopic particulates caused by the shock wave phenomenon [Fug-2004].

Figure 27b shows the SEM image of sample H, a DLC film deposited on a heated glass at about 500°C. Such heated samples peel repeatedly regardless of the used Si or glass substrates. This peeling of the heated films is the result of high residual compressive stress, itself caused by the large difference in thermal conductivities or/and crystalline mismatch between the carbon and hydrogenated carbon clusters and the substrate. The synthesized DLC films are usually affected by the compressive stress especially the thickness [Rob-2002]. The high compressive stresses have been studied by many researchers, producing DLC films which are deposited on various substrates like glass, silicon, stainless steel, etc. The residual internal stress has been found dependent up on the thickness of the films and increases with the thickness in general. It is proved that high internal or residual stresses affect the film when is used for hard coatings by reducing the adhesion strength, microhardness, and wear resistance [Sam-1999, Sum-1998]. The internal stress and adhesion are the two aspects which depend on the stability of the film and substrate [Hid-1999, Yan-2004]. As the result of high internal stress the DLC films become hard and peel off when deposited on steel substrates [Kul-2000]. The DLC films have a significant surface adhesion or wetting tension [Yan-2004]. Robertson reported that the surface energies range between 40-

44mNm^{-1} whereby the low surface energies provide relatively large contact angle [Rob-2002].

(a)



(b)

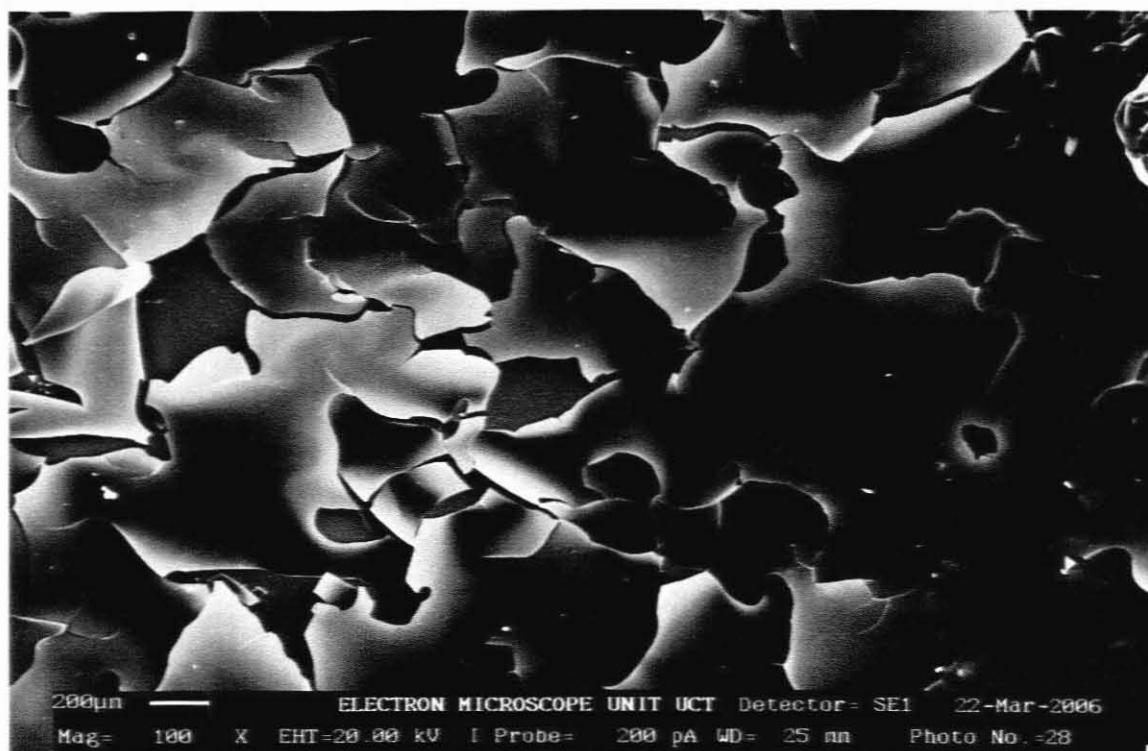
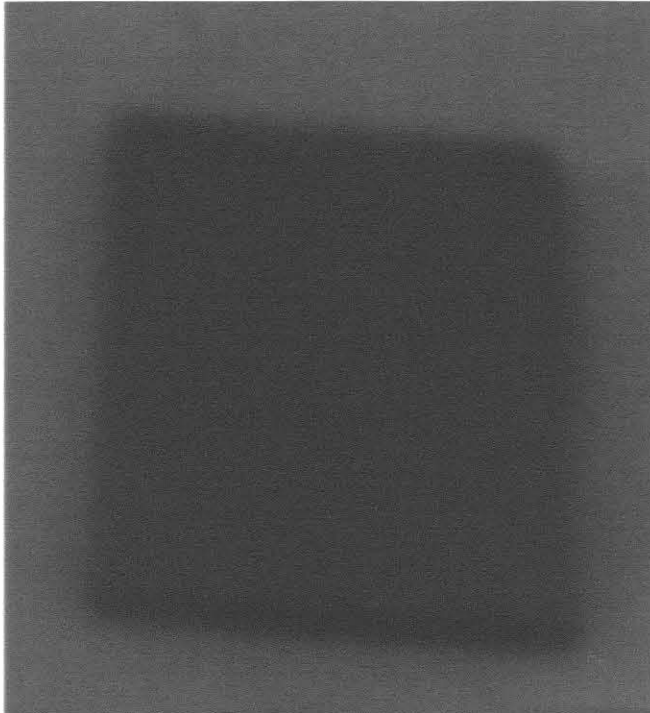


Figure 27: Scanning electron microscopy of DLC films deposited at (a) unheated [sample E3] and (b) heated 500°C [sample H] glass substrates.

As confirmed within numerous studies in the literature, the stresses can be minimized by reducing the amount of hydrogen [Sum-1998] as well as the substrate temperature. Indeed, as shown in Figure 31, low and average hydrogen content samples deposited onto room temperature substrates exhibit continuous and cracks free DLC films of yellow-brown or brown color depending on the film thickness. At low thickness the film show yellow color and becomes yellow-brown to brown at larger thickness. One should mention that the induced residual stress have been found to be minimized by optimizing the laser spectral properties i.e. its wavelength and pulse width value. Indeed, it was found that the particulates growing on the surface of the film can be diminished by using short wavelength UV excimer laser [She-2005]. Relatively to CO₂ and Nd:YAG lasers sources, there is less heating phenomena as the two later sources are emitting in the infrared region: 10.6 mm (CO₂) and 1.06 mm (Nd:YAG)

(a)



(b)

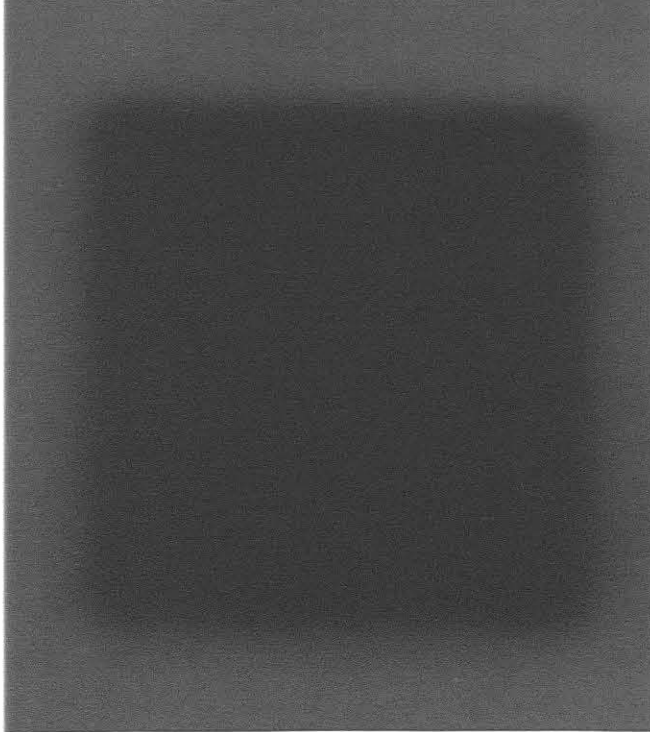


Figure 28: Typical DLC films deposited onto unheated glass substrates with thicknesses of (a) 420 nm [sample C4] and (b) 740 nm [sample C6].

5.1.4. Elemental analysis and hydrogen-Carbon content

In view of quantifying the relative concentration of carbon and hydrogen content and their depth distribution as well as any elemental contamination in particular with oxygen, two techniques were mainly used as mentioned previously: RBS and ERDA. In addition, both techniques allow a direct elemental profiling and could shed light on inter-diffusion phenomena at the interface glass-DLC films and Si-DLC films. For RBS, only samples deposited onto silicon substrates are investigated as the spectra can be easily treated. More accurately, this section provides the RBS and ERDA results of DLC film deposited on silicon substrates at different time and different deposition pressures (Table 1). The DLC films discussed within this RBS section are: Samples series E1 to E5 for which the deposition pressure was fixed to $5 \cdot 10^{-5}$ mbars and those deposited during a fixed deposition time of 25min at the following deposition pressures of: $2 \cdot 10^{-2}$, $6 \cdot 10^{-2}$, $9 \cdot 10^{-2}$, and $1 \cdot 10^{-1}$ mbars. Figure 29 reports the corresponding RBS profiles. As it can be clearly observed, there are no other elements than silicon and carbon specifically no oxygen contamination at least lower than the RBS detection limit. The carbon manifests itself in a form of well localized peak centered at the vicinity of channel 100. As it can be noticed, higher is the pressure, smaller is the carbon peak width i.e. smaller is DLC films' thickness. Approximately, the width at 0.01 mbar is about 4.5 times its value at 1 mbar deposition pressure. This indicates the expected role of the deposition pressure onto the rate of DLC films' deposition. This decrease of the DLC films' thickness versus the deposition pressure P could only be associated to the free mean path of the carbon clusters originating from the plume. The free mean path $\langle L_{\text{clusters}} \rangle$ could be estimated in a first approximation

as $\langle L_{\text{clusters}} \rangle \sim 1/P$. Therefore the free mean path of the carbon clusters and carbon species in general originating from the target via the plume is 4 times larger at 1×10^{-2} mbars than at 4×10^{-2} mbars. Hence the rate of deposition on the substrate if carbon reacting with the hydrogen at the interface of the substrate is 4 times larger at 1×10^{-2} mbars.

Concerning the evolution of the carbon content and its distribution within the DLC films' thickness versus the time of deposition for a fixed deposition pressure, it should be varying in a linear trend. Figure 30 reports the variation of the carbon content versus the deposition time. Figure 30a shows a typical RBS profile with its simulation using RUMP program. Figure 30b indicates that the carbon profile is not constant within the DLC films' thickness but rather variable. It decreases from about 2370 (20 min.) to 460 Carbon atoms/cm². Such a variation could indicate a variation of the reactivity with hydrogen of the carbon clusters at the substrate with the films' thickness and might be an indication therefore of the sp^2/sp^3 ratio evolution. In any case, one should note that the carbon concentration reduction is substantial after 20 min deposition time, a value which concurs with the percolation threshold as indicated in previous Figure 24.

The concentration of hydrogen in the film plays a major role in the nature of bonding and influences the relative sp^3 or sp^2 carbon atoms' population [Pan-2003]. The use of CH₄ in the production itself promotes the formation of sp^3 type carbon bond [Man-1999]. Following the carbon content investigations within the DLC films, hydrogen profiling was performed on the same series of samples by ERDA to find out any correlation between H/C variation and therefore sp^2/sp^3 evolution. Naturally the hydrogen profiling could be determined by different techniques such as nuclear reaction

analysis «NRA», nuclear magnetic resonance «NMR», combustion and infrared spectroscopy. Nuclear techniques such as ERDA and NRA have the advantage to allow the determination of a real density distribution as the RBS for carbon and therefore ERDA & RBS combination would permit the calculation of the desired ratio H/C without measuring the DLC film thickness. In addition, the determination of hydrogen by NMR requires protons

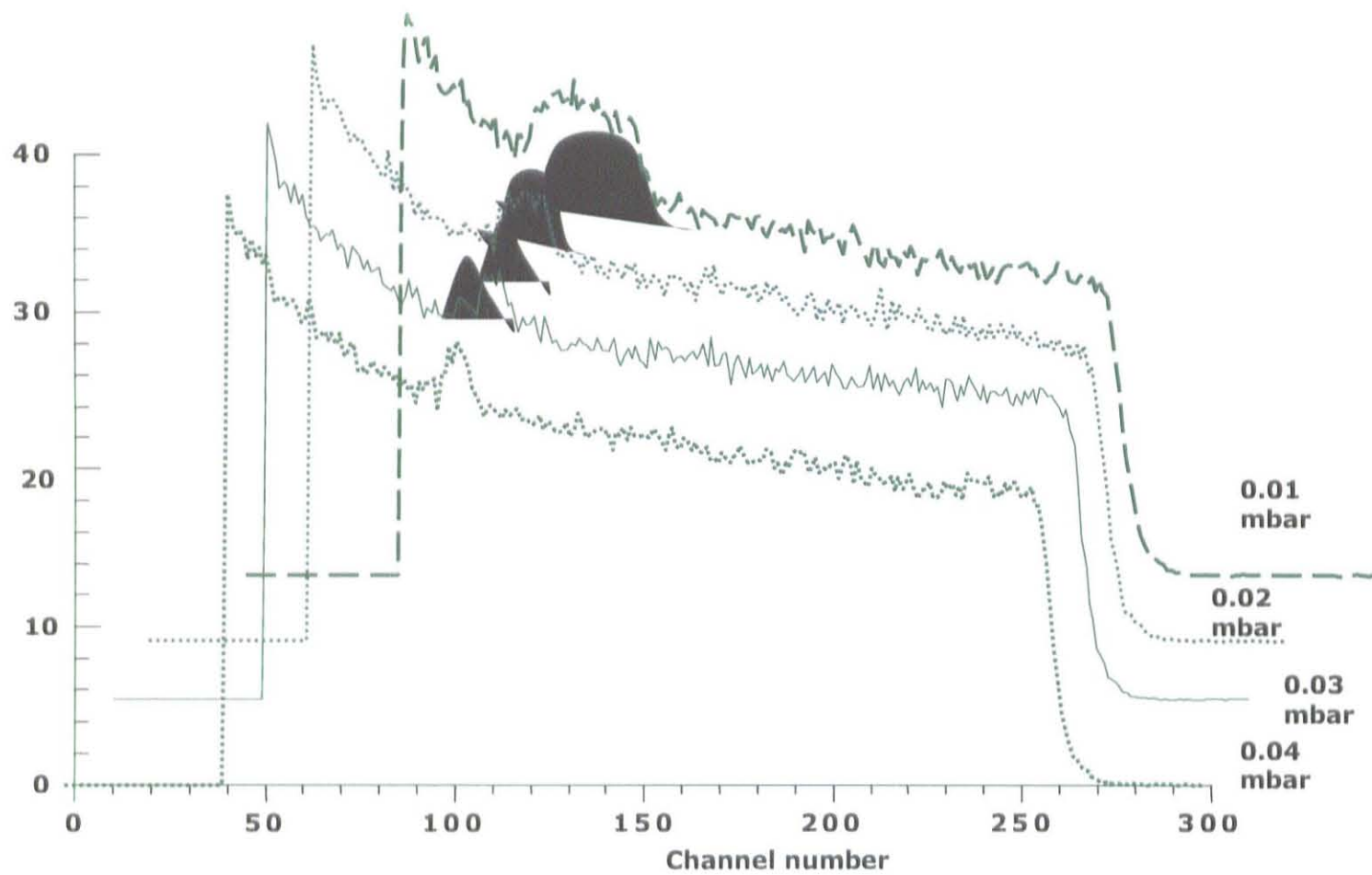


Figure 29: Rutherford Backscattering profiles of DLC films deposited onto Si(100) at different times during a fixed deposition pressure of 1×10^{-2} mbar (Table 1).

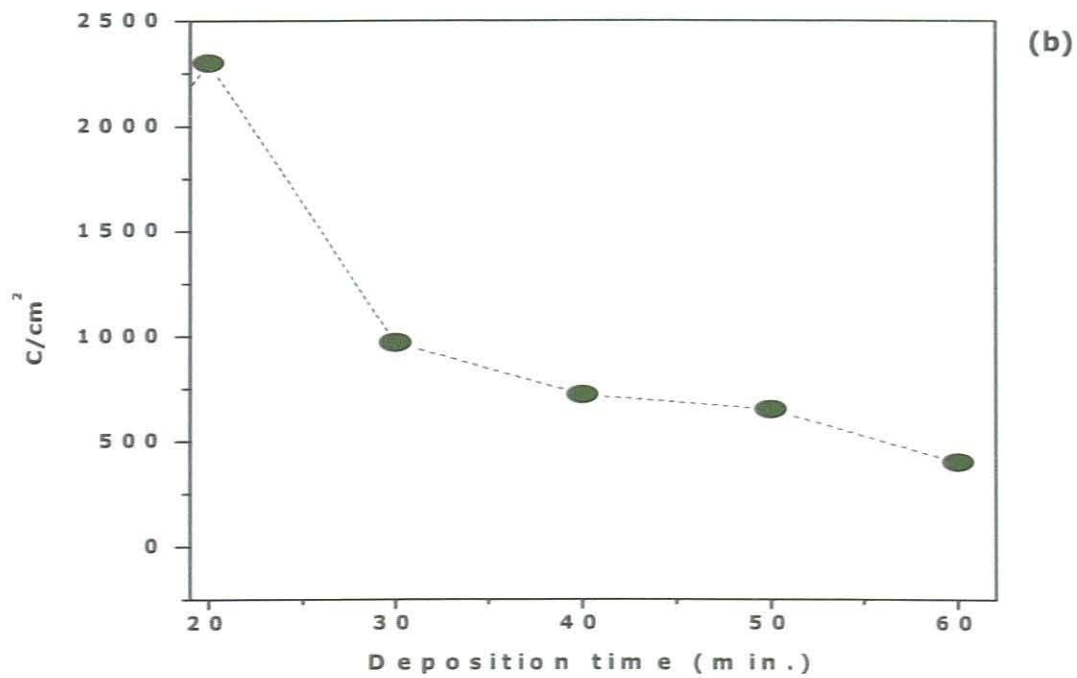
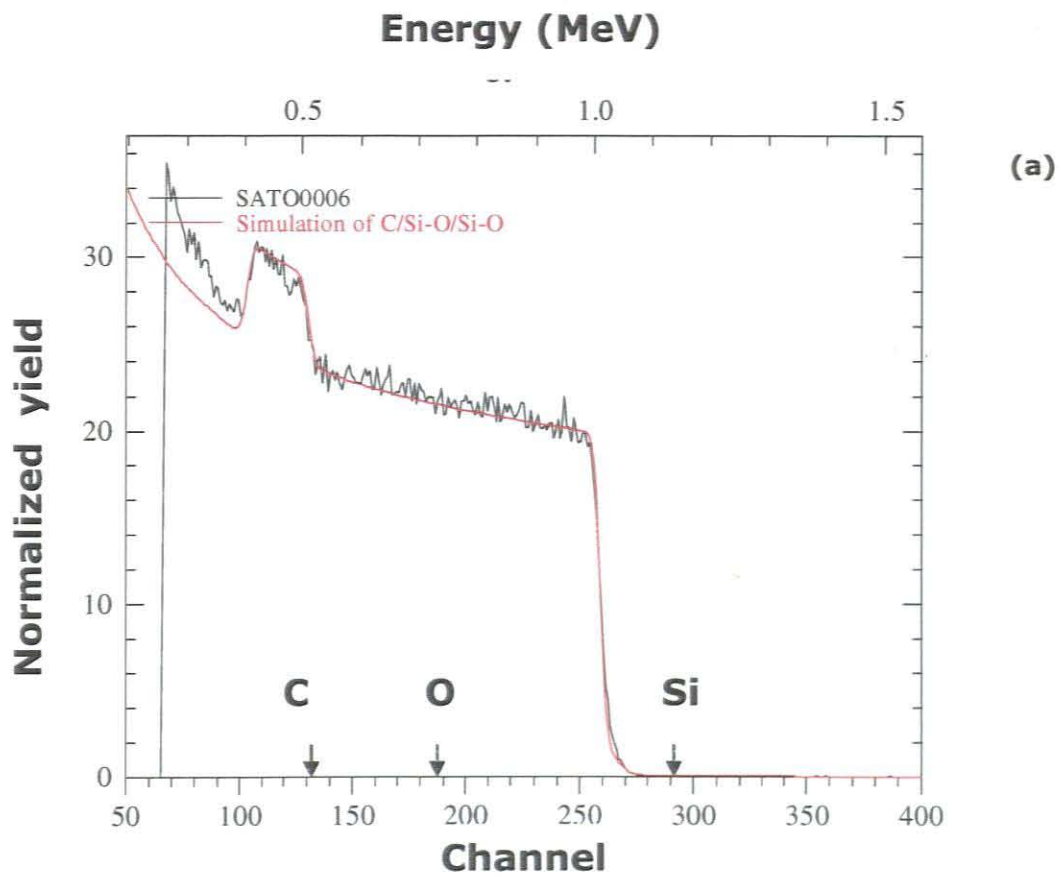


Figure 30: Rutherford Backscattering profiles of DLC films deposited onto Si (100) at different times during a fixed deposition pressure of 1×10^{-2} mbars (Table 1).

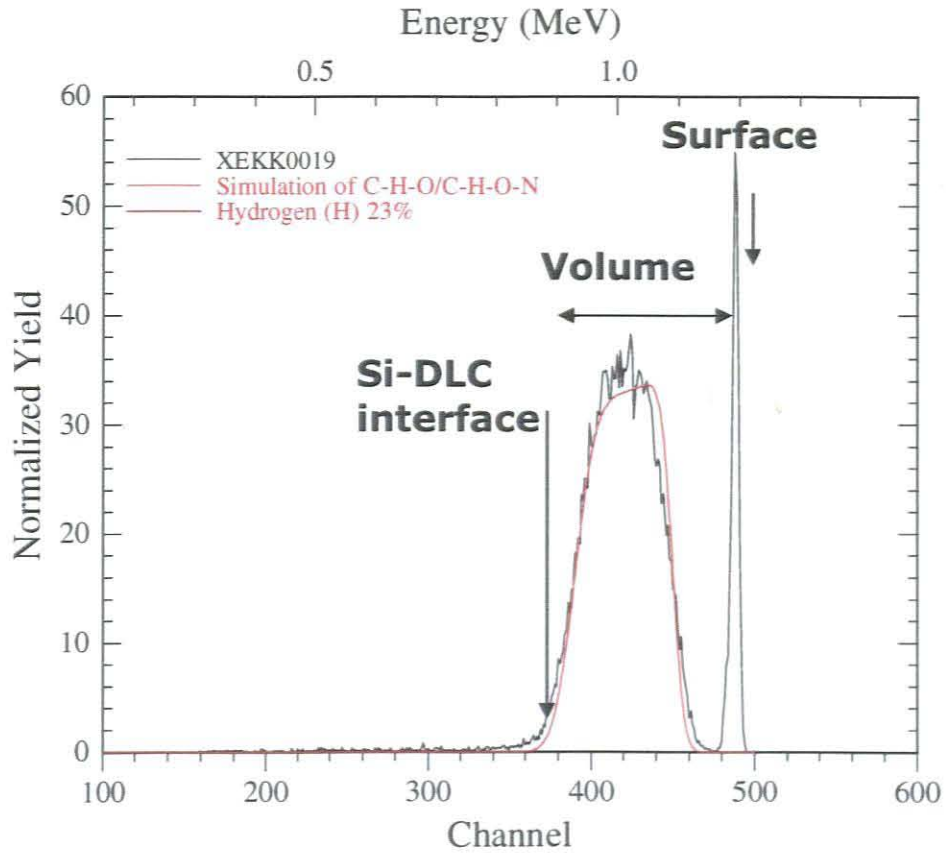


Figure 31: Typical ERDA profile of DLC/Si (100) with its simulation by RUMP program (Table 1).

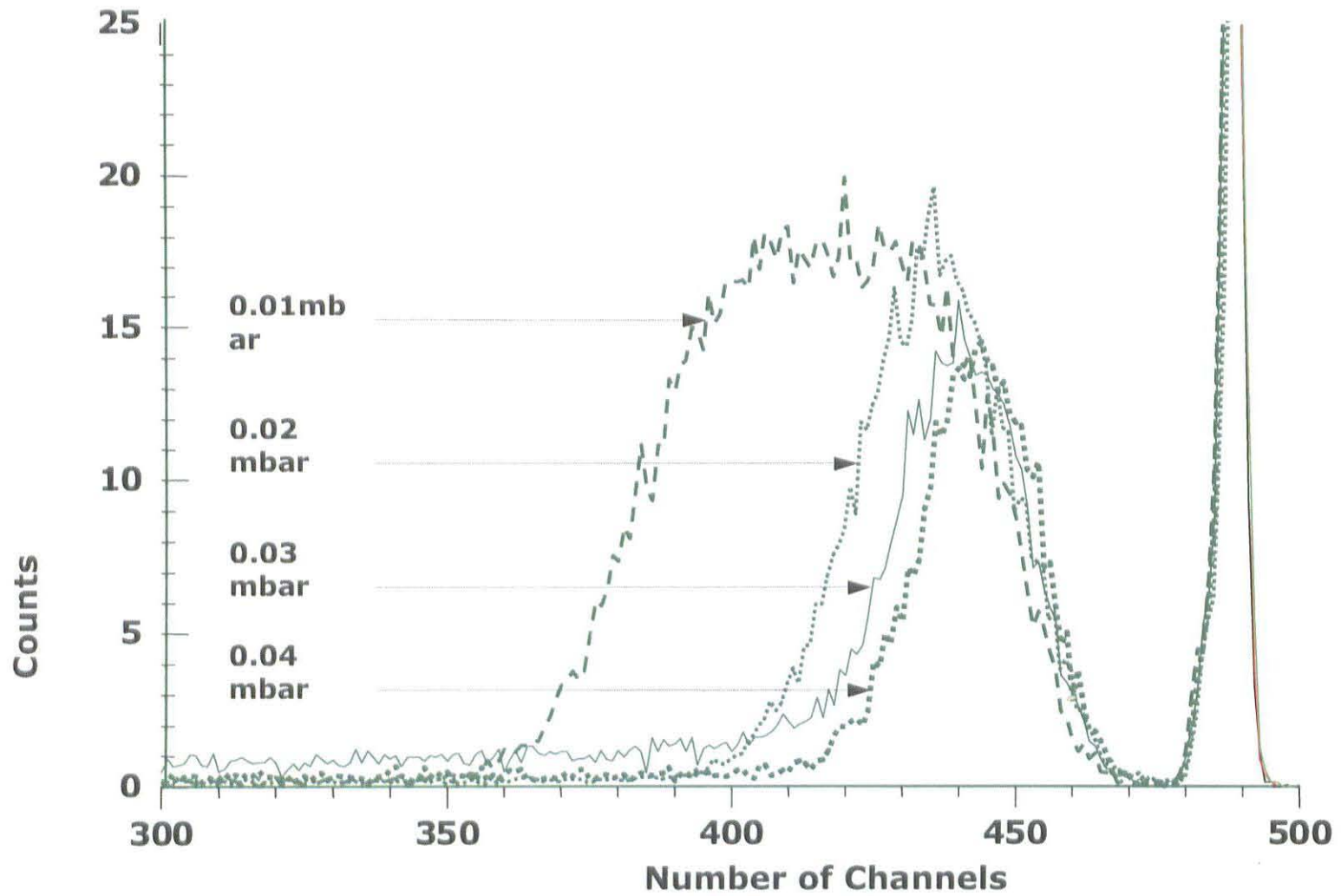


Figure 32: ERDA profiles of DLC films deposited onto Si(100) at different pressures during a fixed time of 25min (Table 1).

Decoupling to segregate the carbons bonded to carbons and to hydrogen which introduce an additional complexity in treating the data. Table 10 reports some typical value of hydrogen concentration in DLC coatings by ERDA and other techniques.

Code	H (at. %)	Type of Carbon	Method	Reported by
1	60	Amorphous C films made by R.F. sputtering	ERDA with 12MeV C	[Fuj-1988]
2	25	DLC film by ion beam deposition	ERDA with 2MeV He ions	[Lon-1992]
3	20	DLC film made by PECVD, 75% CH ₄ and 25 H ₂	NRA with N ions	[Bru-1990]
4	16	DLC film made by PECVD, 25% CH ₄ 75% H ₂	NRA with N ions	[Bru-1990]
5	47	DLC film by R.F. plasma deposition	ERDA with 3MeV He ions	[Ing-1986]
6	35	Carbon foils by DC glow discharge	ERDA with 25MeV He ions	[Tai-1980]
7	21	Carbon foils by carbon arc method	ERDA with 25MeV He ions	[Tai-1980]
8	48	DLC films by microwave plasma deposition	ERDA with 85MeV Ni ions	[Ava-1994]
E1	23	DLC films by PLD	ERDA with 3MeV He ⁺ ions	Current measurements
E4	15	DLC films by PLD	ERDA with 3MeV He ⁺ ions	Current measurements

Table 10: Summary of the study of H concentration in carbon and DLC films obtained from different methods

Figure 32 illustrates a typical ERDA profile of a DLC film deposited onto Si (100) with its simulation using RUMP program. Typically, the ERDA spectra exhibit two peaks. The first one is centered at the

vicinity of channel 490 which corresponds to a hydrogen contamination localized on the surface of the DLC films. This hydrogen rich area consists certainly of H₂O vapor components from the atmosphere. The second peak rising from channel 470 which characteristics (integrated intensity as well as its width) exhibit a net evolution with the deposition time as well as the deposition pressure as reported in figure 35. In this later, one can distinguish the presence of hydrogen in all DLC samples. While hydrogen is distributed in a Gaussian type form for higher deposition partial pressure, it exhibits a bell shape type for the lower values. This concurs with the RBS results of Figure 29 and indicates that hydrogen and carbon seem to be distributed homogeneously within the DLC films. Consequently, one could conclude that the profile of both hydrogen and carbon in the deposited DLC films are concomitant and that the interaction at the substrate between the carbon species and hydrogen originating from the plume and the gas flow source respectively seems to take place as early as the growth stage. The quantification of hydrogen within the current DLC films was determined using the standard ERDA equation:

$$Y = N_p \cdot N_H \left(\frac{d\sigma}{d\Omega} \right)_R \cdot \Omega / \sin \alpha \dots\dots\dots \text{Equation 17}$$

where N_p is the number of incident ions, Ω is the solid angle subtended by the detector, α is the tilt angle of the sample with respect to the ion beam direction and $\left(\frac{d\sigma}{d\Omega} \right)_R$ is the Rutherford recoil cross section. Table 9 reports the range of hydrogen content in the films. It varies from 15.0% to about 23.0% atomic. If these values are within the range of those found in the literature, its variation with the film thickness seems puzzling. The concentrations of 23.0% and 15.0 at% correspond to sample E1 (thin film) and E4

(thick film) respectively. In fact such an abnormal behavior was observed by few authors [Fiy-1988, Ing-1980]. They concluded that hydrogen loss is due to the ion irradiation reported by Avasthi et al [Ava-1994]. The 3 MeV H^+ in this case, is energetic enough to penetrate the film and to knock out hydrogen so depleting the DLC film. The behavior of the decrease of hydrogen content was suggested to involve different mechanisms such as particle bombardment enhanced by the self-bias increases [Dam-2000]. Another studies also reported the same trend of H depletion, the effect of negative substrate bias voltage on H content [Kon-2000, Cap-2006].

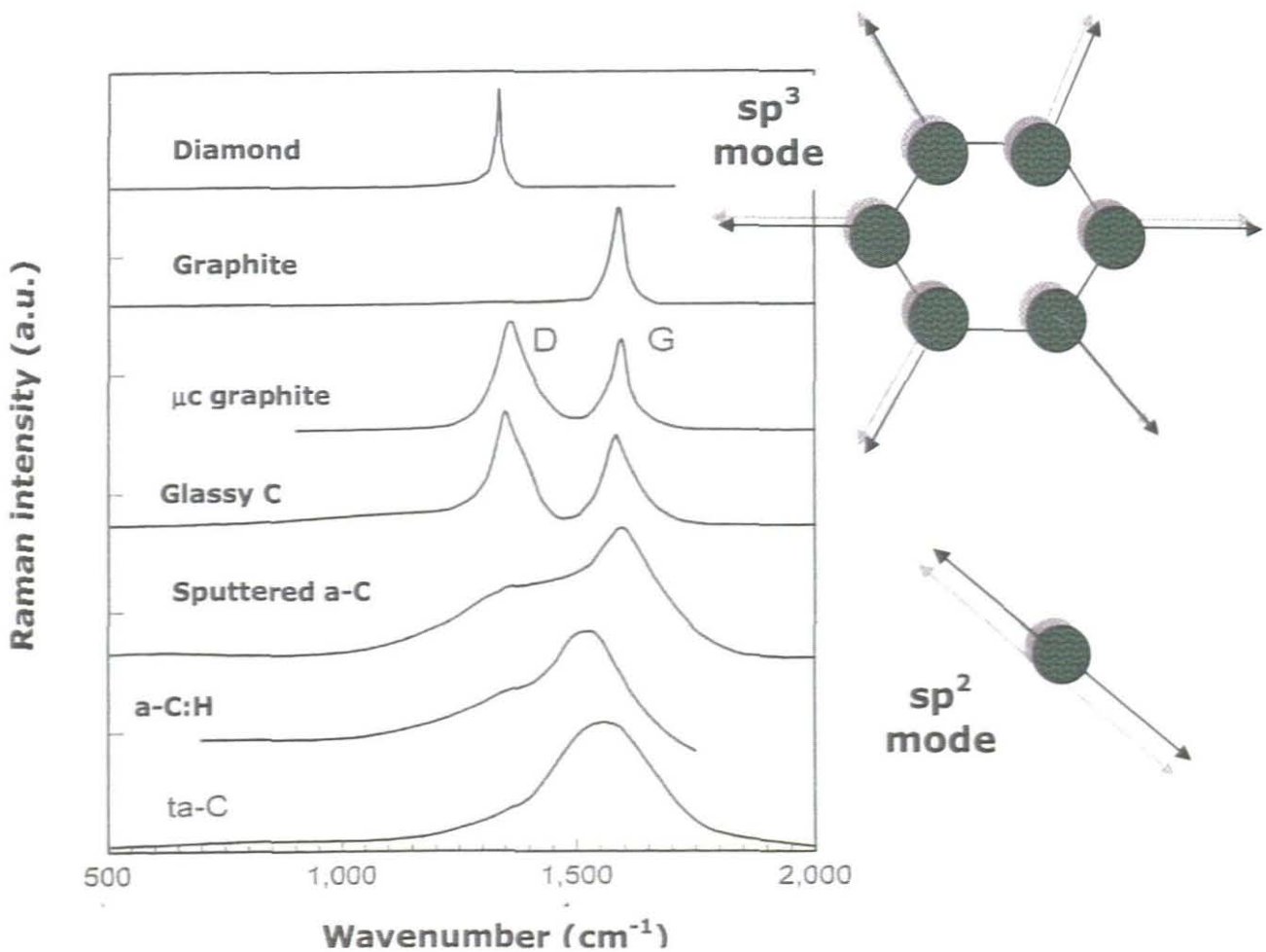


Figure 33: Comparison of typical Raman spectra of carbons [J. Robertson-2002].

5.2. Vibrational and electronic properties

5.2.1. Raman spectroscopy investigations

While ERDA and RBS investigations shed light on the carbon and hydrogen evolution as well as their quantification versus both the deposition pressure and deposition time, they do not allow the identification of the C-C and C-H type of bonding. Room temperature Raman spectroscopy as well as infrared spectroscopy was used for such a purpose with a focus on the Raman results specifically. Indeed Raman spectroscopy is the adequate non destructive tool to investigate the detailed bonding structure of DLC films. The Raman signature of diamond, graphites, fullerenes, nanotubes and DLCs are distinctive as shown in figure 36. Diamond has a single Raman active mode at 1332 cm^{-1} while single crystalline graphite exhibit two modes localized at 1580 and 42 cm^{-1} . While the first one is an E_{2g} symmetry mode, the second E_{2g} mode is due to interplane vibrations. The 1580 cm^{-1} graphite is known as "G" mode disordered graphite under a form of micro amorphous or glassy state exhibits an additional Raman active mode at 1350 cm^{-1} of A_{1g} symmetry and labeled "D". "G" and "D" are labeled for Graphite and Disorder respectively. Diamond like carbon coatings such as a-C:H and ta-C exhibit rather broad peaks around 1500 cm^{-1} . As can be noticed in both DLC cases, the peak is a convolution of 2 different contributions which are due to sp^2 and sp^3 components. In fact, excluding diamond and single crystalline graphite, all graphitic compounds exhibit the G and D modes of graphite with different relative intensities with the G mode always more intense than the D mode. This is due to the sp^2 and sp^3 bondings. One rationale in the existing of both modes with the G mode always more intense than the D mode is the Raman scattering

is dominated by sp^2 sites' scattering. The p states are lower in energy than the s states and therefore the p states are more polarizable. This gives the sp^2 sites a larger Raman cross section's value than sp^3 sites: 50 to 230 larger. Hence the sp^2 dominate the spectra of even the ta-C which has only 10-15% sp^2 sites. The G mode is the stretching vibration of any sp^2 pair both in C=C chains or in aromatic rings as indicated in Figure 33. The G mode does not reflect only graphitic state. The D mode is the breathing mode of sp^2 sites only in rings and not in chains. It is well established that the ratio on the D and G modes intensities i.e. $I(D)/I(G)$ is proportional to the number of rings at the edge of the carbon grains. The G peak is due to all sp^2 sites but the D peak is caused only by the six fold rings. Hence $I(D)/I(G)$ decreases with the rings' population and the increase of the chains population. In addition to the possibility to use $I(D)/I(G)$ as a guide in estimating the sp^2/sp^3 populations' ratio, there is an established guide illustrated in Figure 34 which also could be used. This later figure indicates the various factors which affect both the intensity and the position of the D and G Raman peaks.

While samples from the A, B, C, and D (Table 6-a) series exhibited Raman signals with more graphitic signature, those of series E display a convoluted peak similar to the a-C:H and ta-C Raman signatures as those of figure 36 [Che-2001]. Figure 34 reports the Raman spectra of samples E1, E2 and E3 deposited on Si (100) in the spectral range of 500-2400 cm^{-1} . While E1 is below, E4 and E5 are above the percolation threshold (Table 7, Figure 24).

Code	Raman peak position (cm ⁻¹)		FWHM(cm ⁻¹)		I _D /I _G	sp ² %	sp ³ %
	G-Band	D-band	G-band	D-band			
E1	1501	1350	273	412	17.6	79	21
E4	1507	1463	366	167	38.6	84	15.9
E5	1504	1479	308	406	45	2.9	97.1

Table 11: Raman results of the G and D peaks of samples E1, E4 and E5 (Table 7).

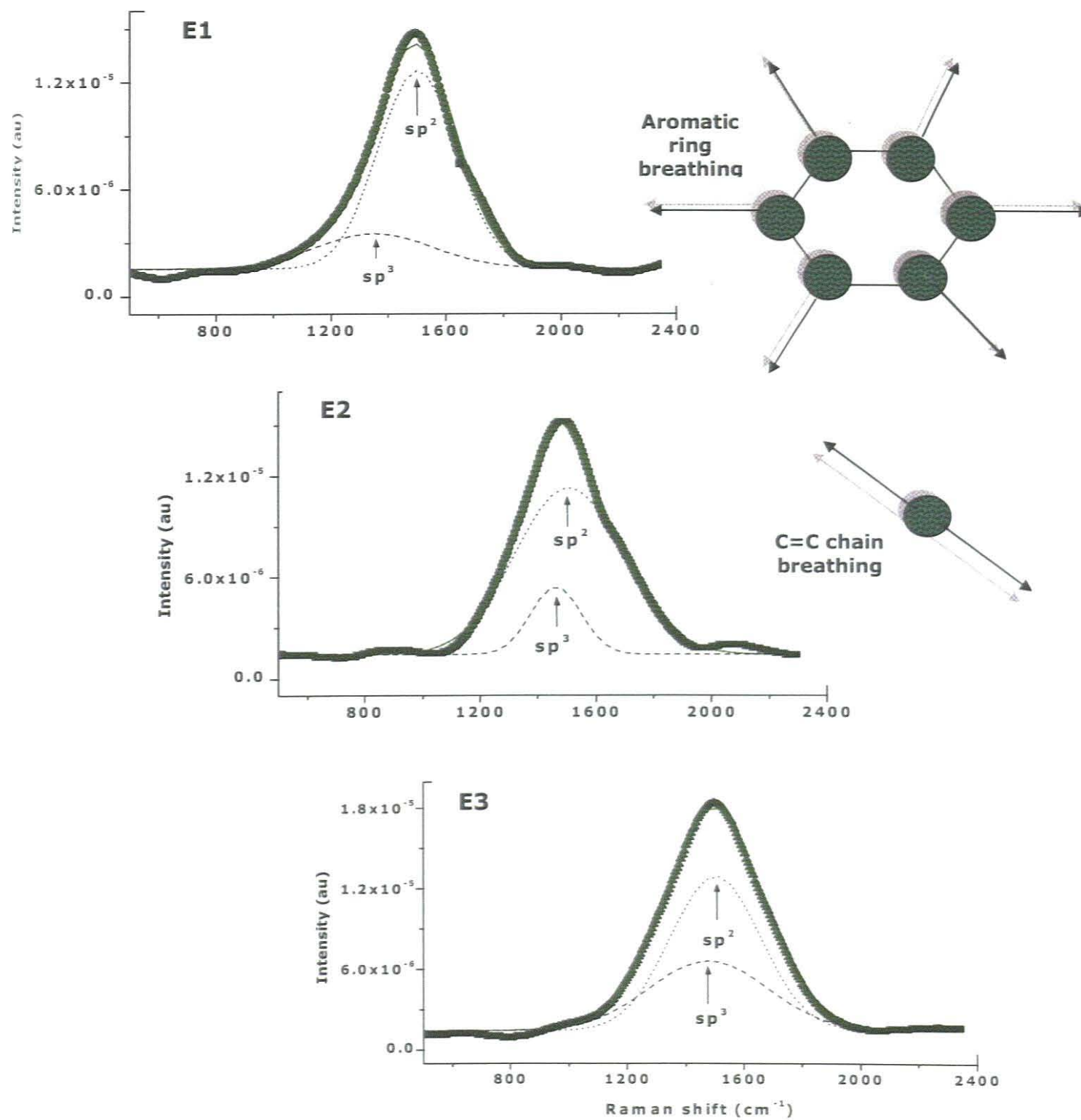


Figure 34: Room temperature Raman spectra of samples E1, E4 and E5 (Table 7).

The asymmetric Raman peaks are centered approximately at the vicinity of 1550 cm^{-1} . Their simulation, using Gaussian distributions allows their deconvolution via the sp^2 and sp^3 contributions with the sp^3 shifted to lower wavenumbers. Naturally, the sp^2 peak is constantly more intense than the sp^3 component. As per discussed previously, this is due to the fact that the Raman cross section of the sp^2 sites is stronger than the sp^3 one. More accurately, the broad full peaks are found within the spectral range of $1000\text{--}2000\text{ cm}^{-1}$ except for sample E5 at $800\text{--}2000\text{ cm}^{-1}$. The major peaks of sample E1, E4, and E5 are centered at $\approx 1488, 1489,$ and 1499 cm^{-1} . Table 11 reports the position, intensity and width at half maximum of both D and G modes. These G and D peaks are used to monitor the structural modification of the DLC films because they represent the structural information of the films and hence the estimation of the sp^2 and sp^3 average populations [Che-2001]. One should mention that visible Raman spectroscopy shows only the excited of sp^2 sites whereas the UV Raman spectroscopy excites both π and σ therefore it is possible to investigate the sp^2 and sp^3 bonding [Fer-2000].

The deconvolution of the Raman peaks indicates that while the spectral position of the G peak changes slightly from 1501 to 1507 cm^{-1} , the D peak has a tendency to shift significantly to higher wavenumbers, from 1350 to 1479 cm^{-1} . Hence, if one considers the well established order-disorder diagram in non-crystalline carbon system of Figure 35, one could conclude that higher is the DLC film thickness, larger is the trend to C based chains formation and clustering. According to Table 11, the $I(D)/I(G)$ ratio increases prominently from 17.6 to 45 with the DLC film thickness (i.e. deposition time), indicating the increase of the sp^3 sites population. Whereas the sp^2 sites population decreases from about $\sim 80\%$ to

~3%, the sp^3 sites population increases extensively from 21% to 97% when the DLC film thickness increases. Based on established DLC literature, such a significant variation of sp^3 sites out of the range of 10-15% indicate that the deposited DLC thin films are of a-C:H type and not ta-C type.

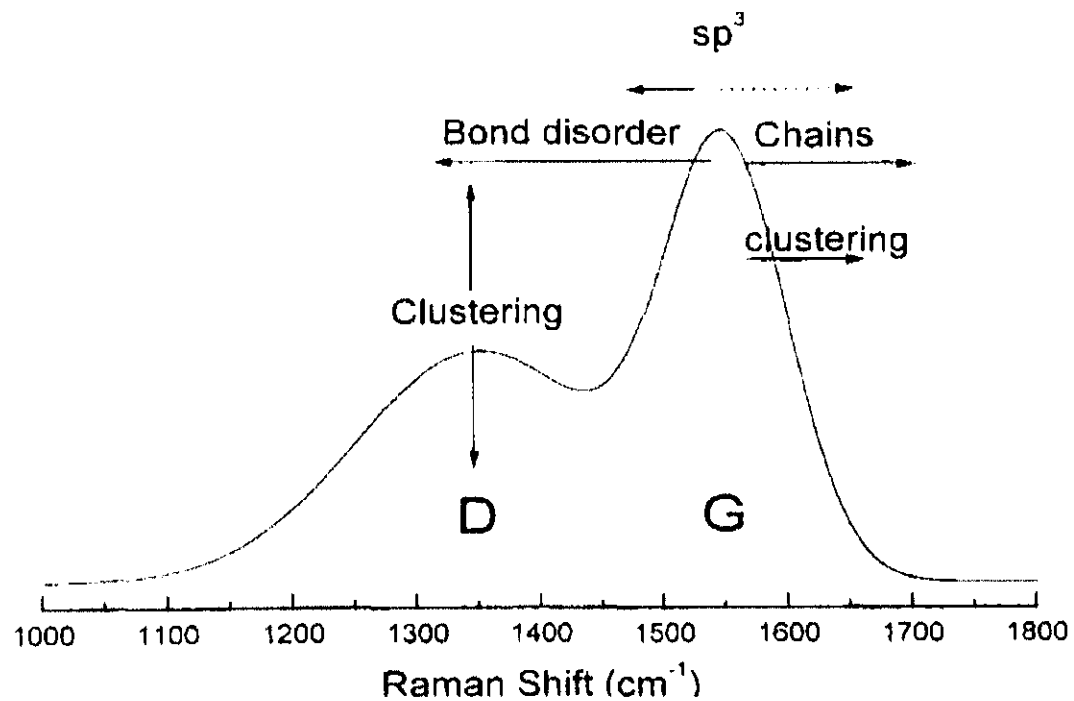


Figure 35: Schematic illustration of the factors affecting the positions and heights of the Raman G and D peaks of non-crystalline carbons [J. Robertson-2002].

5.2.2. Infrared spectroscopy investigations

The preceding visible Raman spectroscopy investigations are not sensitive to C-H bondings whilst the far Infrared spectroscopy «FTIR» is especially responsive to such radicals. Table 11 reports the major C-H vibrational modes in a-C:H (Rob-2002). Hence room temperature IR studies were conducted on the different samples. In this section, the focus would be more towards the evolution versus the DLC films' thickness (Series E, Table 6.a) as the corresponding deposition parameters fit with the optimized conditions. The identification of the C-H bonds is based on the usage of the IR vibrational frequency database obtained on a-C:H samples [Rob-2002] which is summarized in Table 12:

Wavenumbers (cm ⁻¹)	Type (sp ¹ /sp ² /sp ³)		Olefinic or aromatic	symmetric or antisymmetric
3300	sp ¹			
3085	sp ²	CH ₂	Olefinic	A
3035	sp ²	CH ₂	Aromatic	
2990-3000	sp ²	CH ₂	Olefinic	S
2975	sp ²	CH ₂	Olefinic	S
2955	sp ³	CH ₃		A
2920	sp ³	CH ₂		A
2920	sp ³	CH		
2885	sp ³	CH ₃		S
2855	sp ³	CH ₂		S
1480	sp ³	CH ₃		A
1450	sp ³	CH ₂		A
1430	sp ³	CH	Aromatic	
1415	sp ²	CH ₂	Olefinic	
1398	sp ³	(CH ₃) ₃		S
1375	sp ³	CH ₃		S
C-C				
2180	sp ¹			
1640	sp ²		Olefinic	
1580	sp ²		Aromatic	
1515	sp ² /sp ³			
1300-1270	sp ² /sp ³			
1245	sp ² /sp ³			

Table 12: IR vibrational frequencies in hydrogenated amorphous carbon (a-C:H) [J. Robertson-2002].

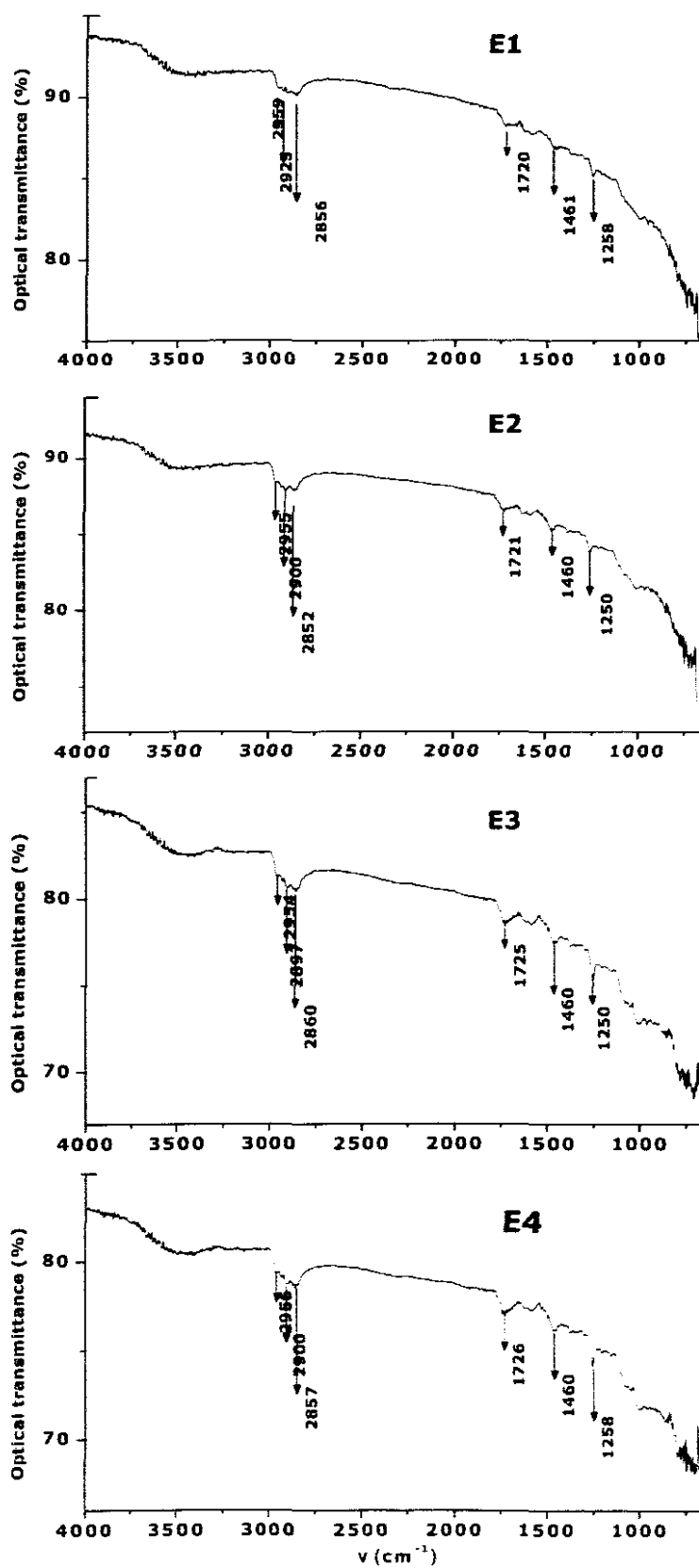


Figure 36: Room temperature Infrared spectroscopy spectra of samples E1, E2, E3 and E4 (7).

Figure 36 reports the IR spectra of the samples deposited onto Si(100) with different thicknesses in the spectral range of 640-4000 cm^{-1} . They exhibit two major band series within the range of 2800-3000 cm^{-1} and 1200-1800 cm^{-1} respectively. All of them exhibit similar trend with C-H stretching modes in the range of 2800 to 3000 cm^{-1} . As per summarized within Table 13, all DLC films present the following symmetric/asymmetric C-H modes: CH_3 , CH_2/CH , CH_2 , CH_3 , CH_2 , and CH_2 located at about 2995, 2900-2920, 2860, 2855 and 1450 respectively. The overall bondings of these vibrational modes are of sp^3 type. In addition to these sp^3 modes, all samples exhibit the sp^2/sp^3 mode assigned to 1245 cm^{-1} absorption. The current results confirms again that the synthesized DLC films are hydrogenated as confirmed by ERDA investigations and that the hydrogen is bonded with the sp^3 and carbon as observed generally in the literature [Rob-2002, Yan-2004].

Wavenumber (cm^{-1})	Configuration	Symmetry/ Antisymmetric	Sample E1	Sample E2	Sample E3	Sample E4
2955 ^a	Sp^3	CH_3	2959	2955	2954	2956
2900-2920 ^b	Sp^3	CH_2, CH	2925	2900	2897	2900
2860 ^b	Sp^3	CH_2, CH_3			2860	
2855 ^a	Sp^3	CH_2	2856	2852		2857
			1720	1721	1725	1726
1450 ^a	Sp^3	CH_2	1461	1460	1460	1460
1245 ^a	Sp^2/sp^3		1258	1250	1250	1258

Table 13: IR vibrational mode assignments in the C-H stretch region for the DLC films with different thicknesses deposited onto Si(100) [Rob-2002, Pan-2003].

5.2.3. X-rays photo-emission electron spectroscopy investigations

As mentioned previously, Raman scattering is dominated by the contribution of the sp^2 sites relatively to sp^3 ones due to the very large sp^2 Raman cross section (50 to 230 times larger). Consequently, the Raman spectra become controlled by the order of the sp^2 sites and not by the sp^2 fraction. Hence, a technique sensitive to the fraction sp^2/sp^3 is necessary. X-rays photo-emission electron spectroscopy is an adequate technique for such a purpose [Asa-1987]. Table 14 reports recent XPS studies on a-C:H. These results will be used as a guide within this section for the estimation of the sp^2/sp^3 ratio and its evolution versus the deposition time in particular.

Code	C1s, BE (eV)	Sp ³ , BE (eV)	Type of Carbon	Method	Authors
1	284.2	285-285.2	a-C:H films by PIII-D, C ₂ H ₂ & Ar	XPS	[Yang-2003]
2	-	286.1	DLC by Pulsed Vacuum arc plasma dep., Ar gas, RT	XPS	[Len-2003]
3	285	287	a-C films, Capacitively-coupled RF II plate plasma reactor, CH ₄	XPS, Mg K- α -line	[Fil-2003]
4	-	285.2	DLC films, by magnetron sputter neg. ion source, Ar plasma	XPS, Al K α monochromatic excitation source	[Nam-2005]
5	285	-	doped DLC films by hot wire plasma sputtering of graphite	XPS, Al k α source	[Vas-2004]
6	-	285.2	DLC films, by pulsed arc discharge method	XPS, Al k α	[Ala-2006]

Table 14: Summary of the study of C1s and sp³ content (%) of DLC films prepared by different methods in previous work.

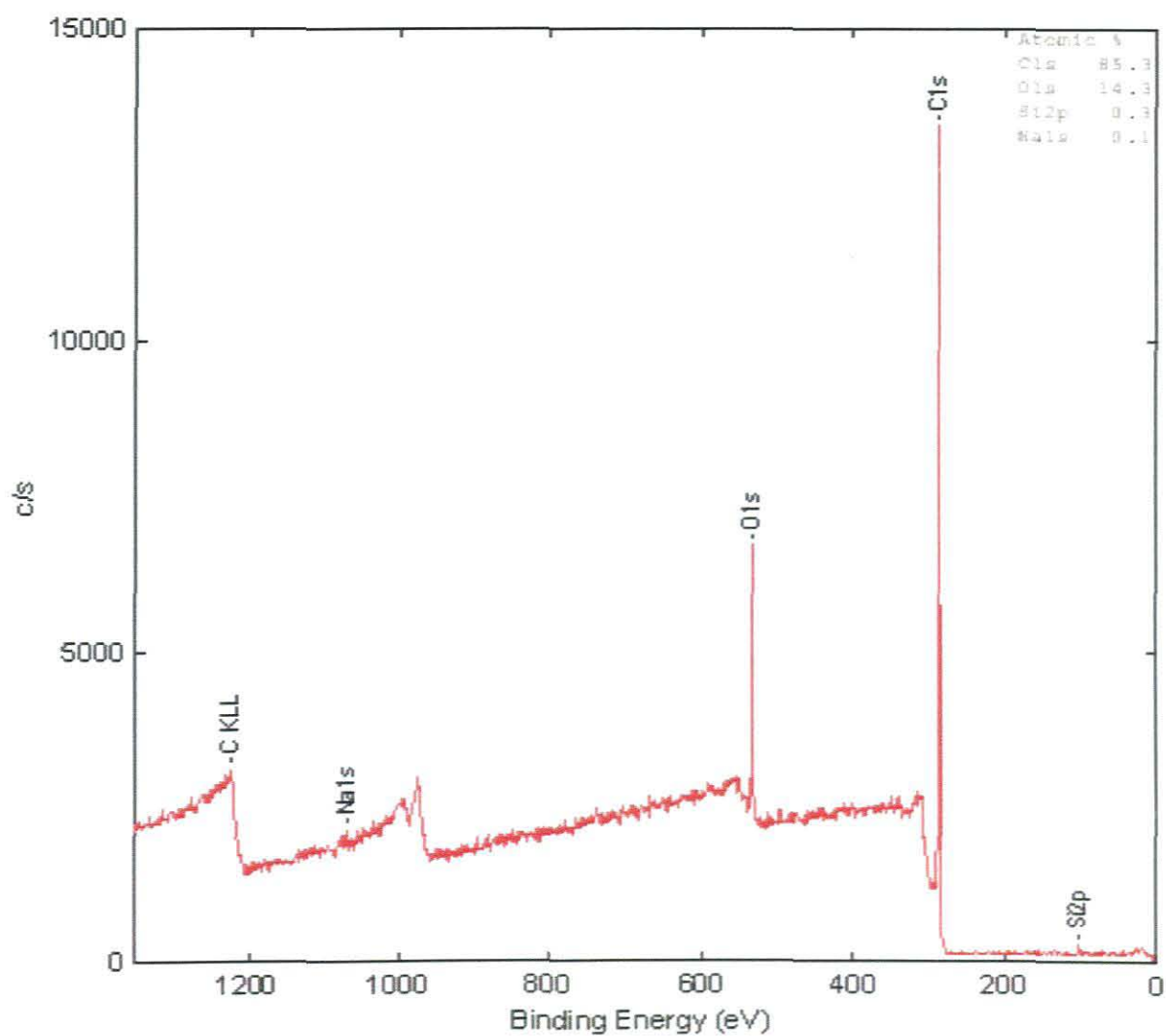


Figure 37: Typical core level XPS spectra of a DLC film: carbon (C) 1s, oxygen (O) 1s, and silicon (Si) 2p.

The XPS unit of the National Metrology Laboratory (Quantum 2000 scanning X-ray Photoelectron Spectrometer) was used. Figure 40 shows a typical XPS spectrum of the synthesized DLC films on Si(100). As it can be clearly noticed, the synthesized DLC film

contain few impurities including O (O1s edge), Na (Na1s edge) and Si (Si2p) at the level of 1.31-1.79 at.%, 0.1 at.% and 0.3-1.3 at.% respectively. These impurities, which were not detected by RBS (limit of detection), could be due to a contamination within the PLD chamber during the post-deposition as the graphitic Carbon target is of a high purity (99.9%, Carbon Lorraine).

To obtain the sp^2/sp^3 ratio, the C1s peak is considered. This later is located at about ≈ 285 eV as indicated in Figure 37. The simulation of the C1s peak by Gaussian-Lorentzian contributions allows determining the population ratio between sp^2 and sp^3 hybridization. The first spectrum at low binding energy indicates the sp^2 hybridization whereas the second one represents the sp^3 hybridization [Rie-2000, Nam-2005]. The films with high contribution of sp^2 carbon indicate the formation of ta-C type films [Fil-2003]. Figure 37 reports the XPS intensity variation at the C1s edge for different samples of series E (Fixed deposition parameters, variable deposition time: variable DLC films' thickness) and In addition to the evolution of Lorentzian and the Gaussian contributions, the full width at half maximum of the convoluted peak changes with the deposition time i.e. the DLC films' thickness. More precisely, the full-width at half maximum (FWHM) is about 1.41eV, 1.34 eV, 1.42eV, 1.49eV, and 1.56eV for samples deposited during 20, 30, 40, 50 and 60 min respectively. This indicates that the sp^2/sp^3 ratio depends on the deposition time i.e. the sp^2/sp^3 type bondings are tightly related to the growth mechanism. In the previous work by Namwoong [Nam-2005], the content of C1s obtained by using magnetron and magnetron sputter-type negative ion source methods does exhibit such growth dependence.

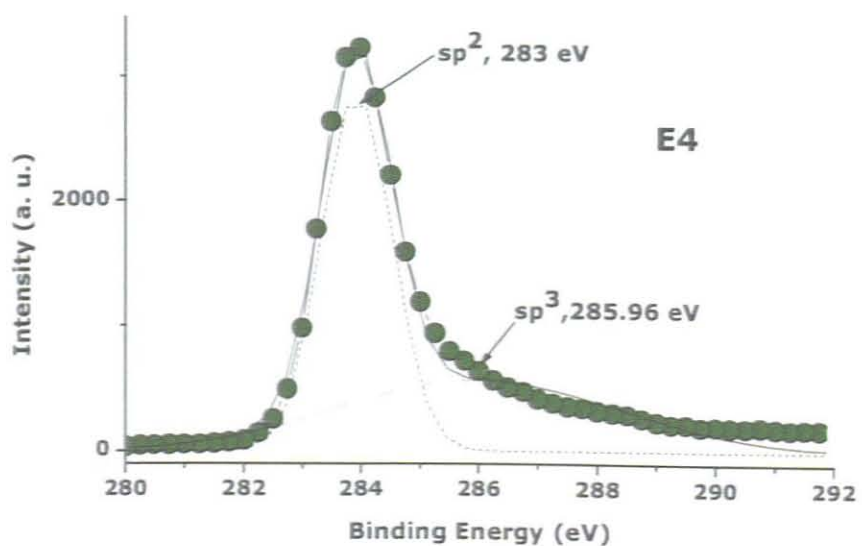
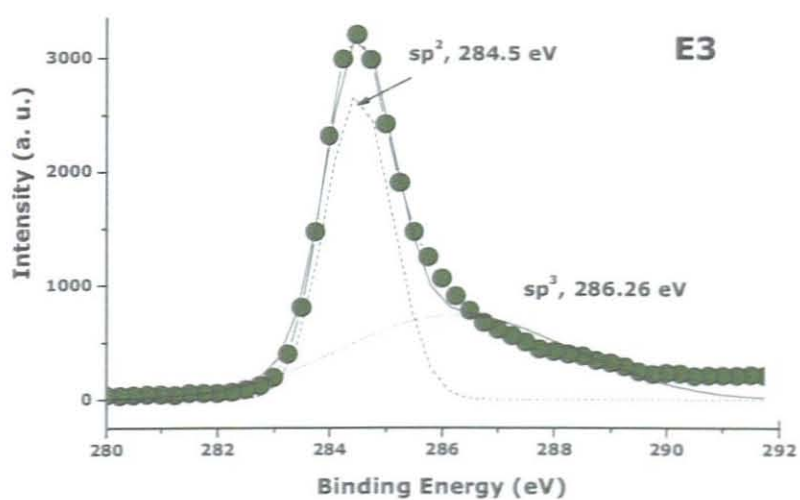
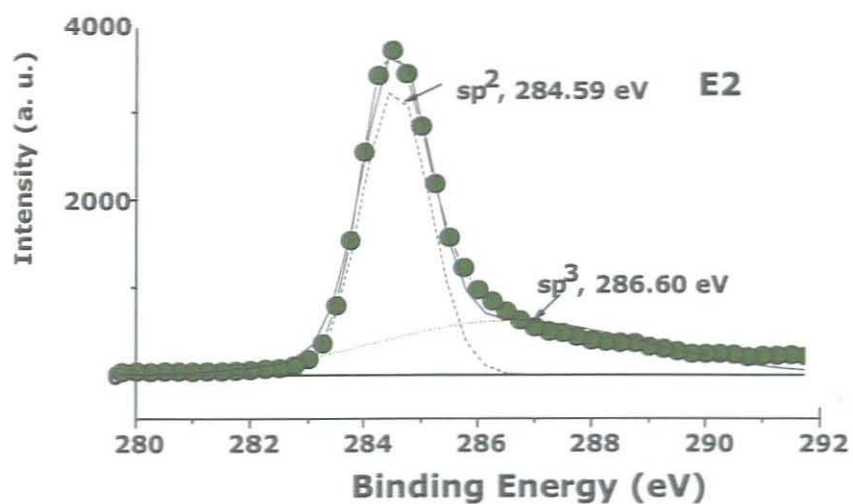


Figure 38: Typical core level XPS spectra of a DLC film at the Cs1 edge for samples of series E.

Table 15 reports the summary of the experimental XPS results as well as the simulation parameters of both the Lorentzian and Gaussian contributions. The sp^2 and sp^3 populations are derived accordingly.

Code	Voltage (kV)	Time (min.)	XPS, $sp^3\%$	sp^2 , BE(eV)	sp^3 , BE(eV)	Gaussian Shift sp^2 (eV)	sp^3 (eV)	C1s %
	18	25	34.4	283.91	285.4			85.1
D1								
	19	25	49.6	284.08	285.6			84.3
D2								
	20	25	39.6	284.03	285.5			82.4
D3								
	21	25	40.6	284.17	285.7			85.7
D4								
	22	25	51.3	283.98	285.5			88.8
D5								
	23	25	41.6	284.12	285.6			83
D6								
	24	20	13.9	284.42	285.5			85.9
E1								
	24	30	19.4	284.48	285.5	0.08	1.07	85.3
E2								
	24	40	21.1	284.46	285.5	0.04	0.75	81.9
E3								
	24	50	16.3	283.89	284.9	0.89	1.02	81.5
E4								
	24	60	88.5	283.59	284.6			84.3
E5								
G	24	120	86.91	283.53	284.4			85.4

Table 15: Summary of the XPS studies on samples of series E and D and their corresponding simulation parameters.

Based on Table 15, Figure 38 reports the evolution of the Gaussian and Lorentzian sp^3 and sp^2 contributions in terms of Carbon content as well as their respective peak positions for the samples series E. As for the width at half maximum which is varying with the deposition time, the binding energy peak position for both sp^2 and sp^3 varies in the same sense (Figure 39a); they are both constant below 40 min of deposition and decrease with approximately an alike slope with the film thickness above 40 min. Such a similar evolution indicates that the sp^2 and sp^3 populations are correlated. Indeed, as sustained by Figure 39, the sp^2 and sp^3 do exhibit well correlated evolutions with the DLC films' thickness. In general, while the sp^2 population decreases, the sp^3 component increases with a sharp variation above 50 min.

Concerning the effect of the laser voltage i.e. laser input fluence, the corresponding samples (Series D), the percentage of sp^3 were found ranging from 34.36 % to 51.26%. According to the literature review literature by Roberson [Rob-2002] and Pearce [Sea-2003], samples D2, D4, D6 correspond to hard a-C:H, whereas D5 represent soft a-C:H.

Concerning the samples deposited within the optimal conditions i.e. samples of series E, and considering the literature results, one could summarize the XPS results (taking into account the previous RBS, ERDA, Raman, Infrared results) as (Table 16):

- (i) films are of a graphitic nature for small thicknesses (≤ 20 min),
- (ii) a-C:H films of GLCH (Graphite like a-C:H) type mainly for intermediate thicknesses (20-50 min) with a high sp^2 population,
- (iii) ta-C:H films for thicker films (≥ 50 min) with a very large sp^3 sites.

The a-C:H and the a-C:H DLC films rich in CH₂ and CH₃ termination sites. Likewise these results show that DLC films richer in sp³ bonding can be obtained at high deposition time even with a low hydrogen content which is within the range of 15-23 at.%. In the previous studies it was found that a-C films produced by standard pulsed laser ablation evaporating graphite target, high quality of DLC films with >90% of sp³ bonds of carbon can be obtain at the impact energy $\approx 100\text{eV}$ ($1.6 \cdot 10^{-16}\text{J}$). Theoretically, the ta-C films has surface layers with lower sp² carbon than bulk and this is also possible for a-C:H films [Fil-2003].

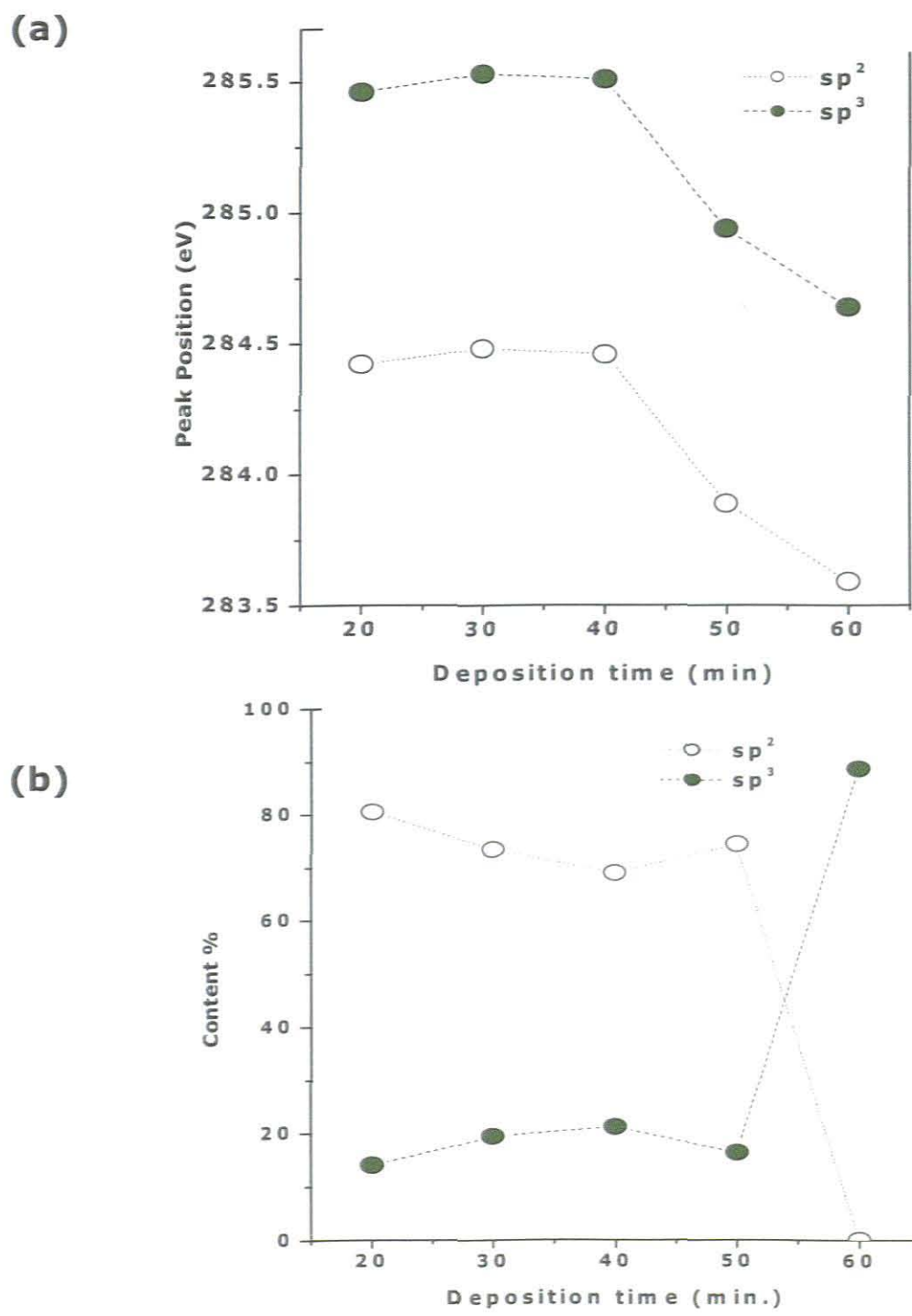


Figure 39: Thickness evolution of sp² and sp³ populations for samples of series E.

Type of DLC	H content % at	Sp ³ population	Sp ³ bonding	Nature
a-C:H	40-60	<70%	Sp ³ -H terminated sites	Soft polymer (PLC-H)
a-C:H	20-40	Lower sp ³	C-C sp ³	Hard DLC
ta-C:H	25-30	≈ 70%	-	-
a-C:H	<20	High sp ²	-	G-LCH

Table 16: Thickness evolution of sp² and sp³ populations for samples of series E.

5.2.4. Optical properties

The UV-VIS-NIR spectrophotometry was used to determine the optical properties of the DLC films with a focus on the determination of the refractive index dispersion. DLC films are often optically transparent in the NIR region above 900nm. Figure 40 reports the room temperature optical transmission of samples from D series in the spectral range of 400-900 nm. Parallel to the interference fringes due to the DLC film thickness, the average value of the optical transmission is about 65% above 700nm. Using the standard method described in chapter 4-section 3.3, the Sellmeir dispersion relation was deduced. The considered approximation for $n(\lambda)$ is [Mar-2003].

$$n(\lambda) = \left[A_1 + \frac{A_2 \lambda^2}{\lambda^2 - A_3} \right]^{1/2} \dots \dots \dots \text{Equation 18}$$

Based on the theory of Tauc-Lorentz model developed by Jellison and Modine [Fil-2003]. The refractive index n of the synthesized DLC films prepared at different voltage was found ranging from 1.7 to 2.2. The refractive index obtained in this work shows different behavior with the change in voltage and correlate with the thickness of DLC film. Gielen et al [Gie-1996] who used expanding thermal plasma to produce a-C:H in the atmosphere of acetylene gas (C_2H) obtained refractive index values of about 2.05 (visible range) and 1.95-2.09 (infrared range). According to their study the quality of the a-C:H with high hardness can be achieved by maximizing the refractive index [Ued-1999]. J. Filik et al [Fil-2003] reported refractive index n of a-C:H produced in the atmosphere of a mixture of CH_4 and H_2S of about 1.6 and 2.3. It was observed that DLC films with refractive index less than 1.6 exhibit a polymer-like

behavior rather than diamond-like. It was observed experimentally that if the value of n is larger than 1.8, the carbon films are of a diamond-like nature. The calculated results of the refractive index n and the thickness t of the synthesized nano-structured DLC film deposited at difference voltage are tabulated in Table17 obtained by means of MATLAB software. One should justify that the optical transmission were conducted only on the C series because due to their transparency in the UV-VIS spectral range.

Sample code	substrate	Voltage (kV)	Working Pressure(mbar)	Time (min)	Refractive index (n)	Thickness (nm)
C:3	Glass	20	0.01	25	2.2064	450
C:4	Glass	21	0.01	25	1.9916	420
C:6	Glass	23	0.01	25	1.7192	740
G	Si	24	0.02	120	-	353

Table 17: Summary of the optical properties of DLC films produced by PLD in an atmosphere of CH₄.

As summarized in Table 17 and reported in Figure 41, the obtained values of the refractive index within the VIS-NIR spectral region are very high relatively to reported values in the literature. The values are, 2.42 (Cubic i.e diamond, faceted crystal), 2.15 (Hexagonal i.e. graphite), 1.5-3.1 (large sp^2/sp^3 ratio DLC) and 1-6-3.1 (large sp^3/sp^2 ratio DLC). Even if the obtained value of the refractive index is large, it could reflect the density of the obtained DLC nano-structures caused by the current dual pulsed laser beam-pulsed gas flow feeding. These high values could be attractive if one considers the well established selective absorption

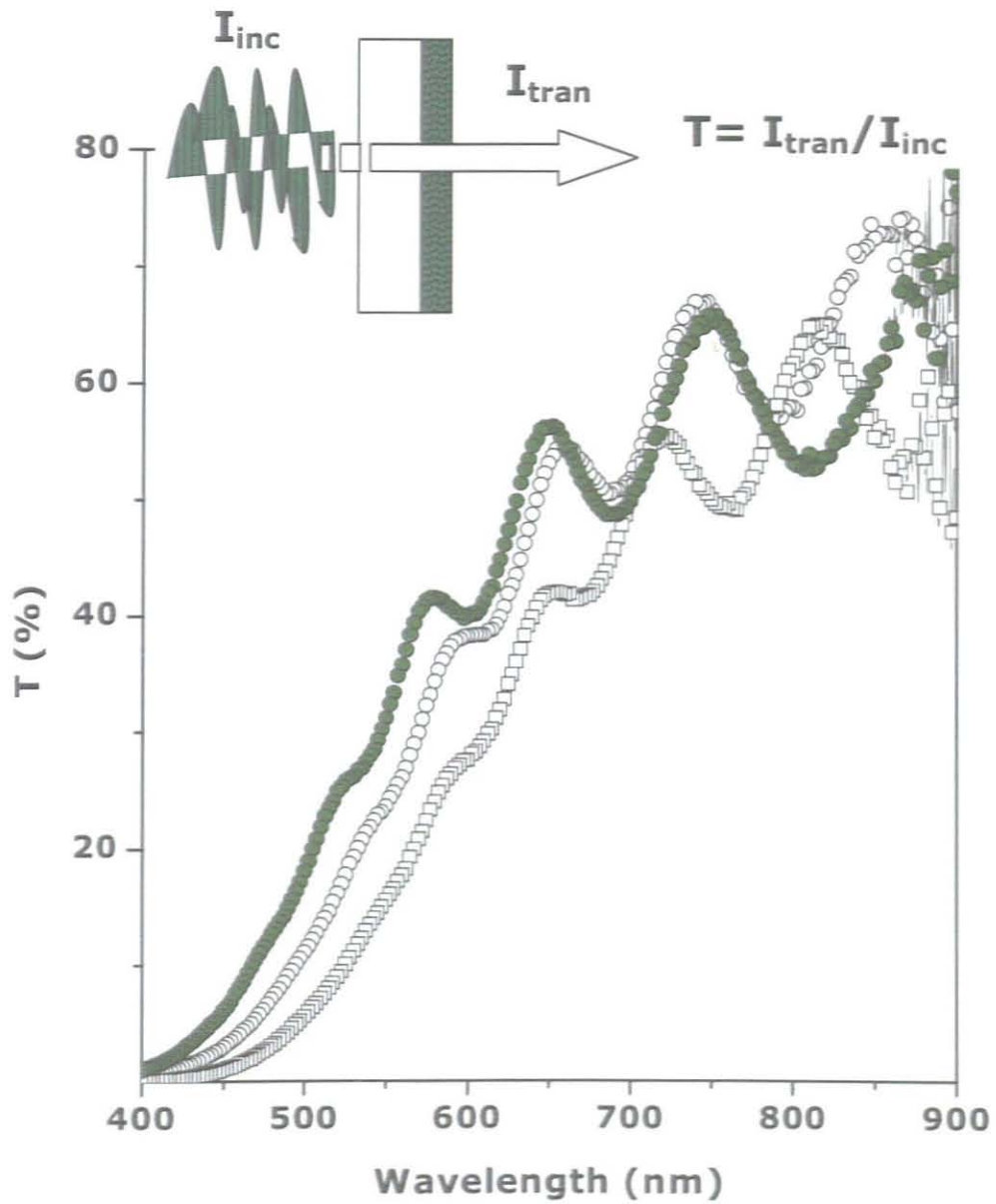


Figure 40: Experimental optical transmittance spectra of DLC films deposited at different voltages: D3 (O O O O), D4 () and D6 (●●●●).

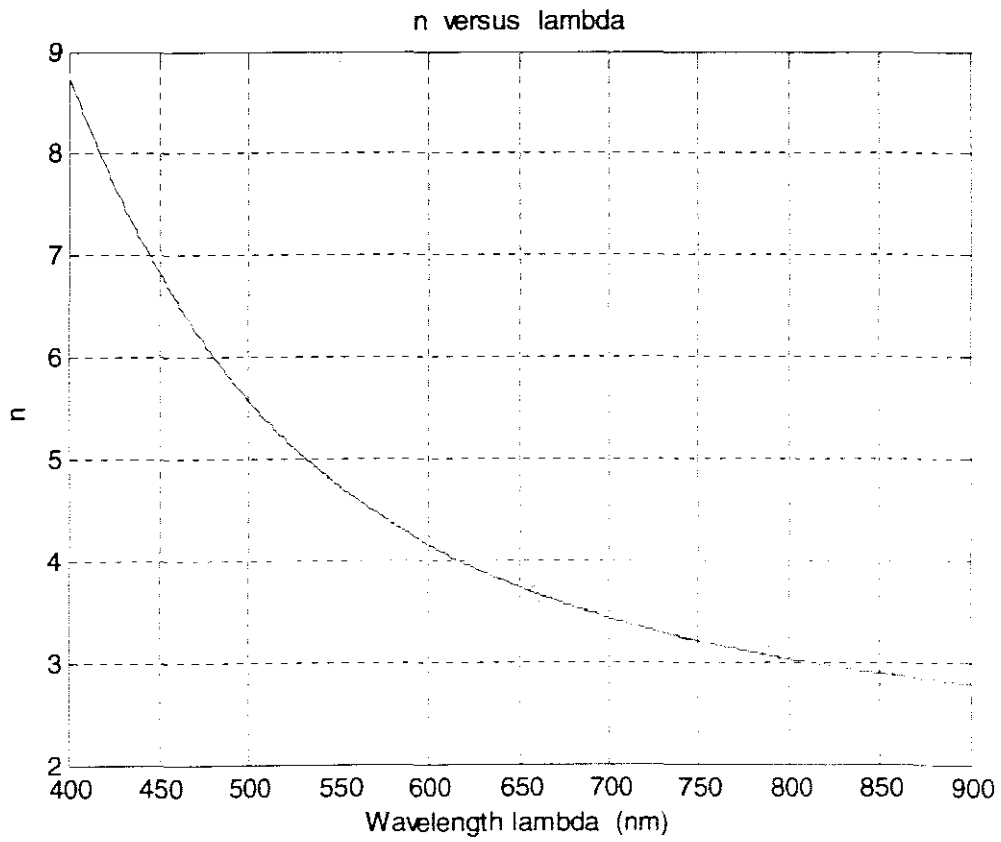


Figure 41: Dispersion relation of DLC films deposited onto glass substrates.

CHAPTER 6

CONCLUSION AND PERSPECTIVES

In summary, the present study demonstrates for the first time the ability of the current dual pulsed gas flow-pulsed laser deposition to synthesize Diamond like carbon nano-structures on unheated silicon /float glass substrates with a high sp^3/sp^2 ratio. This double pulsed approach used within the framework of this research project consists of ablating pure carbon target and injection of pulsed flow of methane or/and hydrogen onto the growth zone at the vicinity of the substrate's surface. This configuration was expected to thermalize less the ablated carbon species within the plume and permits an improved local interaction between the gas pulses and the carbon species. Relatively to the standard pulsed laser deposition, all synthesized DLC nano-structures by the double pulsed approach exhibited a significant mechanical adhesion on the used crystalline or amorphous substrates. All deposited DLC nano-structures were cracks free indicating that stress related effects are minimized.

The surface morphology investigations were performed by scanning electron microscopy, Zygo optical interferometry and mechanical surface mapping. The elemental-chemical analyses were carried out by Rutherford backscattering, Elastic recoil detection analysis as well as X-ray photoelectron spectroscopy. This later was, in addition used to investigate and quantify the C-C sp^2-sp^3 type bonds. The accurate sp^2/sp^3 and C-C as well as C-H bonding nature were studied by Raman and infrared

spectroscopies at room temperature in addition to the UV-VIS-NIR spectrophotometry.

The mechanical surface topography studies showed that the clusters of carbon and/or hydrogenated carbon seem to grow independently within the relatively cold surface of the substrate being it a silicon or glass substrate. Thereafter they start to coalesce following a threshold value of the DLC's thickness which seems to be located within the range of 20-30 minutes deposition time. From this coalescence value, the DLC nano-structures begin to smoothen forming a quasi-leveled smooth surface. Hence, the coalescence limit could be considered as located at the vicinity of 30 min in terms of deposition time/thickness correspondence.

The optical interferometry surface mapping indicated that the films have a tendency to smoothen following the coalescence stage. This could be considered as a sign of an amorphization phenomenon, an assumption sustained by both scanning electron microscopy and X-ray diffraction investigations carried out on all DLC samples deposited without heating. The samples do not exhibit Bragg peaks structure but rather a very large non intense peak centered around 25 deg; a signature of an amorphous state indeed.

The scanning electron microscopy showed that all films were continuous and cracks' free, implying that the stress and related effects if any are insignificant. Such stress free phenomenon in the DLC nano-structures seems to be favored by the local interaction occurring between the ablated carbon species and the pulsed methane/hydrogen molecules originating from the pulsed gas source.

The elemental investigations pointed out that the carbon profile is not constant within the DLC films' thickness but rather varies through out the growth phase. Such an evolution was interpreted as an indication of a variation of the reactivity of carbon with hydrogen of the carbon clusters at the substrate with the films' thickness. It was concluded that this carbon variation might be an indication therefore of a variation of the sp^2/sp^3 ratio during the growth stage. It was noticed that the carbon concentration reduction is substantial after 20 min deposition time, a value which concurs with the percolation threshold.

The hydrogen profiling indicates that both hydrogen and carbon in the deposited DLC nano-structures are concomitant and that the interaction at the substrate between the carbon species and hydrogen originating from the plume and the gas flow source respectively seems to take place as early as the growth stage. The hydrogen content was estimated to be within the range of 15.0% - 23.0% atomic depending on the deposition conditions.

The Raman spectroscopy investigations revealed obvious DLC trends similar to the standard a-C:H and ta-C Raman signals. Based on the established order-disorder diagram in non-crystalline carbon system and the variation of the G and D Raman modes, it was concluded that higher is the DLC nano-structure's thickness, larger is the trend to C based chains formation and C clustering. The $I(D)/I(G)$ ratio was found to increase prominently with the DLC film thickness, indicating the rise of the sp^3 sites population. Whereas the sp^2 sites population decreases significantly; the sp^3 sites population increases extensively to reach values as large as 97% when the DLC film thickness increases. Such a significant variation of sp^3 sites out of the range of 10-15% specifies that the deposited DLC thin films are of a-C:H type and not ta-C type. This

Raman results were complemented by infrared and XPS studies. The infrared spectroscopy investigations showed that the hydrogen is bonded with carbon atoms in sp^3 bonding type as observed generally in the literature. Based on the XPS investigations, it was confirmed that while the sp^2 population decreases, the sp^3 component increases with a sharp variation above 50 min.

Taking into account the previous elemental and spectroscopy investigations, one could summarize the growth of the DLC nanostructures by the dual pulsed laser deposition/pulsed gas feeding as follows:

- (i) films are of a graphitic nature for small thicknesses (≤ 20 min),
- (ii) a-C:H films of GLCH (Graphite like a-C:H) type mainly for intermediate thicknesses (20-50 min) with a high sp^2 population,
- (iii) ta-C:H films for thicker films (≥ 50 min) with a very large sp^3 sites.

The a-C:H and the ta-C:H DLC films rich in CH_2 and CH_3 termination sites. Likewise these results show that DLC films richer in sp^3 bonding can be obtained at high deposition time even with a low hydrogen content which is within the range of 15-23 at.%.

BIBLIOGRAPHY

- [Aha-1999] Ahalapitiya Hewage Jayatissa, Funio Sato and Nobuo Saito, *J. Phys. D : Appl. Phys.* 32, 1443-1446, (1999).
- [Ala-2006] E. Alakoski, *Studies on diamond-like carbon and novel diamond-like carbon polymer hybrid coatings deposited with filtered Pulsed arc discharge method*, (2006).
- [All-2000] R. Allenspach, *Spin-polarized scanning electron microscopy*, Vol. 44No. VOL. 44 (2000).
- [Art-2001] Arto Nurmela, *Non-Rutherford Elastic Scattering Cross Sections for Materials Analysis*, University of Helsinki, (2001).
- [Asa-1987] K. Asami and K. Hashimoto, *X-ray photoelectron Spectroscopy for Corrosion Studies*, *Langmuir*, 3, 897-904, (1987).
- [Ava-1994] D K Avasthi, D Kabiraj, Jaipal and G K Mehta, H C Barshilia, Somna, Sah, B R Mehta and V D Vankar, *Study Hydrogen in DLC film by ERDA with ⁵⁸Ni ions*, (1994).
- [Bar-1997] N. P. Barradas, C. Jeynes, and R. P. Webb, *Simulated annealing analysis of Rutherford backscattering data*, (1997).
- [Bat-2002] Battelle, *X-ray photoelectron spectroscopy (XPS)*, EMSL, U.S. Department of Energy Pacific Northwest National Laboratory, (2002).

- [Bon-2002] M. Bonelli, A.C Ferrari, A. Fioravanti, A. Li Bassi, A. Miotello, and P.M. Ossi, *Eur. Phys. J. B* 25, 269-280, (2002).
- [Bon-2005] Bong Geum Choi, Jae Kwang Kim, Won Jae Yang and Kwang Bo Shim, *Journal of Ceramic Processing Research*, Vol. 6, No.2, pp. 101-105 (2005).
- [Bru-1990] J Bruley, P Madakson and J C liu, *Nucl Instr Meth*, B45, 618, (1990).
- [But-2002] A.L. Butterworth, R.J. Chater, and I.A. Franchi, *Lunar and Planetary Science*, XXXIII, (2002).
- [Cam-2003] Camps E., Escobar-Alarcón L., Espinoza M. E, Camacho-Lopez M. A., Rodil S. E. Muhl S. *Superficies y Vacío* 16(4), 37- 41, diciembre de (2003).
- [Cap-2006] Gil Capote, Luís F. Bonetti, Lúcia V. Santos, Vladimir J. Trava-Airoldi, Evaldo J. Corat, *Braz. J. Phys.* v.36 n.3b São Paulo set. (2006).
- [Che-2001] C.-L Cheng, C.-T Chia, C.-C Chiu, C.-C Wu, H.-F Cheng, I.-N Lin, *Applied Surface Science*, 174, 251-256, (2001).
- [Che-2001] C.-L Cheng, C.-T Chia, C.-C, Wu, I.-N Lin, *Diamond and Related Materials* 10, 970-975, (2001).
- [Che-2002] C.-L Cheng, C.-T Chia, C.-C Chiu, I.-N Lin, *Diamond and Related Materials* 11, 262-267, (2002).

- [Chu-2002] Churl Seung Lee, Kwang-Ryeol Lee, Kwang Yong Eun, Ki Hyun Yoon, Jun Hee Han, *Diamond and Related Materials*, 11, 198-203, (2002).
- [Cin-2007] Cinzia Casiraghi, John Robertson, and Andrea C. Ferrari, *Materials Today*, vol. 10, no.12, (2007).
- [Dam-2000] J. C. Damasceno, S. S. Camargo Jr, F. L. Freire Jr and R. Carius, *Surface and Coatings Technology*, Volume 133-134, pp. 247-252, (2000).
- [Dav-1998] David M. Teter, Chapter 1, *MRS Bulletin*, (1998).
- [Esa-2006] Esa Alakoski, *Studies on Diamond-like carbon and Novel diamond-like carbon polymer Hybrid coatings deposited with Filtered Pulsed Arc Discharge Method*, (2006).
- [Esc-2000] L. Escobar-Alarcon, E. Camps, B. Rebollo, E. Haro-Poniatowski, M.A. Camacho-Lopez, S. Muhl, *Surficies y Vacio* 11, 36-39, (2000).
- [Fer-2000] A.C. Ferrari and J. Robertson, *Physical Review B* Volume 61, Number 20, (2000).
- [Fie-2005] P. Fierlinger, S. Heule, A. Knecht, U. Straumann, *University de Fribourg*, pp 7, (2005/06).
- [Fil-2003] J. Filik, I.M. Lane, P.W. May, S.R.J. Pearce, K.R. Hallam, *Diamond and Related Materials* 13, 1377-1384, (2003).
- [Fil-2003] J. Filik, P. W. May, S.R.J. Pearce, R.K. Wild, K.R. Hallam, *Diamond and Related Materials*, 12, 974-978, (2003).

- [Fra-2002] D. Franta, L. Zajickova, I. Ohlida, J. Janca, K. Veltruska, *Diamond and Related Materials*, 11, 105-117, (2002).
- [Fuge-2004] G.M. Fuge, P.W. May, K.N. Rosser, S. R.J. Pearce, M.N.R. Ashfold, *Diamond and Related Materials*, 13, pp. 1442-1448, (2004).
- [Fuj-1988] F Fujimoto, M Tanaka, Y Iwata, A Ootuka, K Komaki, M Haba and K Kobayashi, *Nucl Instr and Meth*, B33, 792, (1988).
- [Gag-2005] R. Gago, M. Vinnichenko, H. U. Jager, A. Yu. Belov, I. Jimenez, N. Huang, H. Sun, and M.F. Maitz, *Physical Review B* 72, 014120, (2005).
- [Gie-1996] J.W.A.M. Gielen, M.C.M. van de Sanden, and D.C. Schram, *Appl. Phys. Lett.* 69, (2), (1996).
- [Gop-2002] B Gopalakrishnan and SV Subramanyam, *Many phases of Carbon*, (2002).
- [Han-2000] E B Hanlon, R Manoharan, T-W Koo Shafer, JT Motz, M Fitzmaurice, JR Kramer, I Itzkan, RR Dasari and MS Feld, *Phys. Med Biol.* 45, R1-R59, (2000).
- [Hav-2003] J. Haverkamp, R. M. Mayo, and M.A. Bourham, J. Narayan and C. Jin, G. Duscher, *Journal of Applied Physics*, Volume 93, Number 6, (2003).
- [Hel-2001] Helen Ronkainen, *Technical Research Centre of Finland*, (2001).

- [Heo-2004] Heon Woong Choi, Myoung-Woon Moon, Tae-Young Kim-Ryeol Lee, and K Yu Hwan Oh, *Mat. Res. Soc. Symp. Proc. Vol. 795*, (2004).
- [Heo-2006] Heon Woong Choi, Kwang-Ryeol Lee, Rizhi Wang, Kyu Hwan Oh, *Diamond & Related Material*, 15, pp. 38-43, (2006).
- [Hid-1999] Hideki Minami, *Characterization of Diamond-like Carbon Films Produced by Pulsed Laser Deposition*, University of Alberta, (1999).
- [Hua-2004] Huang Weidong, Ding Ding, Zhan Rujan, *Plasma Science & Technology*, Vol. 6, No. 2, (2004).
- [Hua-2007] Huayu ZHANG, Liangxue LIU, Yulei WANG, Hongtao MA and Fanxin LIU, *J. Mater. Sci. Technol.*, Vol.23 No.4, (2007).
- [Hue-TN-100] Hue Phan, *Fundamental Infrared Spectroscopy*, TN-100
- [Ing-1986] D C Ingram, J A Woolam and G Bu Abbud, *Thin Solid Films*, 137, 255, (1986).
- [Jac-2005] Raman spectroscopy: a simple, non-destructive way to characterize diamond and diamond-like materials, Vol. 17, No. 5, (2005).
- [Jar-2000] Jarmo Koivusaari, *Structural, Mechanical, and Electrical, and Electronic Properties of Pulsed Laser Deposited carbon thin films and C-Si- Heterojunctions*, Department of Electrical Engineering, University of Oulu, (2000).

- [Joh-2006] Johanna Ylanen, Petri Vuoristo, Institute of Materials Science, (2006).
- [Jos-2002] Joson Goldsmith, Eli Sutter, John Moore, Brajendra, Mark Growder, Surface Engineering: Science & Technology of Interface II, (2002).
- [Jud-1982] Judith A Smith, Phys, Educ, Vol. 17, (1982).
- [Kar-2002] H. Karl, I Grosshans, A Wenzel, B Stritzker, R Claessen, V N Strocov, G E Cirlin, V A Egorov, N K Polyakov, Yu B Samsonenko, D V Denisov, V M Ustinov and Zh I Alferov, Nanotechnology, 13, 631-634, (2002).
- [Kaz-1998] Kazuhisa Miyoshi, Structure and Mechanical Properties of Natural and Synthetic Diamonds, Lewis Research Center, Cleveland, Ohio, (1998).
- [Kon-2000*] Konstantin Iakoubovskii, Optical Study OF Defects In Diamond, PhD, Thesis, (2000).
- [Kon-2000] Y. Konishi, S. Ogura, N. Ikuchi, D. Imai, T. Nishihara, and M. Shinohara, Diamond and Related Materials, Volume 9, Issue 3-6, pp. 746-751, (2000).
- [Kri-2002] Krishna C. Kadiyala, Characterization and tribological behavior of diamond-like carbon and Nitrogen-doped Diamond-like carbon Thin films, MSc Thesis, The Department of mechanical Engineering, (2002).
- [Kul-2000] V Kullkovsky, F Franc, A. Delneka, V Vorlicek, and L Jastrabik, J Phys. D: Appl. 33, 2880-2883, (2000).

- [Lar-2003] Lars Landstrom, formation of Nanoparticles by Laser-Activated Processes, (2003).
- [Len-2003] Y.X. Leng, J.Y. Chen, P. Yang, H. Sun, G.J. Wan, N. Huang, Surface Science 531, pp. 177-184, (2003).
- [Lin-2002] Linjum Wang, Yiben Xia, Hujiang Shen, J. Phys. D: Appl. Phys., 36, 2548-2552, (2002).
- [Lon-1992] X Long, X Peng, F He, M Liu and X Lin, Nucl Instr Meth, B 68, 266, (1992).
- [Man-1999] R. D. Mansano, M. Massi, P. Verdonck, P. M. Nogueira, L. S. Zambom, H.S. Maciel, C. Otani, Superficies y Vacio 9, 111-114, (1999).
- [Mar-2003] M. Martino, A. P. Caricato, M. Fernandez, G. Leggieri, A. Jha, M. Ferari, M. Mattarelli, Thin Solid Films 433, 38-44, (2003).
- [Mic-2005] Michael Curry, Fourier Transform as used by Chemists, The University of Extra, (2005).
- [Mik-1999] Dr Mike, S. Lou, Dr. Joseph, C. Chen & Dr. Caleb, M. Li, Journal of Industrial Technology, Volume 15, Number 1, (1999).
- [Mor-1999] Moreton Moore, Mina Golshan, Grzegorz Kowalski, John Reid§, Steve Iollins, and Bridget Murphy, J. Phys. D: Appl. Phys. 32, A37-A41, (1999).
- [Mul-1999] S. Muhl, E. Camps, L. Escobar-Alarcon, O. Lea, Superficies y Vacio 9, 123-127, (1999).

- [Nam-2005] Namwoong Paik, *Surface & Coatings Technology*, 200, 2170-2174, (2005).
- [Nob-2001] Nobuyuki Matsuyama and Ken Yukimura, Toshiro Maruyama, *Journal of Applied Physics*, volume 89, number 3, (2001).
- [Pan-2003] Pankaj Gupta, *Synthesis Structured and Properties of Nanolayered DLC/DLC films*, MSc. Thesis, B.E., Panjab University, (2003).
- [Pau-1972] Paulus Gerardus Henricus Kusters, *FT-IR spectroscopy of thin Biological Layers*, (1972).
- [Pis-2005] S. Piscanec, F. Mauri, A. C. Ferrari, M. Lazzeri, J. Robertson, *Diamond & Related Materials*, 14, 1078-1083, (2005).
- [Rai-2001] Rainer Haerle, Elisa Riedo, Alfredo, Alfredo Pasquarello, and Alfonso Baldereschi, *Physical Review B*, Volume 65, (2001).
- [Rie-2000] E. Riedo, F. Comin, J. Chevrier, F. Schmithusen, S. Decossas, M. Sancrotti, *Surface and Coatings Technology*, 125, 124-128, (2000).
- [Rob-1994] J. Robertson, *Pure & Appl. Chem.*, Vol. 66, No. 9, pp. 1789-1796, (1994).
- [Rob-2001] J. Robertson, *phys. stat. sol. (a)* 186, No. 2, 177-185 (2001).

- [Rob-2002] J Robertson, Material Science & Engineering, Vol. R37, Nos. 4-6, (2002).
- [Rya-2004] R Ryan Vallance, Chris J Morgan, Shelby M Shreve and Eric R Marsh, J. Micromech. Microeng. 14 1234–1243, (2004).
- [Sam-1999] Sam Zhang, Hon Xie, Xianting Zeng, Peter Hing, Surface and Technology, 122, 219-224, (1999).
- [Sea-2003] Sean Pearce, The Synthesis and Characterisation of Carbon Phosphide, MSc. Thesis, pp. 1-19, Department of Chemistry, (2003).
- [Sem-2001] T.V. Semikina, A.N. Shmyryeva, Semiconductor Physics, Quantum Electronics & Optoelectronics, V. 4, N 4, P. 313-317, (2001).
- [She-2005] Shevon Johnson, Pulsed Laser Deposition of Hydroxyapatite Thin Films, Georgia Institute of Technology, (2005).
- [Sie-2000] M. P. Siegal, D. R. Tallant, L. J. Marktinez-Miranda, J. L. Barbour, R. L. Sumpson, D. L. Overmyer, Nanostructural Characterization of Amorphous Diamond-like carbon films, (2000).
- [Šil-2005] M. Šilinskas, A. Grigonis, Ž. Rutkūnienė J. Maniks, V. Kulikuaskas, Physics and Chemistry of Solid State, Vol. 6, No. 3, 394-397, (2005).

- [Sta-1998] A. Stavrides, J. Ren, M. Ho, J Cheon, J. Zink, H.P. Gillis, R.S. Williams, *Thin Solid Films* 335, 27-31, (1998).
- [Sum-1995] Suman B Iyera, K S Harshavardhanb, Vikram Kumar, *Thin Solid Films*, 256, 94-100, (1995).
- [Sun-2004] Sunil Kumar Pal, *Synthesis, Characterization and Tribological behavior of nitrogen-doped chromium-diamond-like carbon nanocomposite thin films*, MSc. Thesis, B. Tech, Institute of technology-Banaras Hindu University, (2004).
- [Sun-2005] Sung-Jin Cho, Jin-Won Chung, Kwang-Ryeol Lee, *Diamond & Related Materials* 14, 1270–1276, (2005).
- [Tai-1980] N R Tait, D W L Tolfree, P John, I M Odeh, M J K Thomas, M J Triker, J I B Wilson, J B A England, D Newton, *Nucl Instr and Meth*, 176, 433 (1980).
- [Tan-2006] W. C. Tan, K. Koughia, J. Singh, and S. O. Kasap, *Optical Properties of Condensed Matter and Applications*, (2006).
- [Tim-2002] Timo Sajavaara, *Heavy Ion Recoil Spectroscopy of Surface Layers*, University of Helsinki, (2002).
- [Ued-1999] A Uedono, S. Fujii, N. Morishita§, H. Itoh§, S Tanigawa, and S Shikata, *J. Phys.: Condens. Matter* 11, 4109-4122, (1999).

- [Vas-2004] V. N. Vasilets, A. Hirose, Q. Yang, A. Singh, R. Sammynaiken, M. Foursa, Y. M. Shulga, *Appl. Phys. A* 79, 2079-2084, (2004).
- [Waz-2005] Wazumi Kouichirou, Fuchigami Kenji, Uematsu Kazuo, Koga Yoshinori, and Tanaka Akihiro, *Tribological Properties of DLC films produced by Pulsed Biased Plasma CVD method*, Vol. 38, No. 1, (2005).
- [Web-1998] R.P. Webb, J.J. Jimenez-Rodriguez, M. Kerford, S.R.P Silva, *Diamond and Related Materials*, 7, pp 1163-1166, (1998).
- [Xia-2002] Xiao Liu, D.M. Photiadis, J.A. Bucaro, J.F. Vignola, B.H. Houston, *Material Science and Engineering A*, (2002).
- [Yan-2003] P. Yang, N. Huang, Y.X. Leng, J.Y. Chen, R. K.Y. Fu, S.C. H. Kwok, Y. Leng, P.K. Chu, *Biomaterials*, 24, 2821-2829, (2003).
- [Yan-2004] X B Yan, T Xu, S R Yang, H W Liu and Q J Xue ; *J. Phys. D: Appl. Phys.* 37, 2416-2424, (2004).
- [Yib-2003] Yibrán Argenis Perera Mercado, *Diamond-like carbon and ceramic materials as protective coatings grown by pulsed laser deposition*, (2003).
- [Zha-1999] Q. Zhang, S. F. Yoon, J. Ahn, Rusli, H. Yang, C. Yang, C. Yang, F. Watt, E. J. Teo, T. Osipowice, *Microelectronics Journal* 30, 801-805, (1999).